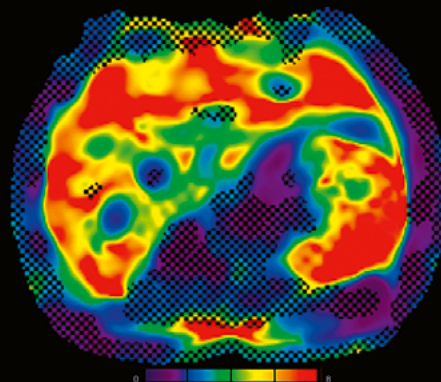
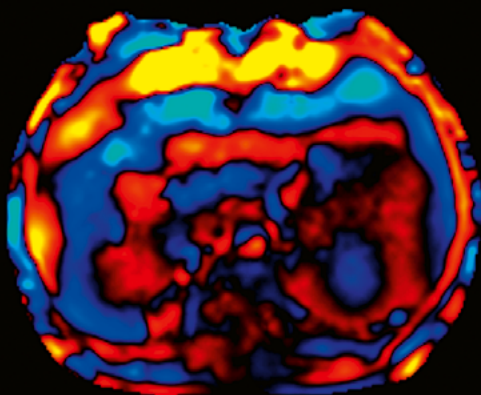
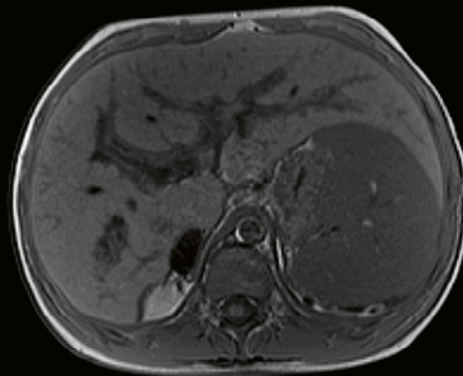
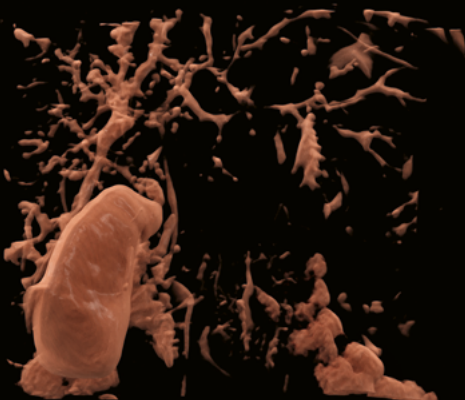


MReadings: Liver MRI

Contributions from our MAGNETOM users

siemens-healthineers.com/magnetom-world



Liver cancer care pathway



Liver cancer care pathway



Screening & Early Detection

3 Case Series: Clinical Application in Liver Fat and Iron Quantification using LiverLab

Barbara Frittoli, et al.
ASST-Spedali Civili di Brescia, Italy

13 Magnetic Resonance Elastography of the Liver: Best Practices

Arunark Kolipaka, et al.
The Ohio State University, Columbus, OH, USA

22 Liver Magnetic Resonance Elastography in Children

Elżbieta Jurkiewicz, et. al.
Department of Diagnostic Imaging, The Children's Memorial Health Institute, Warszawa, Poland

Treatment Planning & Delivery

58 4D-MRI for Treatment Planning of Liver Tumors

Jessica Scholey et. al.
Department of Radiation Oncology,
University of California, San Francisco, CA, USA

Diagnosis & Therapy Decision

28 Fast and Reliable Liver Imaging Using Deep Learning HASTE

Alain Luciani, Sébastien Mulé, et al.
Service d'Imagerie Médicale, AP-HP, Hôpitaux Universitaires Henri Mondor, Créteil, France

35 Fast, Standardized, and Robust Imaging with BioMatrix and Compressed Sensing GRASP-VIBE

Johan Dehem
VZW Jan Yperman, Ypres, Belgium

43 Fast and efficient liver imaging with Primovist®/Eovist®

Gregor Thörmer
Siemens Healthineers, Erlangen, Germany

49 Reduced Stress and Consistent Contrast enhanced MRI Scans with Precisely Timed, Automated Injection Enabled by MR-Injector Coupling

Gregor Thoermer
Siemens Healthineers, Erlangen, Germany

53 New Advances in Radiomics of Liver Imaging

Roberto Cannella, Tommaso Vincenzo Bartolotta
Section of Radiology – BiND, University Hospital "Paolo Giaccone", Palermo, Italy



Case Series: Clinical Application of Liver Fat and Iron Quantification using LiverLab

Barbara Frittoli, M.D.¹; Martina Bertuletti, M.D.¹; Valentina Angelini, M.D.²; Luigi Grazioli, M.D.¹

¹ASST-Spedali Civili di Brescia, Italy

²"Federico II" University, Naples, Italy

Background

In western countries in the last ten years, nonalcoholic fatty liver disease (NAFLD) has increased in incidence and prevalence, as has its advanced form, nonalcoholic steatohepatitis (NASH). These are complex metabolic alterations of liver function and structure. They have long term impacts on health and quality of life, raising the risk of cirrhosis and hepatocellular carcinoma. In the USA they are now the second indication for liver transplantation [1–5].

It has therefore become necessary to characterize and quantify the liver reversible modifications such as intrahepatic fat and iron overload associated with NAFLD and NASH. The ability to quantify liver fat will also benefit patients with chemotherapy-associated-steatohepatitis (CASH); and quantifying iron accumulation can benefit those with hemochromatosis, hemosiderosis, and chronic hepatopathy diseases [1–5].

These overload diseases usually have heterogeneous distribution within the liver, which is a challenge for liver biopsy. Biopsy is still considered by clinicians as the gold standard for diagnosis and quantification, despite being invasive. However, biopsy does not always show the real severity of the disease and its distribution within the parenchyma because it samples only one or a few sites.

Various noninvasive qualitative and quantitative techniques can be used to quantify liver steatosis, including ultrasound and computed tomography; but MRI is the most accurate and reproducible technique. MRI is also the only accurate method for detecting iron overload in the liver.

In recent years, software has been developed to automatically manage quantitative measurements and represent them with color parametric maps, which has simplified the use of quantitative MR imaging in everyday clinical practice [6].

Recent MRI methods for liver fat and iron quantification in the liver are based on the Dixon technique and spectroscopy. These methods are available as LiverLab on our magnetic resonance tomographs 1.5T MAGNETOM Aera and 3T MAGNETOM Skyra (Siemens Healthcare, Erlangen, Germany).

LiverLab comprises a fat and iron screening component (two-point e-Dixon), and two methods for evaluation: multi-echo Dixon VIBE (six point q-Dixon), an image-based method; and HISTO, a voxel-based spectroscopic method. It also provides clinical reports. In our experience with LiverLab, we take advantage of its very fast acquisition, reproducibility of results and interpretation immediacy [7, 8].

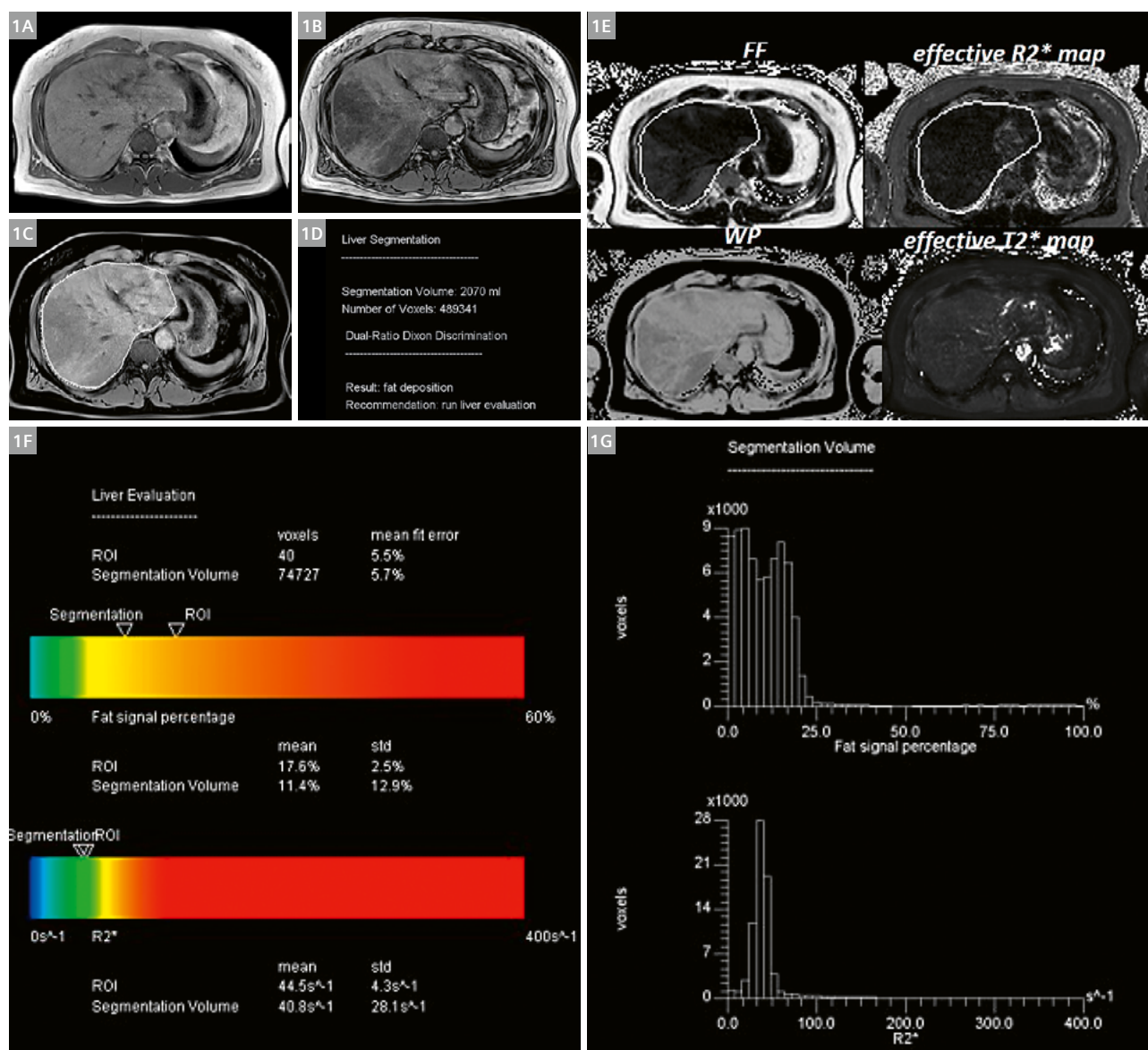
For our patients undergoing MR liver examination, the first sequences acquired during our liver protocol are T1 GRE in/opp. If liver signal intensity is hypointense in in-phase or opposed-phase acquisition, LiverLab is acquired before contrast media administration, in order to identify and quantify fat and/or iron deposition. It takes about 5–7 minutes if both Multi-echo Dixon VIBE and HISTO are acquired, and doesn't alter the regular workflow. Some hepatopathic and hematological patients are scheduled only for LiverLab acquisition by Hepatologists and Hematologists and then the complete MR examination takes about 10 minutes, with T2* map added to the protocol.

In our experience, LiverLab has become routinely useful in evaluating liver overload diseases in many clinical assets, bringing the advantages of rapid, accurate and reproducible acquisition. Here we show examples, in patients with fat accumulation (NAFLD/NASH, liver chronic hepatopathy, CASH in oncological patients), iron accumulation (hemochromatosis, hemosiderosis), and both (NAFLD/chronic hepatopathy). This technique is useful for follow-up and drugs effect monitoring, due to easy and rapid administration and accurate measurement.

Case 1

50-year-old male with incidental finding of cholestasis and hypercholesterolemia. Ultrasound examination of the liver had very heterogeneous aspect, with hyperechoic areas and pseudonodular hypoechoic areas. The patient was

scheduled for an MRI examination to quantify steatosis and characterize pseudonodular lesions. Images were acquired by 1.5T MAGNETOM Aera.



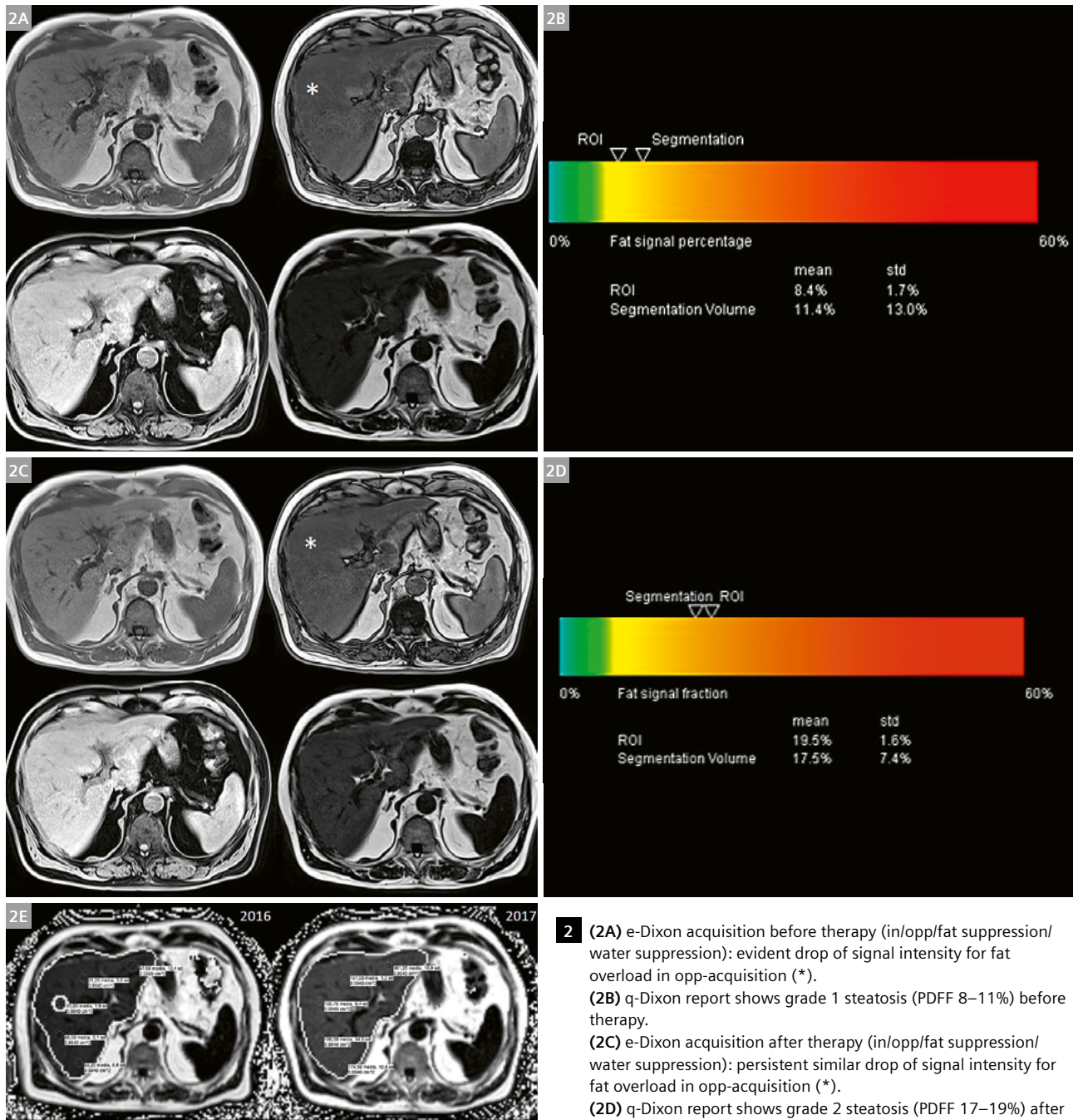
- 1 (1A) T1w GRE in-phase: liver of regular volume and morphology.
- (1B) T1w GRE opp-phase: heterogeneous drop of signal within the liver parenchyma, in particular in the right lobe where some hypointense areas have pseudonodular aspect.
- (1C) e-Dixon automatic liver segmentation.
- (1D) e-Dixon report estimates liver volume and number of voxels, and reports the presence of intrahepatic fat.
- (1E) Four of the five series of images from q-Dixon acquisition: FF (Fat Fraction), WF (Water Fraction), effective R2*, effective T2*.
- (1F) q-Dixon report: color bars show the values of PDF and R2* both for the whole liver volume segmented and for the ROI positioned in the right lobe. ROI value for PDF is higher (17.6%) than segmentation value (11.4%) because of major fat accumulation in right lobe. Classification is grade 1–2 steatosis; R2* values are normal; no iron overload is detected.
- (1G) q-Dixon report: histograms describe PDF values and R2* values distribution.



Case 2

56-year-old male with steatosis. The patient was enrolled in a double-blind study in which steatosis was quantified by LiverLab performed on 3T MAGNETOM Skyra, before and after one year of therapy (drug versus placebo).

Qualitative imaging (in/opp or e-Dixon) could not correctly identify variation in fat overload; quantitative imaging (q-Dixon) could identify and measure PDFF before and after drug/placebo administration.

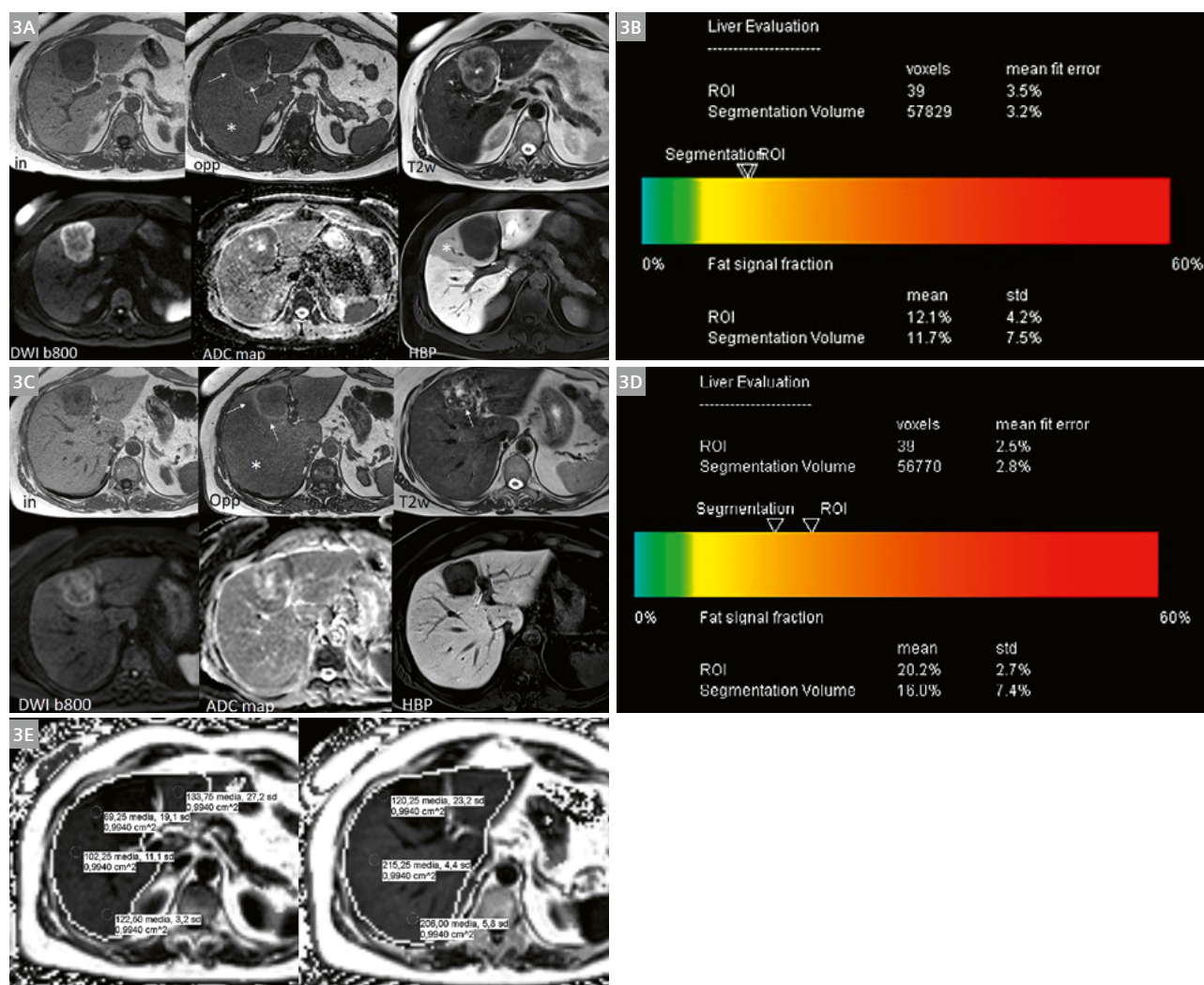


- 2** (2A) e-Dixon acquisition before therapy (in/opp/fat suppression/ water suppression): evident drop of signal intensity for fat overload in opp-acquisition (*).
 (2B) q-Dixon report shows grade 1 steatosis (PDFF 8–11%) before therapy.
 (2C) e-Dixon acquisition after therapy (in/opp/fat suppression/ water suppression): persistent similar drop of signal intensity for fat overload in opp-acquisition (*).
 (2D) q-Dixon report shows grade 2 steatosis (PDFF 17–19%) after therapy.
 (2E) q-Dixon FF series before and after therapy: multiple ROIs positioned in right liver lobe confirm PDFF values reported on colored bars.

Case 3

48-year-old female with single liver metastasis in S4 in obese patient with rectal cancer studied by MRI. The patient underwent chemotherapy and repeat MRI after three months to evaluate response to therapy: partial response was assessed but steatosis worsened and the patient could

not go on with chemotherapy because of CASH. The multi-disciplinary team decided to perform surgery "liver-first". The pathologic examination of liver surrounding resected metastasis confirmed grade 2 steatosis.



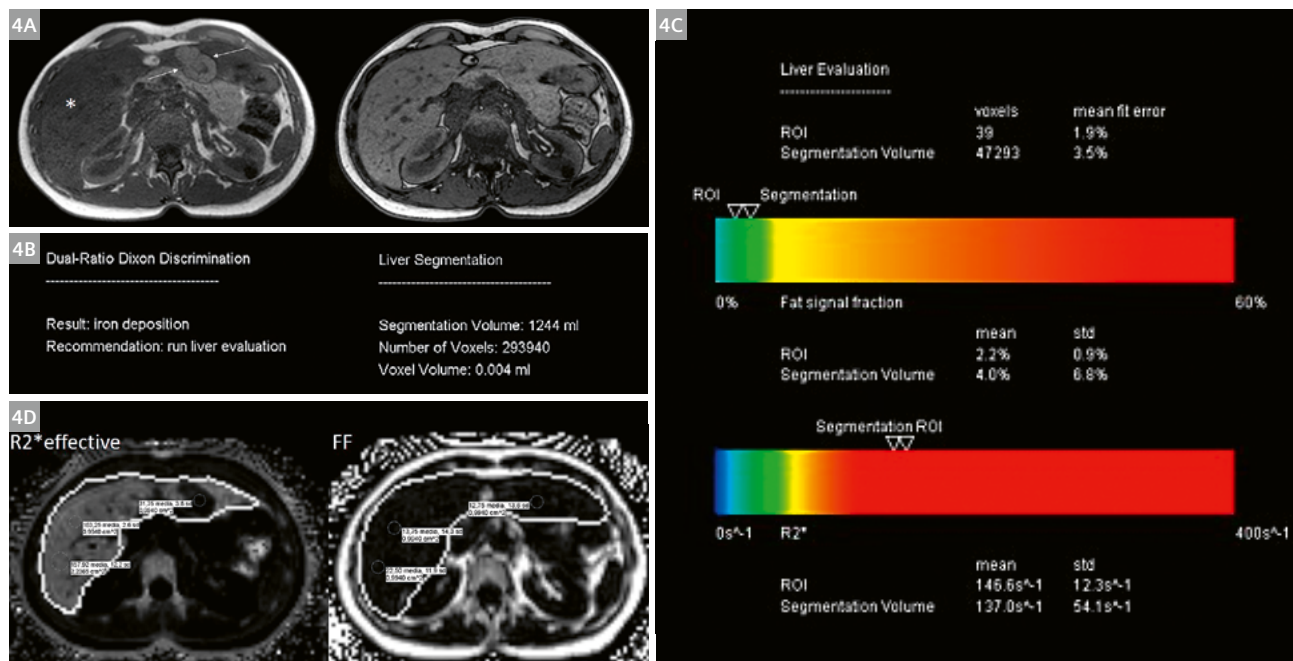
- 3** (3A) in-/opp, T2w, DWI (b800), ADC and hepatobiliary phase (HBP 15 min after EOB-DTPA injection) of the hepatic lesion at the initial staging: liver diffuse steatosis (* in opp); the lesion determines compression on left portal branch with consequent perilesional steatosis spare (arrows) and functional liver impairment (* in HBP).
 (3B) q-Dixon report shows grade 1 steatosis (PDF 11–12%) before chemotherapy.
 (3C) in-/opp, T2w, DWI, ADC and HBP (15 min after EOB-DTPA injection) of the hepatic lesion after chemotherapy: liver diffuse steatosis persists (* in opp); the lesion is smaller but perilesional steatosis spare is still evident (arrows in opp); the signal of the lesion in T2w sequence is more heterogeneous (arrow) without any restriction of signal on DWI/ADC. The functional liver impairment is no easier to see during HBP.
 (3D) q-Dixon report shows worsening of steatosis (grade 2, PDF 16–21%) after chemotherapy.
 (3E) q-Dixon FF series before and after (*) therapy: multiple ROIs in right liver lobe confirm PDF values reported on colored bars of q-Dixon report.



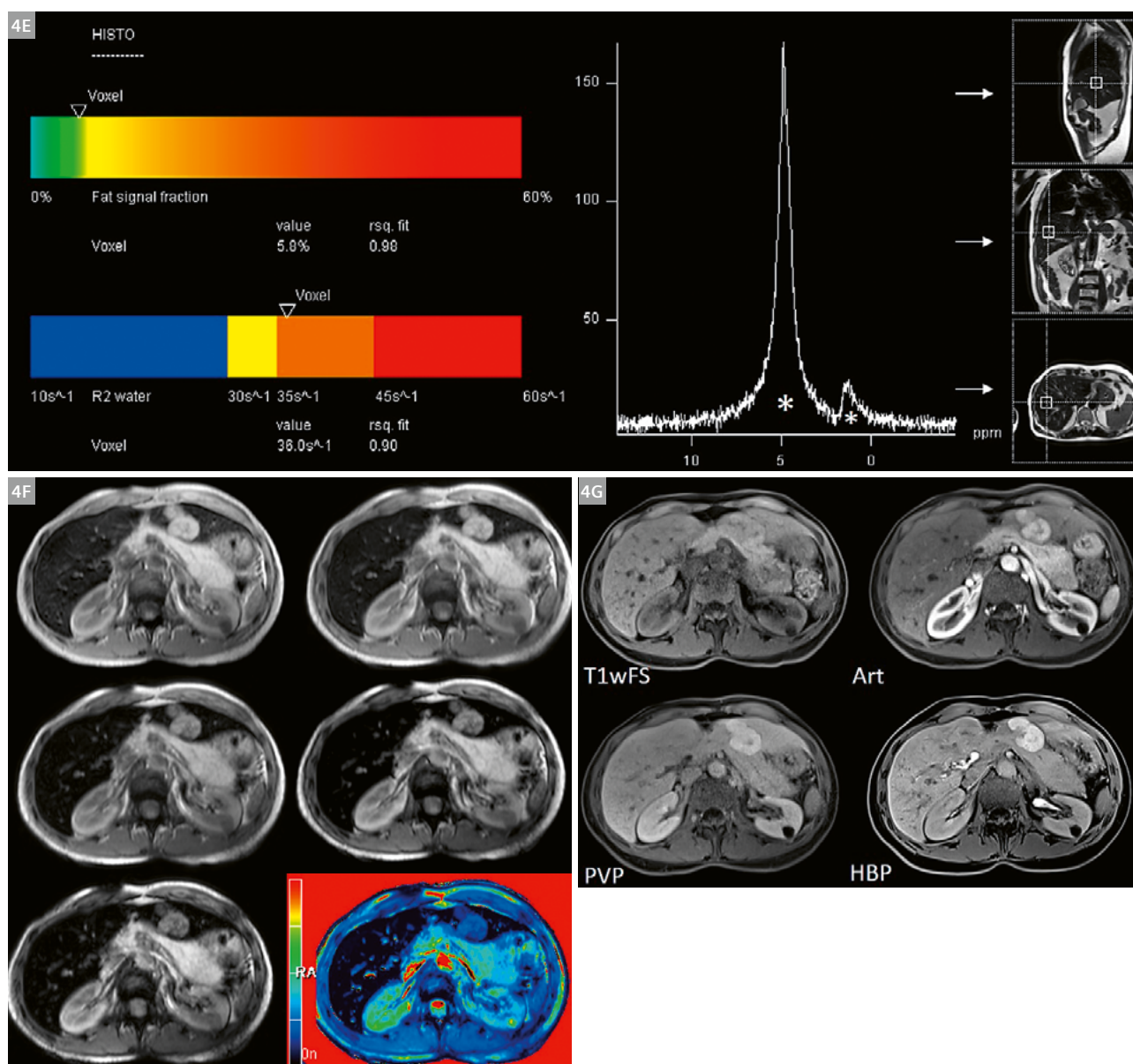
Case 4

43-year-old female with incidental ultrasound finding of hypoechoic lesion in left lobe in hyperechoic liver – suspected steatosis. The patient was scheduled for MRI. With T1 GRE in/opp sequences, more hypointense signal of liver parenchyma was noted on T1 in-phase sequence. LiverLab was performed, and confirmed mild iron overload

(LIC 4.4–4.7 mgFe/g). The lesion in the left lobe had signal intensity and pattern of enhancement typical for focal nodular hyperplasia (FNH). The patient was given specific blood tests, and heterozygosity for hemochromatosis was confirmed.



- 4** (4A) T1 GRE in/opp sequence: the signal intensity of liver parenchyma is lower in in-phase acquisition (*); in the left lobe an exophytic lesion shows as isointense in opp-phase and hyperintense in in-phase (arrows).
 (4B) e-Dixon report confirms iron overload and provides an estimation of liver volume.
 (4C) q-Dixon report shows mild iron overload, with R2* of 137–147 sec⁻¹, corresponding to LIC of 4.4–4.7 mgFe/g. PDFF is normal (<5%).
 (4D) q-Dixon R2*effective and FF sequences: multiple ROIs in right liver lobe confirm R2* and PDFF values reported on colored bars. No fat or iron overload can be detected within the lesion in the left lobe.



4 (4E) HISTO acquisition report confirms iron overload ($R2 \text{ water } 36 \text{ sec}^{-1}$; normal values $<30 \text{ sec}^{-1}$) in the single voxel measured in right lobe (arrows indicate the site of the measured voxel in multiplanar vision). Asterisks represent T2-corrected peak areas for water and fat at each measured TE.

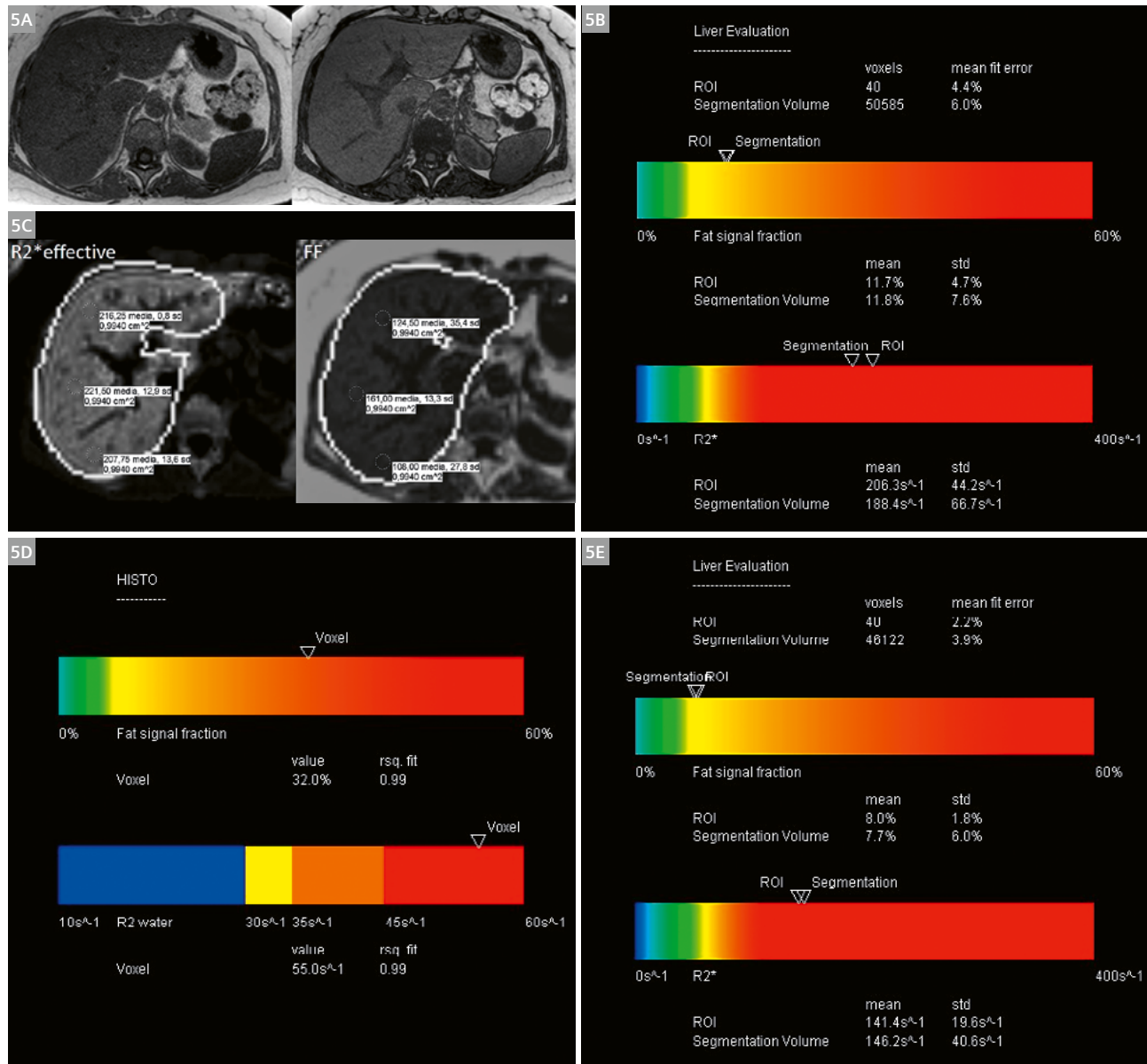
(4F) T2* multi-echo acquisition (TE = 9,53 – 14,29 – 19,05 – 23,81 and 28,58 seconds) and T2* colored map.

(4G) Characterization of the liver lesion before (T1w FatSat) and after contrast media administration (EOB-DTPA) during dynamic (arterial and portal venous phase) and hepatobiliary phase (HBP): focal nodular hyperplasia (FNH).

**Case 5**

68-year-old female with hemosiderosis. The patient undergoes MRI (LiverLab) to quantify iron overload and evaluate whether chelation therapy should be performed. After seven bloodletting sessions the patient was scheduled for

LiverLab acquisition, which showed reduction of iron overload. Mild steatosis was associated with iron overload, and fat accumulation was reduced after therapy.

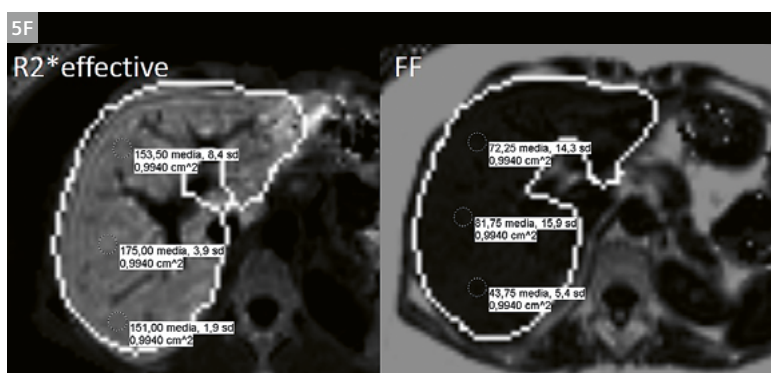
**5 (5A) T1 GRE in/opp sequences**

(5B) q-Dixon report shows iron overload, with R2* of 190–206 sec⁻¹, corresponding to LIC of 6.1–6.6 mgFe/g; and mild steatosis (PDFF 11–12%).

(5C) q-Dixon R2*effective and FF series: multiple ROIs positioned in right liver lobe confirm high R2* values (up to 221 sec⁻¹) and heterogeneous mild steatosis (PDFF 10–16%).

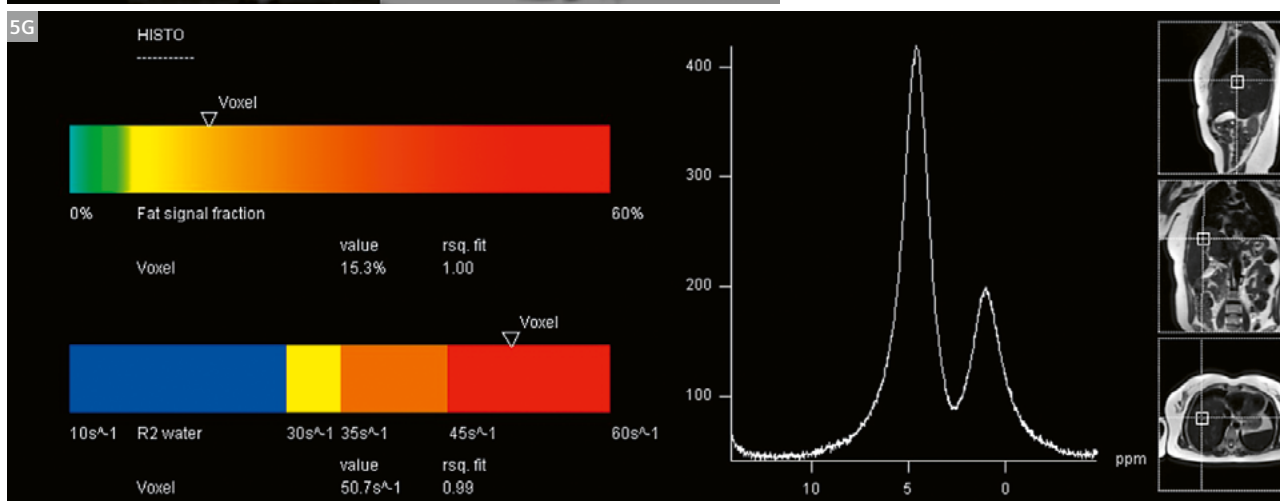
(5D) HISTO acquisition report confirms iron overload and steatosis: R2 water 55 sec⁻¹ (normal values < 30 sec⁻¹) in the single voxel measured in right lobe. PDFF is 32% in the same voxel. According to literature, steatosis can be overestimated in presence of iron overload [14].

(5E) After bloodletting therapy, q-Dixon acquisitions demonstrate reduction in iron overload and steatosis: R2* is 145 sec⁻¹, corresponding to LIC of 4.64 mgFe/g. Steatosis is reduced (PDFF 7–8%).



(5F) q-Dixon R2* effective and FF series: multiple ROIs in right liver lobe confirm high R2* values (up to 175 sec⁻¹) and mild steatosis (PDFF 7–8%) with areas of relative spare (PDFF 4.3% in S6).

(5G) HISTO confirms the effect of the therapy: R2 water is 50.7 sec⁻¹ (normal values < 30 sec⁻¹) in the single voxel measured in right lobe. PDFF is 15% in the same voxel.



Technique

The first sequence is an e-Dixon, obtained in a single 15–20 second breath-hold acquisition, which returns four series of images: in/opp/fat suppression/water suppression. It gives a semi-quantitative evaluation of fat and iron buildup by estimating the total number of voxels (and the volume in mL of the hepatic parenchyma) and the presence of fat and/or iron in the parenchyma.

The six-point acquisition q-Dixon, obtained in a 18–20 second breath-hold acquisition, is a 3D multi-echo gradient echo sequence with Dixon reconstructions and correction for T2* in the presence of iron. It returns five series of images: FF (fat fraction), WF (water fraction), effective R2*, effective T2* and goodness-of-fit map for quality control. It also plots the distribution of measured echo times, and gives a graphical representation with color bars or colorimetric maps of the two biomarkers: PDFF (proton density fat fraction) and R2* (1/T2*), both as average values calculated over the entire liver volume and as single voxel measurements.

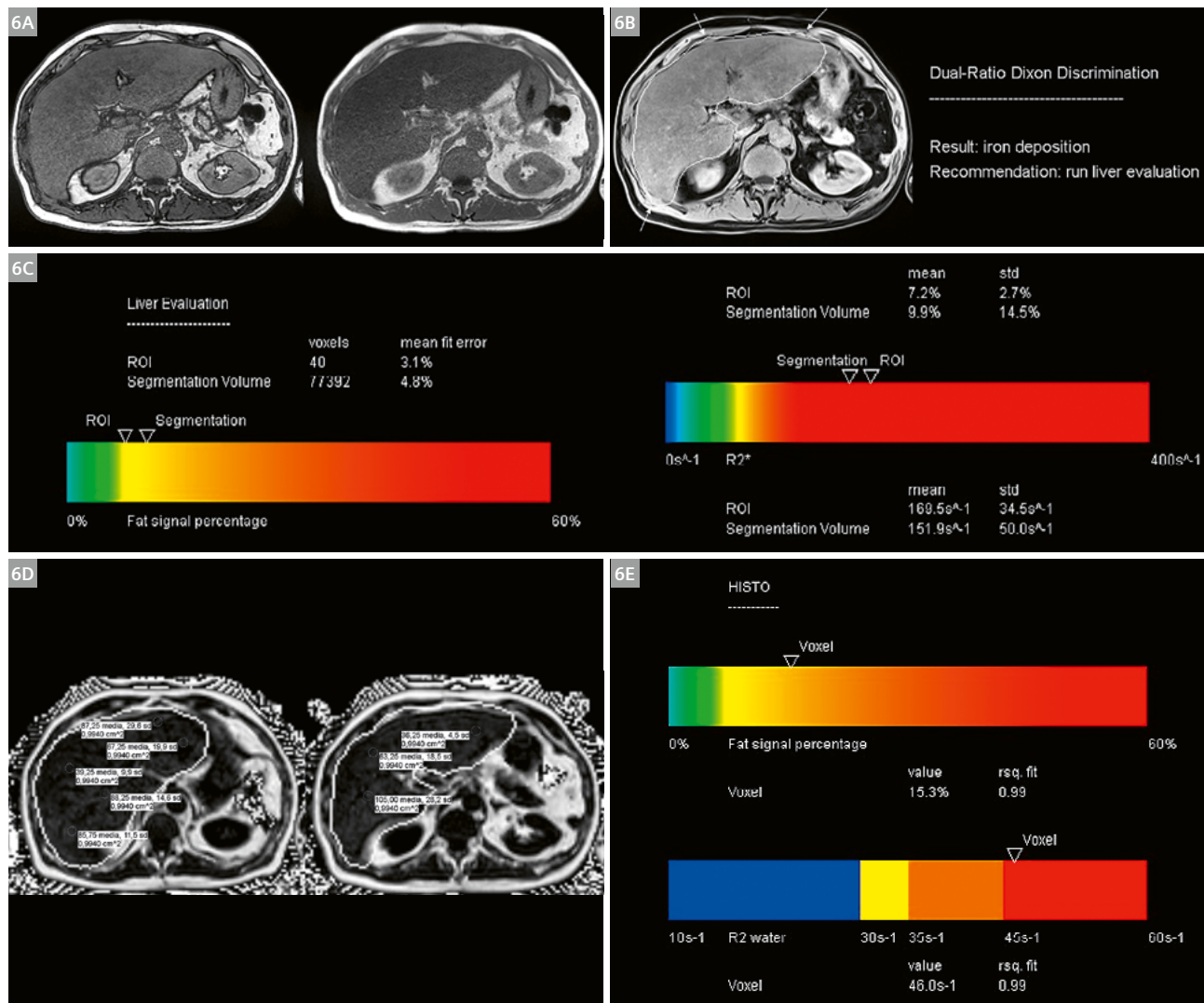
During postprocessing, PDFF and R2* can also be measured in each desired voxel of the liver, by placing the region of interest (ROI) in the most interesting hepatic segments in the FF and effective R2* series. In this way an estimate of steatosis can be made for each part or lobe, which is useful if the patient must undergo liver resection [9].

The FF value multiplied by 10⁻¹ corresponds to the PDFF value in that location. This makes it possible to classify steatosis in a very accurate manner: grade 0 (normal liver PDFF: 0–5%), grade 1 (mild PDFF: 5–17%), grade 2 (moderate PDFF: 17–22%), and grade 3 (severe PDFF: ≥ 22%).

The effective R2* is measured in Hertz (or sec⁻¹) and correlates to the value of LIC (liver iron concentration) through a specific conversion factor for each device. The LIC is the ratio of intrahepatic iron to the dry weight of the parenchyma. Normal LIC is < 1.8 mg/g (dry weight). Values between 3 and 7 indicate a mild iron overload, > 7 moderate, and > 15 severe. A LIC value of 7 mg/g is an indication for chelation therapy in patients with iron overload due to repeated blood transfusions [10–12].

**Case 6**

66-year-old male with recent detection of liver cirrhosis; no viral causes were documented and the patient denied any alcohol abuse. NASH-related cirrhosis was suspected, so LiverLab evaluation was requested.



The HISTO spectroscopy sequences are multi-echo sequences corrected for the T2 signal, at high speed, acquired on a single voxel. These sequences are based on the principle that there is a strong nonlinear correlation between the water R2 signal and the iron concentration, independent of the lipid concentration. The sequence contains an algorithm that integrates the water and fat signal for each TE acquired, and can be used to obtain the values of fat fraction and water R2 [13].

Three localizer sequences define the location of the voxel, and then an apnea sequence of about 18–20 seconds returns a spectrum of the shorter TEs to perform quality control of the values obtained at TE = 12 seconds, where two distinct peaks must be appreciated: water and fat. The sequence also shows the measured values of fat fraction and R2 water on color bars. If desired, the acquisition can be repeated in another voxel of your choice.

A T2* colored map can also be obtained by acquiring multi-echo T2* sequences.

Conclusion

These cases show how LiverLab can give a wealth of information to clinicians, useful for diagnosis, management and follow-up of patients with fat and/or iron liver overload. With its rapid acquisition (5–7 minutes) it can easily be integrated in a standard liver MRI protocol. Radiologists' skills in using and interpreting LiverLab acquisitions and measurements can improve rapidly once these sequences are added to the standard protocol in patients with hepatopathy. In our experience clinicians appreciate the information given about fat and/or iron liver overload, and ask for this type of evaluation more and more frequently.

Contact

Barbara Frittoli, M.D.
Radiologia 1 ASST-Spedali Civili di Brescia
p.le Spedali Civili 1
25123 Brescia
Italy
bfrittoli@gmail.com



References

- 1 Xiaozhou M, Nagaraj-Setty H, Kambadakone R, Kenudson-Mino M, Hahn PF, Sahani DV. Imaging based Quantification of Hepatic Fat: Methods and Clinical Applications. *RadioGraphics*. 2009;29(5):1253-1280.
- 2 Caussy C, Reeder SB, Sirlin CB, Loomba R. Noninvasive, Quantitative Assessment of Liver Fat by MRI-PDFF as an Endpoint in NASH Trials, *Hepatology*. 2018;68(2):763-772.
- 3 Mouzaki M, Trout AT, Arce-Clachar AC, Bramlage K, Kuhnell P, Dillman JR et al. Assessment of Nonalcoholic Fatty Liver Disease Progression in Children Using Magnetic Resonance Imaging. *The Journal of Pediatrics*. 2018;201:86-92.
- 4 Yu EL, Golshan S, Harlow KE, Angeles JE, Durelle J, Goyal NP et al. Prevalence of Nonalcoholic Fatty Liver Disease in Children with Obesity. *The Journal of Pediatrics*. 2018; in press, available online since 14 Dec 2018 from <https://www.sciencedirect.com/journal/the-journal-of-pediatrics/articles-in-prepress>.
- 5 Deng J, Zhong X, Fishbein M et al. Hepatic Fat Quantification in Pediatric Patients using Multi-echo Dixon VIBE: Early Experience. *MAGNETOM Flash*. 2015;2(62):23-25.
- 6 Hutton C, Gyngell ML, Milanese M, Bagur A, Brady M. Validation of a standardized MRI method for liver fat and T2 quantification. *PLoS ONE*. 2018;13(9):e0204175. <https://doi.org/10.1371/journal.pone.0204175>
- 7 Sharma P, Martin D. An Efficient Workflow for Quantifying Hepatic Lipid and Iron Deposition using LiverLab. *MAGNETOM Flash*. 2014;3(58):12-17.
- 8 Sellers R. MR LiverLab. *MAGNETOM Flash*. 2016;3(66):39-43.
- 9 Kim HJ, Cho HJ, Kim B, You MY, Lee JH, Huh J et al. Accuracy and precision of proton density fat fraction measurement across field strengths and scan intervals: A phantom and human study. *Journal of Magnetic Resonance Imaging*. 2018; in press, available online since 14 Nov 2018 from <https://onlinelibrary.wiley.com/toc/15222586/0/0>
- 10 Wood JC. Use of magnetic resonance imaging to monitor iron overload. *Hematol Oncol Clin North Am*. 2014;28(4):747-64.
- 11 Henninger B, Zoller H, Rauch S, Finkenstedt A, Shockey M, Jaschke W et al. R2* relaxometry for the quantification of hepatic iron overload: biopsy based calibration and comparison with the literature. *RoFo*. 2015;187(6): 472-479.
- 12 Quinn C, St Pierre T. MRI Measurements of Iron Load in Transfusion-Dependent Patients: Implementation, Challenges, and Pitfalls. *Pediatr Blood Cancer*. 2016;63:773–780.
- 13 Reeder SB, Cruite I, Hamilton G, Sirlin CB. Quantitative assessment of liver fat with magnetic resonance imaging and spectroscopy. *J. Magn. Reson. Imaging*. 2011;34:729-749.
- 14 Pineda N, Sharma P, Qin Xu, Hu X, Vos M, Martin DR. Measurement of Hepatic Lipid: High-Speed T2-Corrected Multiecho Acquisition at 1H MR Spectroscopy—A Rapid and Accurate Technique. *Radiology*. 2009;252(2):568-576. <https://doi.org/10.1148/radiol.2523082084>.



Magnetic Resonance Elastography of the Liver: Best Practices

Manjunathan Nanjappa, Ph.D.¹; Bradley Bolster, Ph.D.²; Ning Jin, Ph.D.²; Stephan Kannengießer, Ph.D.³; Robert Sellers, RT(R)(MR)(CT)²; Arunark Kolipaka, Ph.D., FAHA, FSCMR¹

¹The Ohio State University, Columbus, OH, USA

²Siemens Healthineers, US MR R&D Collaborations, Malvern, PA, USA

³Siemens Healthineers, MR DL ONCO, Erlangen, Germany

Introduction

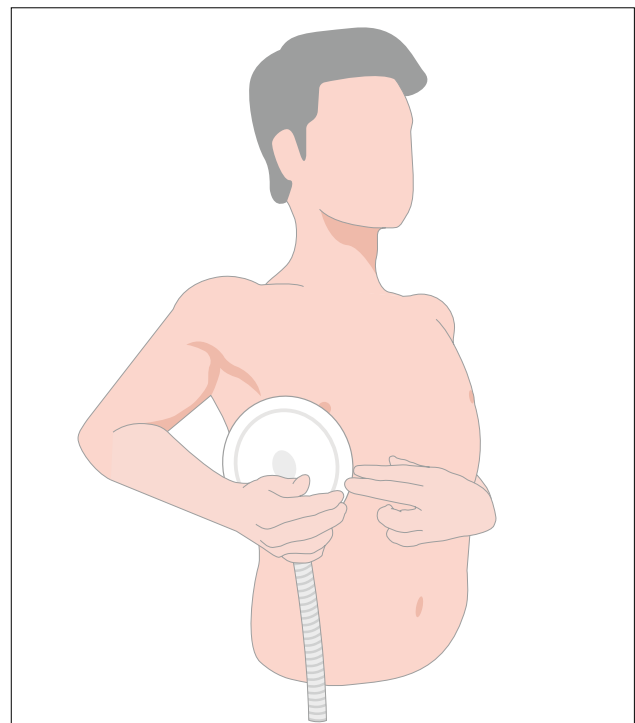
Liver is the largest solid internal organ of the human body. It performs a wide range of functions including aiding digestion, storing energy, removing metabolic waste and microorganisms from the circulatory system, and producing blood-clotting components. The liver can repair, regenerate and/or regrow itself to maintain its structure and functions, yet certain health conditions can overwhelm these capabilities leading to the progression of liver disease [1]. Alcohol abuse, obesity, and chronic illness can lead to excessive accumulation of extracellular matrix proteins including collagen. This results in diminished blood flow and the subsequent build-up of scar tissue in the liver known as liver fibrosis [2].

Liver fibrosis in its initial and moderate stages causes no clinical symptoms by itself and can often be missed by routine blood tests or by medical imaging examinations. Fibrosis can be treated and reversed on early detection; however, if this condition is left untreated for a long time, it may lead to a severe condition called cirrhosis. Once cirrhosis has developed, clinical symptoms and their associated problems may begin to appear, and eventually liver damage becomes permanent and irreversible [3]. Therefore, early detection of liver fibrosis plays an important role in treatment and disease management.

Traditionally, liver fibrosis is diagnosed and staged by percutaneous liver biopsy, an invasive technique. Lately, non-invasive methodologies such as blood serum tests and medical imaging techniques have emerged as an alternative to biopsy. However, serum tests such as APRI, FIB-4, and other commercial assays have proven less accurate than the imaging modalities [4] such as ultrasound (US) elastography and magnetic resonance elastography (MRE) for staging fibrosis. Several studies comparing MR- and US-based elastography techniques concluded that the MRE has been shown to exceed all other diagnostic methods in terms of accuracy, sensitivity, specificity, and organ coverage [5].

Magnetic Resonance Elastography

MRE is a non-invasive technique to estimate the stiffness of soft tissues. Given the non-invasive nature and accuracy of diagnostic results, in recent years MRE has become a standard clinical tool to stage liver fibrosis on both 1.5T and 3T scanners [6]. MRE can be acquired with or without contrast agent on board [8], meaning it can be performed at any point in a standard clinical examination, depending on site preference.



1 Illustration of the passive driver placement for liver MRE imaging. The entire flat surface of the drive should be in contact with the subject's upper abdomen at the fifth intercostal space and lateral to the mid-clavicular line.



The liver MRE technique can be separated into four elements as described below.

1. Inducing shear wave motion into the liver using an external mechanical driver
2. Acquiring wave images of the liver via motion encoding and phase-contrast imaging
3. Reconstructing stiffness maps from the wave images using an inversion algorithm
4. Reporting average stiffness values in ROIs identified in the liver stiffness maps as having good wave quality and no artifacts

Liver MRE has been described in a QIBA profile [10], which also gives practical guidance for performing MRE and interpreting the results. Conformance to this profile supports the claim that a change in measured hepatic stiffness of at least 19% is considered to be real with 95% confidence.

This article reviews the essentials of MRE and provides best practice for its routine clinical usage. To clinicians, the MRE technique offers the special benefit that all major MR manufacturers adopted the same standard solution, hardware and inversion algorithm, and high reproducibility has been demonstrated [6]. This uniformity makes the interpretation of diagnostic results much easier, especially in centers where multiple platforms are used. However, some image acquisition sequences and workflow options may differ, so in the following, the focus will be on the Siemens Healthineers platform.

The most commonly used and commercially available solution (Resoundant Inc, Rochester, MN, USA) induces continuous single frequency mechanical shear wave motion in the liver using a special hardware complement to the MR system that consists of an active driver (frequency generator) and a passive driver (plastic drum), and a standardized inversion algorithm implementation [17].

Insert 1: Best practice workflow

Pay attention to the following workflow elements to improve chances of performing a high quality MRE exam.

1. Inspect the hardware regularly for any damage to the passive driver diaphragm, or air leakage in the tubing system.
2. Turn the active driver (off and) on prior to each examination to wake it up from standby mode.
3. Place the elastic belt on the MR patient table at liver level and position the patient in a supine position with head-first. Position and secure the passive driver as explained in the section *Driver setup for liver MRE*. Lateral placement is preferred over anterior placement but good contact between the driver face and the subject's abdomen is critical.
4. Direct the end of the passive driver tubing towards where it will connect to the tubing from the active driver. In some cases this may be at the back of the bore.
5. Fasten the belt tightly. Ask the subject if they can breathe normally with the belt; if not, adjust the belt. Inform them about expected examination duration, order of sequences, that the Elastography is performed at end-expiration, and that they will feel vibrations coming from the driver during the activation. Repeat the latter to the patient just before the MRE sequence to avoid them being startled.
6. Verify passive driver positioning in scout images in relation to the liver at end-expiration and other landmarks. Adjust the driver as necessary.
7. Run the MR Elastography sequence and acquire the images at end-expiration.
8. Load the results into the Viewing Task Card and review image quality as described in the section *Postprocessing and evaluation* (magnitude for breathing artifacts, wave images for good propagation along with depth penetration, and confidence mask for successful inversion). In case of insufficient quality, check driver positioning and repeat, using a modified protocol where appropriate, e.g., in case of iron overload.
9. Measure stiffness via ROI evaluation as described in the section *Postprocessing and evaluation*.



Driver setup for liver MRE

Positioning of the passive driver on the subject (Figure 1) is one of the most critical steps in an MRE examination. Optimal driver positioning ensures that the externally generated mechanical waves are transferred to the subject efficiently and thereby penetrate deep into the liver. This helps achieve the desired anatomical coverage and obtain stiffness measurements with high quality.

To enable the performance of reliable human liver MRE, the passive driver is placed on the upper abdomen centered at the fifth intercostal space but lateral to the midclavicular line as shown in Figure 1. While positioning the passive driver it is necessary to make sure that the driver's flat surface area is fully in contact with the body close to the liver.

To maintain the passive driver in one fixed position throughout the imaging session, it is necessary to immobilize it with a dedicated elastic belt firmly while ensuring the subjects' comfort to breathe normally. To improve contact between the subject and the passive driver it is advisable to use extra cushioning material such as a sponge or clothing materials (as shown in Figure 2) in between the passive driver and the belt to tightly hold the driver against the body. This enables mechanical waves to be delivered to the region of interest uniformly throughout the imaging session. Finally, it is important to ensure that the passive driver is connected tightly to the active driver via plastic tubing so that there is no air leakage. It may be advantageous to connect the remaining tubing only after the subject has been moved into the scanner.

After placing the driver, it is important to verify that the driver is positioned correctly, i.e., centered in H-F direction with respect to the liver. If collected at end expira-

tion localizer images of sagittal and axial views like those in Figure 3 will show the placement of the driver. The indentation on the sagittal view indicates that the driver is placed at the center with respect to the liver. Similarly, the axial view will show the indentation anterior to the liver. If the position of the driver is not correct, then the driver must be adjusted with respect to these landmarks.

Sequence optimization and image acquisition

The Siemens Healthineers MRE product consists of two sequence options, a GRE based sequence with an optional rapid acquisition mode (see Figure 4) and a sequence based on single-shot spin-echo echo planar imaging (SE-EPI). Both sequences acquire 2D axial slices in the center of the liver at end-expiration with through-slice motion encoding and include a fractional encoding option to shorten TE (Figure 4). The SE-EPI MRE acquisition is more efficient and should be the default acquisition where possible. The primary benefit of SE-EPI is that multiple slices are acquired in a single 11–13 seconds breath-hold and the SE-EPI component makes the sequence more robust to susceptibility that occurs with liver iron loading or with higher field strengths. Fat saturation is very important for SE-EPI; SPAIR-strong is the preferred fat suppression setting for this sequence. GRE MRE requires multiple breath-holds (one per slice), however, in some situations such as where implants exist and lower radio frequency flip angles are necessary, or if referencing previous GRE MRE studies, it can be the sequence of choice. Standard imaging parameters for the two sequences are shown in Table 1 and the standard Siemens Healthineers protocol tree for



2 Demonstration of MRE setup and driver placement for liver imaging, using the dedicated elastic belt, plus cushioning material (arrow).

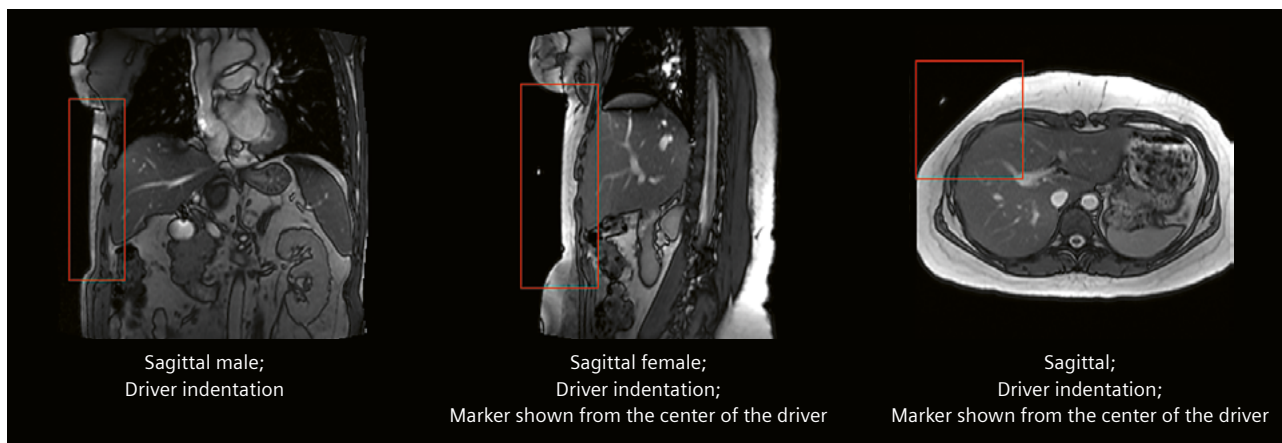
Watch the videos on <https://www.magnetomworld.siemens-healthineers.com/clinical-corner/protocols/body-pelvis/mr-elastography>

MR Elastography is shown in Figure 5. As previously mentioned, an MRE protocol can be added either at the beginning (pre-contrast) or the end (post-contrast) of a measurement program.

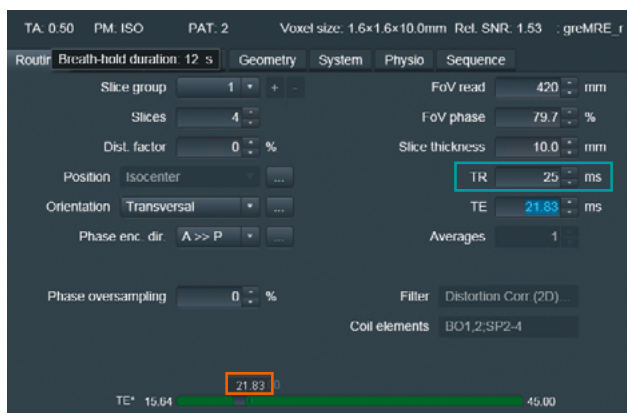
The mechanical excitation frequency is fixed at 60 Hz, and the amplitude of the active driver is typically set to 40%, which will work well, irrespective of body habitus, in 85% of the patients. If the current driver amplitude should lead to either too much or too little motion encod-

ing, some control over the motion encoding strength is possible using the Gradient mode UI parameter, since the amplitude of the motion encoding gradient (MEG) will scale with it: It is lower for Normal and higher for Fast Gradient mode.

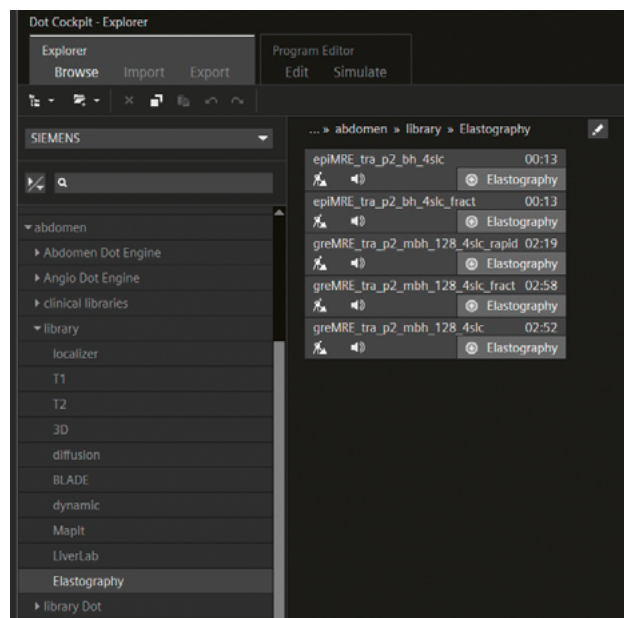
The active driver is activated ("triggered") via the sequence, and automatic breath-hold commands can be used. Make sure that both MRE and the localizer are acquired in end-expiration.



- 3 Localizers illustrating the driver placement for an optimized MRE liver examination. Positioning the driver center to the liver facilitates uniform propagation of waves in the region of interest. (An MR visible fiducial has been added to the passive driver in this case showing the center of the passive driver in these images.)



- 4 Example parameter card for a GRE MRE protocol in Rapid mode (TR 25 instead of 50 ms, petrol highlight). Shortening the TE below the gap in the range bar (orange highlight) would activate fractional motion encoding (which may boost signal at the expense of sensitivity, but this is only recommended for cases with short T2*).



- 5 The Siemens Healthineers protocol tree for Elastography representing all MRE options: epiMRE with and without fractional encoding, and greMRE in its standard, rapid and fractional encoding configuration.



Parameter	SE-EPI MRE	GRE MRE
FOV	420 mm (x 100%)	420 mm x 70–100%
TR	1000–1200 ms	25 ^a or 50 ms
TE	47 ms or lower ^b	21 ms or lower ^b
Slice thickness	8 mm, 25% gap	10 mm, no gap
Acquisition matrix	100 x 100%	128 x 80%
Bandwidth	2170 Hz/pixel	399 Hz/pixel
Gradient Mode	Normal, Fast ^c	Normal, Fast ^c
GRAPPA factor	2	2
GRAPPA reference lines	24 GRE/separate	12 integrated
Fat saturation	SPAIR – strong	none
Other key settings	Prescan Normalize, Adaptive Coil Combination	

Table 1: Typical sequence parameters for MRE.

^aSelecting a TE of 25 ms will put the GRE MRE sequence into “Rapid” mode [14] (see Figure 4).

^bSelecting TE lower than the gap in the sequence UI (see Figure 4) will cause the motion encoding gradients to be shortened to 65% of full (“fractional” encoding [15]); this is beneficial for short T2 / T2*, but will also reduce motion encoding, so it is only recommended for problem-solving.

^cThe gradient mode will influence the motion encoding via the MEG amplitude; start with Normal, and if there is not enough motion encoding, go to Fast.

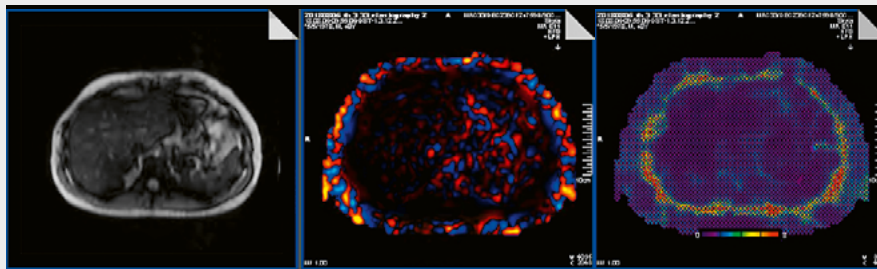
Protocols (.exar1 files) are available for download at

<https://www.magnetomworld.siemens-healthineers.com/clinical-corner/protocols/body-pelvis/mr-elastography>

Insert 2: Trouble shooting

No waves or inadequate waves in the liver (Figure 6)

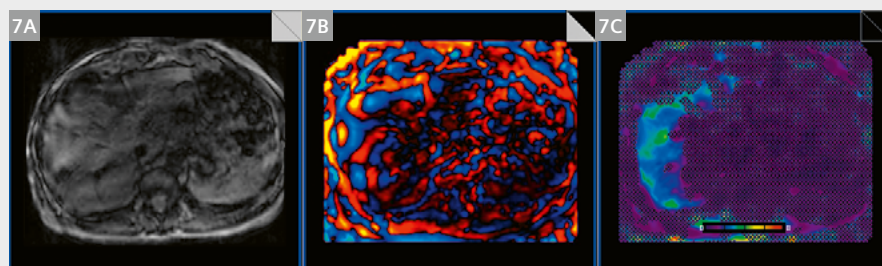
1. Check tubing for disconnection and pneumatic pressure leakage.
Make sure that the passive driver diaphragm (flat surface) is not damaged.
2. Make sure the passive driver has a good contact with the subject's body and is positioned correctly as shown in Figure 2.
3. Make sure the active driver is turned on and not in standby mode.



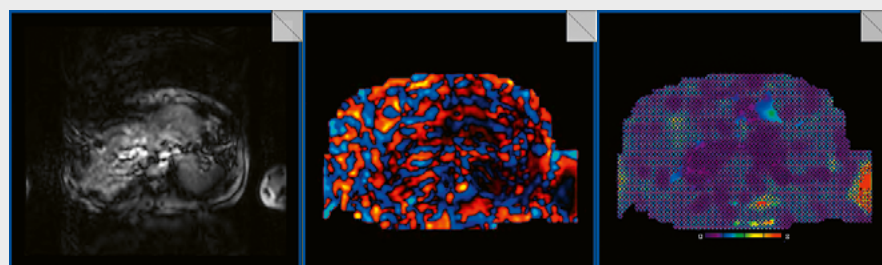
- 6** Example of a scan without mechanical vibration. The reason could be a disconnected pressure hose, or an active driver in standby mode.

No planar waves (Figure 7, Figure 8)

1. Adjust the driver position lateral to the center of Xiphoid as shown in Figure 1.
2. Check the localizer images as shown in Figure 3 to ensure the driver position is correct. If not adjust the driver position accordingly.
3. Additional care must be taken in imaging women and obese subjects in placing the driver laterally by moving the breast to have adequate planar waves in the liver.



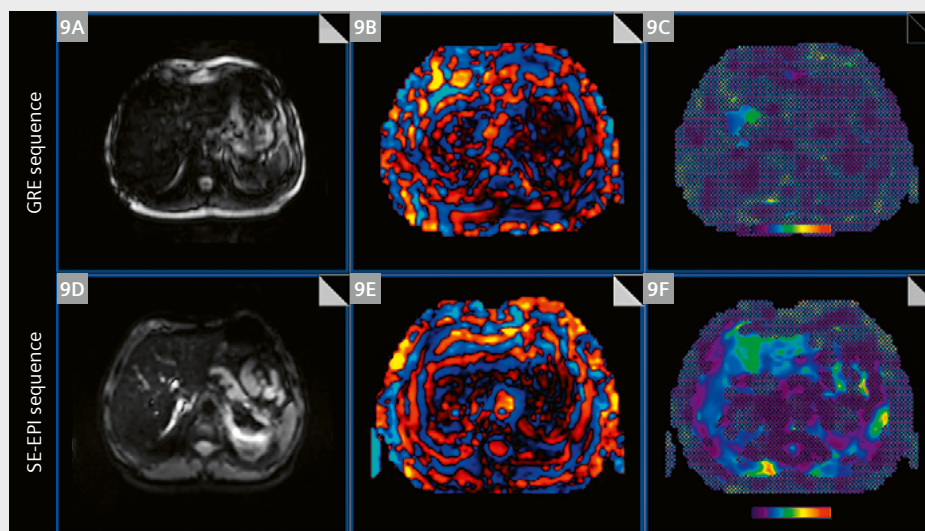
7 Volunteer example at 1.5T with bad placement of the passive driver. **(7A)** Magnitude, **(7B)** wave image with incoherent wave pattern, **(7C)** elastogram with 95% confidence markings.



8 Example of a scan with erroneous driver triggering (Rapid GRE). The reason could be a wrongly set mechanical frequency on the active driver, or a wrongly configured trigger output (optical-to-electrical converter).

Signal loss through transverse relaxation (Figure 9)

The motion encoding gradient between excitation and acquisition in the sequence timing causes echo times to be comparatively long, e.g., ~20 ms for gradient-echo sequences and ~50 ms for SE-EPI sequences. Long echo times in turn make the sequences prone to signal loss if the transverse relaxation times (T_2 or T_2^*) are short, which can be the case at 3T or with hepatic iron overload. Image acquisition parameters should be adjusted for these scenarios. The GRE based MR elastography technique does not perform well on iron overload liver; however, the SE-EPI based technique can be deployed with customized parameter settings [11] to obtain diagnostic quality images.



9 Volunteer example at 3T with $R_2^* \sim 90 \text{ s}^{-1}$, corresponding to a liver iron content of ~1.5 mg/g dry weight. **Top row:** GRE sequence, **bottom row:** SE-EPI sequence. **(9A, D)** magnitude, **(9B, E)** wave image, **(9C, F)** elastogram with 95% confidence markings.



Postprocessing and evaluation

The phase difference images are processed for the standard MRE option using an inline implementation of Resoundant's MMDI inversion algorithm to generate the stiffness maps called elastograms. Stiffness is calculated as the magnitude of the complex shear modulus [18]. The output further contains the original magnitude and phase difference images, and additional computed output: confidence map, stiffness map with confidence markings, and finally colored interpolated wave images. The confidence map is based on the wave quality, i.e., which includes wave signal-to-noise-ratio (SNR) wave amplitude and shape. Then, the stiffness map uses a 95% threshold of the confidence map (shown as unhatched area) to determine the regions to trust within the liver parenchyma and report the stiffness values. Figure 10 shows an example of output series obtained in one healthy volunteer.

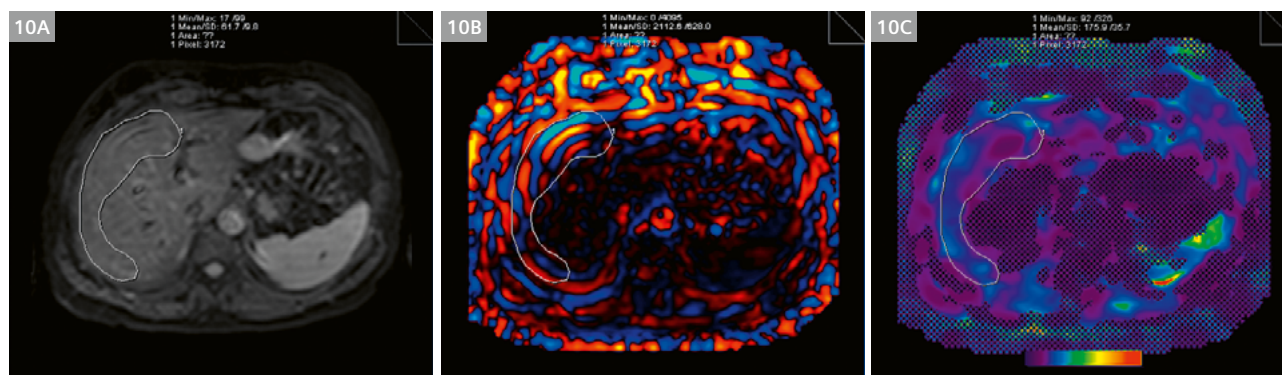
The image quality of the data should be analyzed further to determine if any motion artifacts exist which are typically a result of improper breath-hold. The artifacts appear in the magnitude image as blurring or ghosting in the phase encoding direction. Additionally, the wave images (colored images of the output from the scanner) are also qualitatively analyzed to determine discernible waves propagating in the liver as connected wave fronts as shown in Figure 10.

The stiffness map is generated using a color scale from 0–8 kPa; a grayscale reading of 100 corresponds to 1 kPa. Note that all colorized maps are natively grayscale images displayed using a color lookup table; hence, they

can be windowed, and ROI measurements can be made directly from them¹.

For repeatable measurements, a large region of interest is drawn in the liver parenchyma excluding the hatched region, avoiding the large vessels and at least 1 cm in from the edge of the liver. Note that the cross-hatched regions contain pixels of value zero, so they must not be included in ROI measurements. If in doubt, propagate ROIs to the stiffness map without cross-hatching. Make sure that the wave images show planar wave propagation in the selected region and avoid areas close to the liver edge and the left lobe. Divide ROI mean values by 100 to report the mean stiffness value in kPa. Hot spots in the stiffness maps that occur under the MRE driver or at the liver periphery are typically due to over driving or wave reflections respectively and should be avoided when drawing the ROIs. However, it is acceptable to include small artificial hot spots in the center region of the parenchyma as these may not change the mean stiffness value significantly. In Figure 10, it can be observed that planar waves penetrate throughout the liver and the stiffness map shows sufficient coverage of the liver to report the mean stiffness. Table 2 shows typical stiffness values used to stage liver fibrosis [19]; a meta-analysis [20] reported slightly different values. We advise the user to consult the scientific literature for latest studies which best match their clinical environment.

Stiffness values are generally independent of field strength. However, increased sensitivity to susceptibility effects such as iron overload cause signal loss in the liver parenchyma to be more prevalent at higher field strengths.



10 Scan results (SE-EPI) from a healthy volunteer. (10A) Magnitude, (10B) wave image, (10C) stiffness map with 95% confidence mask overlay; note the color bar indicating the color map distribution across the 0–8 kPa range. Planar wave propagation can be inferred from the uninterrupted wave pattern in the ROI. The manual free-hand ROI contours select regions of high wave quality while observing anatomical placement and the confidence mask.

¹Some PACS systems may not be able to retain these properties. Depending on syngo MR software version, there may be transfer/export settings to manage this.

F0	F1	F2	F3	F4
3.00 ± 1.12 kPa	3.11 ± 0.82 kPa	3.87 ± 1.85 kPa	4.78 ± 1.89 kPa	6.52 ± 2.34 kPa

Table 2: Mean ± standard deviation values of MRE-derived liver stiffness for different fibrosis stages from 289 patients according to [19].

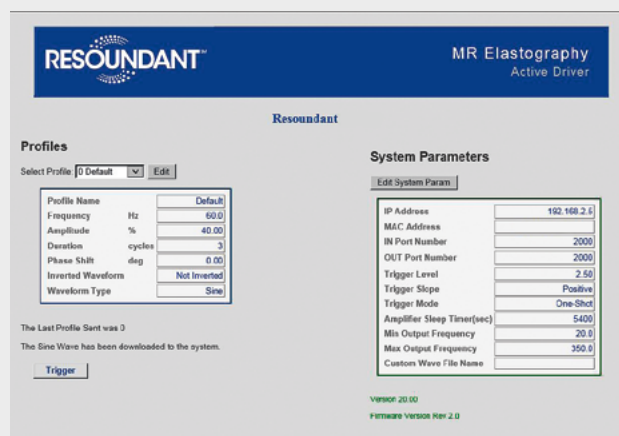
Insert 3: Setup and configuration

The hardware part of the MRE option is set up by a service engineer. Settings of the active driver can typically be configured once and remain unchanged thereafter. Details can be found in the operator manual [16]; some of them are given here for reference.

Figure 11 is a screenshot of the active driver's configuration page which can be accessed via a web browser and Ethernet connection, which may be a special research configuration². The number of cycles per trigger is set to 3 for both GRE and SE-EPI MRE sequences as they are each designed to trigger the active driver every 50 ms. In pediatric patients³ or in the 15% of adult patients with very large or very small body habitus, it can be beneficial to change the driver amplitude.

Note: If you have an older driver with earlier firmware (< version 2.0 as shown in the lower right-hand corner of the configuration screen), the driver frequency will need to be set to 60.1 Hz in order to sync correctly with the incoming triggers from the sequence. Additionally, the driver has a sleep timer configured in the lower part of the right-hand column on the configuration page. After the preset amount of time, the amplifier will go to sleep and no longer respond to triggers.

To wake up the unit either depress the Trigger button on the configuration page or manually cycle the power on the unit. Without this sleep timer, damage to the driver can occur, greatly limiting its lifespan.



11 Screenshot showing the MRE active driver setting card (Resoundant Inc, Rochester, MN, USA) containing all necessary parameters for either MRE sequence at the proper frequency and amplitude.

²Please work with your MR Collaborations scientist and your service engineer if this special configuration is necessary at your site.

³MR scanning has not been established as safe for imaging fetuses and infants less than two years of age. The responsible physician must evaluate the benefits of the MR examination compared to those of other imaging procedures.

Summary and take away points

It was the intent of this article to give Siemens Healthineers MRE users, both new and experienced, guidance on how to consistently perform MRE with high-quality results. The content is weighted heavily on achieving a good patient setup with proper passive driver positioning. We have found that driver positioning can be highly variable in practice and is a major contributor to non-diagnostic MRE exams. Using the described workflow,

however, it was shown that achieving measurable areas from 65% to 85% of liver coverage, our definition of a successful exam, is possible. Further, reproducibility of the results not only depends on patient setup and scanning workflow, but also on standardized image interpretation, quality checks, and ROI measurements. Therefore, the guidance provided includes these topics as well.

Once the MRE option is set up and configured correctly (see Insert 3), and the workflow for scanning, reading, and reporting is established, the procedure should be kept



unchanged to achieve low variability between examinations. In Insert 1 we summarize a best-practice workflow that includes some elements that may not be commonly considered. With its additional hardware and patient setup, the MRE acquisition has some inherent complexities not present in other MR imaging applications. Optimal wave propagation can depend on multiple factors ranging from hardware functionality to setup to exiting patient pathology. To address some of the more common scenarios we have provided a troubleshooting guide as Insert 2.

Finally, it should be noted that the current standard MRE solution is tailored to breath-hold liver applications by only acquiring a low number of slices and only encoding a single (through-slice) motion direction. This implicitly makes simplifying assumptions of in-plane, planar wave propagation without reflections. This also makes localized stiffness readings, e.g., by liver segment, less reliable. Thus, this “2D” standard solution cannot easily be transferred to other organs in the abdomen, or to other body regions. There exist prototypes with contiguous coverage of larger regions and “3D” motion encoding in all three spatial directions [12], as well as dedicated applications in other body regions [13].

References

- 1 Michalopoulos GK, DeFrances MC. Liver regeneration. *Science*. 1997;276(5309):60-6.
- 2 Bataller R, Brenner DA. Liver fibrosis. *J Clin Invest*. 2005;115(2):209-18. Erratum in: *J Clin Invest*. 2005;115(4):1100.
- 3 Sharma S, Khalili K, Nguyen GC. Non-invasive diagnosis of advanced fibrosis and cirrhosis. *World J Gastroenterol*. 2014;20(45):16820-30.
- 4 Wang XP, Wang Y, Ma H, Wang H, Yang DW, et al. Assessment of liver fibrosis with liver and spleen magnetic resonance elastography, serum markers in chronic liver disease. *Quant Imaging Med Surg*. 2020;10(6):1208-1222.
- 5 Tana MM, Muir AJ. Diagnosing Liver Fibrosis and Cirrhosis: Serum, Imaging, or Tissue? *Clin Gastroenterol Hepatol*. 2018;16(1):16-18.
- 6 Trout AT, Serai S, Mahley AD, Wang H, Zhang Y, Zhang B, Dillman JR. Liver Stiffness Measurements with MR Elastography: Agreement and Repeatability across Imaging Systems, Field Strengths, and Pulse Sequences. *Radiology*. 2016;281(3):793-804.
- 7 Venkatesh SK, Wang G, Lim SG, Wee A. Magnetic resonance elastography for the detection and staging of liver fibrosis in chronic hepatitis B. *Eur Radiol*. 2014;24(1):70-8.
- 8 Hallinan JT, Alsaf HS, Wee A, Venkatesh SK. Magnetic resonance elastography of liver: influence of intravenous gadolinium administration on measured liver stiffness. *Abdom Imaging*. 2015;40(4):783-8.
- 9 Bolster Jr B, Jin N, Kannengiesser S. MR Elastography – Pearls and Pitfalls. *MAGNETOM Flash* (71) 2/2018:19-23.
- 10 QIBA Profile, Magnetic resonance elastography of the liver. Stage 2: consensus profile. Radiological Society of North America https://qibawiki.rsna.org/images/a/a5/MRE-QIBAProfile-2018-05-02_CONSENSUS.pdf (2018).
- 11 Barrera CA, Otero HJ, Hartung HD, Biko DM, Serai SD. Protocol optimization for cardiac and liver iron content assessment using MRI: What sequence should I use?, *Clin Imaging*, Volume 56, 2019, Pages 52-57. 2019;56:52-57.
- 12 Shi Y, Glaser KJ, Venkatesh SK, Ben-Abraham EI, Ehman RL. Feasibility of using 3D MR elastography to determine pancreatic stiffness in healthy volunteers. *J Magn Reson Imaging*. 2015;41(2):369-75.
- 13 Dong H, White RD, Kolipaka A. Advances and Future Direction of Magnetic Resonance Elastography. *Top Magn Reson Imaging*. 2018;27(5):363-384.
- 14 Chamarthi SK, Raterman B, Mazumder R, Michaels A, Oza VM, Hanje J, Bolster B, Jin N, White RD, Kolipaka A. Rapid acquisition technique for MR elastography of the liver. *Magn Reson Imaging*. 2014;32(6):679-83.
- 15 Rump J, Klatt D, Braun J, Warmuth C, Sack I. Fractional encoding of harmonic motions in MR elastography. *Magn Reson Med*. 2007;57(2):388-95.
- 16 Siemens Healthineers MR. Operator manual MR Elastography.
- 17 Resoundant Inc. Technical report. Available from <https://www.resoundant.com/technical-report>. [Accessed Feb 23, 2022].
- 18 Manduca A, Bayly PJ, Ehman RL, Kolipaka A, Royston TJ, Sack I, Sinkus R, Van Beers BE. MR elastography: Principles, guidelines, and terminology. *Magn Reson Med*. 2021;85(5):2377-2390.
- 19 Yin M, Glaser KJ, Talwalkar JA, Chen J, Manduca A, Ehman RL. Hepatic MR Elastography: Clinical Performance in a Series of 1377 Consecutive Examinations. *Radiology*. 2016;278(1):114-24.
- 20 Singh S, Venkatesh SK, Wang Z, Miller FH, Ehman RL, et al. Diagnostic performance of magnetic resonance elastography in staging liver fibrosis: a systematic review and meta-analysis of individual participant data. *Clin Gastroenterol Hepatol*. 2015;13(3):440-451.



Contact

Arunark Kolipaka, Ph.D., FAHA, FSCMR
Associate Professor & Technical Director,
Magnetic Resonance Imaging
The Ohio State University
Wexner Medical Center
Department of Radiology
395 West 12th Ave, 4th Floor
Columbus, OH 43210
USA
Phone: +1 614-366-0268
arunark.kolipaka@osumc.edu



Liver Magnetic Resonance Elastography in Children

Jędrzej Sarnecki¹, Piotr Pawliszak¹, Paulina Opyrchal¹, Cepuch Kamil², Elżbieta Jurkiewicz¹

¹Department of Diagnostic Imaging, The Children's Memorial Health Institute, Warszawa, Poland

²Siemens Healthineers, Warszawa, Poland

Magnetic resonance elastography (MRE) was introduced in the mid-90s by researchers at Mayo Clinic in Rochester, MN, USA. It is a dynamic imaging technique that assesses the elasticity of tissues [1]. The basic principle of this diagnostic technique relies on the evaluation of the mechanical properties, often referred to as stiffness or elasticity, of tissues. This is possible by measuring the tissue's distortion in response to a mechanical stimulus in the form of vibrations [2]. Some authors refer to MRE as "virtual palpation", as this approach to tissue evaluation somewhat resembles palpation. Similar to the observations made during a physical examination, normal and abnormal tissues differ in elasticity, mostly due to fibrosis and to cellular proliferation and infiltration in pathologically altered regions.

In order to assess a tissue's stiffness using MRE, an external force needs to be applied to the evaluated organ. The force is provided by an external device referred to as a "driver", which generates vibrations at a single, specified frequency within the lower part of the audio frequency range [2]. The motion induced by the mechanical stress is then imaged using a standard phase-contrast imaging sequence with motion-encoding gradients (MEG) synchronized with the driver's function. The imaging time itself is short and does not significantly extend the duration of a standard abdominal MRI study. Typically, MRE of the liver consists of four cross-sectional scans of the liver, each obtained in less than one minute on a MAGNETOM Avanto^{fit} scanner (Siemens Healthcare, Erlangen, Germany). The study is normally well tolerated, and patients describe the sensations caused by the vibrations as "tingling". The data acquired in the process of wave propagation are used to generate elastograms (Fig. 1D and 2D). Image analysis using selected regions of interest

(ROIs) enables measurement of the target tissue's stiffness, typically expressed in kilopascals (kPa). Aside from typical MRI contraindications, there are no absolute contraindications for MRE. However, study postponement should be considered for patients directly after liver biopsy or with skin lesions at the typical driver location.

Over the years, many potential fields of MRE application have emerged. However, it is currently most widely used in liver assessment for both adults and children. As the prevalence of chronic liver disease increases – mainly due to the rising number of patients with nonalcoholic fatty liver disease (NAFLD) – there is a need for noninvasive methods of assessing the liver parenchyma. Hepatic fibrosis is a dynamic and potentially (in the early stages) reversible condition that precedes cirrhosis. Currently, core liver biopsy is regarded as the gold standard in liver disease diagnosis and hepatic disease staging. Nevertheless, it has several disadvantages: It is invasive, costly, and only assesses a minute sample of the liver [3]. There is also a non-negligible risk of obtaining nondiagnostic material, for example due to fragmentation or lack of liver tissue [4, 5]. Low sampling volume may affect the sensitivity of diagnosing liver disease that is heterogeneously distributed across the parenchyma.

Therefore, there is increasing interest in using MRI or ultrasound elastographic techniques to assess and monitor liver fibrosis. In contrast to liver biopsy, MRE is a noninvasive diagnostic procedure that enables a much larger sampling volume of liver parenchyma. Its other advantages are the short scanning time, relatively low cost, and high interobserver and intraobserver agreement [6]. It is currently the most accurate noninvasive method of detecting and grading liver fibrosis [7, 8]. In some cases, simultane-



ous calculation of spleen elasticity can provide additional value, especially in patients with portal hypertension and esophageal varices.

To date, numerous studies have proven MRE to be a feasible tool for evaluating liver fibrosis. Some authors even suggest that, owing to its high negative predictive value for advanced fibrosis, MRE could replace core liver biopsy for surveilling patients who have undergone the invasive diagnostic procedure in the past [9, 10]. Noninvasive assessment of the liver may also be useful in patients with chronic diseases that predispose them to liver fibrosis, such as cystic fibrosis, multicystic kidney disease, biliary atresia, inflammatory bowel disease, and alpha-1 antitrypsin deficiency. In patients after liver transplantation, MRE could possibly substitute some protocolary liver biopsies, which are performed every 5 to 10 years, or identify patients who would benefit from a biopsy. In combination with the LiverLab tool (Siemens Healthcare, Erlangen, Germany), MRE could also be used for noninvasive liver assessment in living donors to prevent or anticipate possible complications of the procedure.

Moreover, MRE can detect increased liver stiffness even in the absence of histologically detectable fibrosis. The results possibly reflect the increased volume of extracellular fluid in the early stages of liver disease preceding fibrosis [11]. This can occur in steatohepatitis – the mechanical properties of extracellular fluid lead to perisinusoidal cell activation (Ito cells) with consecutive development of fibrosis due to dedifferentiation of these cells to myofibroblasts [12]. Nevertheless, simple steatosis does not alter the mechanical properties of the liver, so it is undetectable using elastography. Given current growing trends in the epidemiology of NAFLD and nonalcoholic steatohepatitis (NASH), grading steatosis in all patients with liver disease should be considered. Parametric imaging of the liver and assessing it using the LiverLab tool, which evaluates liver steatosis and liver iron load, can easily be incorporated into the abdominal MRI study.

Proper positioning of the driver allows us to simultaneously evaluate both liver and spleen [13]. This is particularly useful in liver disease that leads to portal hypertension and increased hepatic venous pressure gradient (HVPG), which correlates with the risk of esophageal varices development, ascites, and splenomegaly. Currently, HVPG can only be evaluated invasively [14, 15]. However, there is data suggesting that MRE is a feasible tool for estimating this parameter and has prognostic value. Liver and spleen elasticity increases with the degree of esophageal varices on endoscopy. Additionally, spleen stiffness measured using MRE in children was shown to have good diagnostic performance in predicting the presence of gastroesophageal varices [16].

MRE in pediatric liver disease

Pediatric patients can suffer from a variety of chronic liver diseases, both of hereditary and sporadic origin. Some conditions may lead to liver fibrosis and, when untreated, to cirrhosis.

NAFLD is currently the most common chronic liver disease in children and its prevalence is rising. The condition constitutes a significant public health issue, as its sequelae include cirrhosis and hepatocellular carcinoma. In the United States, NAFLD is currently the second most common cause of liver transplantation in adults [17]. Between 40% and 90% of patients with NAFLD develop liver fibrosis, so MRE and LiverLab assessment might be increasingly employed in pediatric patients [18]. In a prospective multicenter observational study (MRI Assessment Guiding NAFLD Evaluation and Treatment, MAGNET) Schwimmer et al. compared hepatic stiffness assessed in MRE and histologic fibrosis staging in children aged 8–17 with known or suspected NAFLD [18]. The study showed good correlation between the histologically established degree of liver fibrosis and MRE liver stiffness measurements in the 90 patients with reliable imaging data. Importantly, the inter-reader agreement of liver stiffness evaluation was strong. The study also showed potential problems with conducting MRE in children, as the percentage of unreliable imaging studies was relatively high, at 16% [18]. However, a large retrospective analysis of 468 MRE studies in children and young adults demonstrated successful MRE data acquisition in the vast majority (96%) of attempts [19].

In a study which included 35 children with chronic liver disease – of whom 27 had NAFLD, and of those 22 had NASH – Xanthakos et al. showed very good accuracy of MRE in diagnosing significant liver fibrosis (stage ≥ 2), with a sensitivity of 88%, a specificity of 85%, and an AUC of 0.92 [20]. Another study analyzed 86 children and adults under 21 years of age with clinical indications for liver biopsy (most commonly fatty liver disease, followed by autoimmune hepatitis and primary sclerosing cholangitis) who also underwent MRE [21]. The analysis of the collected data showed a good correlation between hepatic stiffness and severity of liver fibrosis. Additionally, the study demonstrated moderate predictive performance of MRE for identification of Ludwig stage ≥ 2 fibrosis (AUC = 0.70). However, the accuracy was significantly higher for diagnosis of stage 3 or higher fibrosis (AUC = 0.92) [21].

MRE was also compared with other quantitative MRI markers and clinical variables in a study of 58 children and young adults with autoimmune hepatitis (AIH), primary sclerosing cholangitis (PSC), or autoimmune sclerosing

cholangitis (ASC) [22]. Mahalingam et al. demonstrated significant associations between liver stiffness measured in MRE and magnetic resonance cholangiopancreatography (MRCP) metrics, T1 relaxation times, and the levels of laboratory markers of liver disease [22]. Additionally, McCary et al. showed that the above quantitative parameters, including hepatic stiffness, are independently associated with worse Mayo risk scores and SCOPE index in children and young adults with autoimmune liver disease [23]. MRE can also be used to assess liver parenchyma in children after a Fontan operation, as liver injury is a well-known complication of the procedure [24].

The results of the studies show potential for diagnosing and monitoring liver fibrosis in pediatric patients with NAFLD and other chronic liver diseases. A number of authors also believe that some typically pediatric conditions may become clinically significant indications for MRE. It is debated whether MRE can help differentiate biliary atresia from neonatal¹ hepatitis or provide early diagnoses of liver disease in patients on total parenteral nutrition or with short bowel syndrome [3]. Nevertheless, more studies are needed to expand the clinical indications for liver MRE in pediatric patients.

Importantly, Trout et al. recently published normative liver stiffness values measured with MRE in a prospective, multicenter study with 71 participants who were aged 7 to 17 and had no personal or family history of liver disease [25]. The mean liver stiffness in the study group was 2.1 kPa, with the 95th percentile equal to 2.8 kPa [25]. Crucially, the investigators did not observe significant differences in liver stiffness measured on different MRI scanners, which suggests that the established normative data can be uniformly applied across different MRI platforms [25]. The study also did not show significant differences between MRE imaging on 1.5T and 3T scanners. In our experience a similar cutoff value of 2.86 kPa, which is significantly lower than in adults, is associated with very good diagnostic accuracy of biopsy-confirmed significant liver fibrosis corresponding to an Ishak score of ≥ 3 in patients with AIH and Wilson's disease (Pawliszak et al., unpublished data).

How we do it

Patient preparation for liver MRE does not differ significantly from preparation for a standard abdominal MRI, except for the recommended fasting period of 4 to 6 hours [2, 25]. This is due to the fact that, in patients with chronic liver disease and liver fibrosis, liver stiffness may increase following a meal. Therefore, fasting is advised to increase measurement reproducibility [2].

As previously described, liver MRE requires reproducible vibrations with a predefined frequency. This is achieved by using a driver, which should be placed over the right liver lobe. The standard driver position is usually in the right midclavicular line, at the level of the xiphoid process of the sternum. In some cases, such as in patients post right hemihepatectomy or post liver transplant, the driver placement might need to be modified and should cover the approximate location of the largest portion of the liver [2]. The driver position can be adjusted after the localizer sequence.

For standard liver MRE, the driver's frequency should be set to 60 Hz. Performing test stimuli from the driver prior to proper acquisition can increase the patient's compliance.

Liver MRE is usually part of an abdominal MR examination, or it is performed together with MRCP. Breath-holding is useful, but not vital for successful image acquisition during liver MRE. If the patient is cooperating, image acquisition should preferably be performed at end-expiration.

Imaging starts with two T2-weighted HASTE sequences in transverse and coronal planes for precise liver localization. The standard imaging protocol consists of imaging at four levels of the liver, including an acquisition at the level of the liver hilum. A GRE MRE sequence is acquired with a voxel size of $1.4 \times 1.4 \times 5.0$ mm, with one slice positioned transversally in the scanner coordinate system and with TR/TE = 50/23.75 ms. The acquisition lasts 19 seconds, which corresponds to one breath-hold. Each elastography is followed by a low-resolution T1-weighted FLASH sequence for position confirmation and spatial localization. After the elastography, patients undergo examination for their specific clinical questions.

The causes of poor or nondiagnostic elastographic imaging include poor shear-wave delivery to the liver, improper driver power, other technical issues with the driver, paramagnetic or motion artifacts, or liver iron overload. Each of the acquired scans undergoes automatic quantitative analysis, and all areas with a confidence threshold below 95% are marked as unsuitable for evaluation.

Liver stiffness is measured by placing an ROI in the liver parenchyma with good imaging quality. The ROI should not include the subcapsular portions of the liver (approx. 1 cm thick), the hilum, the great vessels, the gall bladder (if applicable), or any apparent artifacts. Mean liver stiffness values calculated for each area should be added and divided by the number of scans (usually four) [26]. In cases of a smaller liver, due to area differences, mean liver stiffness can be adjusted for this parameter.

¹MR scanning has not been established as safe for imaging fetuses and infants less than two years of age. The responsible physician must evaluate the benefits of the MR examination compared to those of other imaging procedures.



Case 1

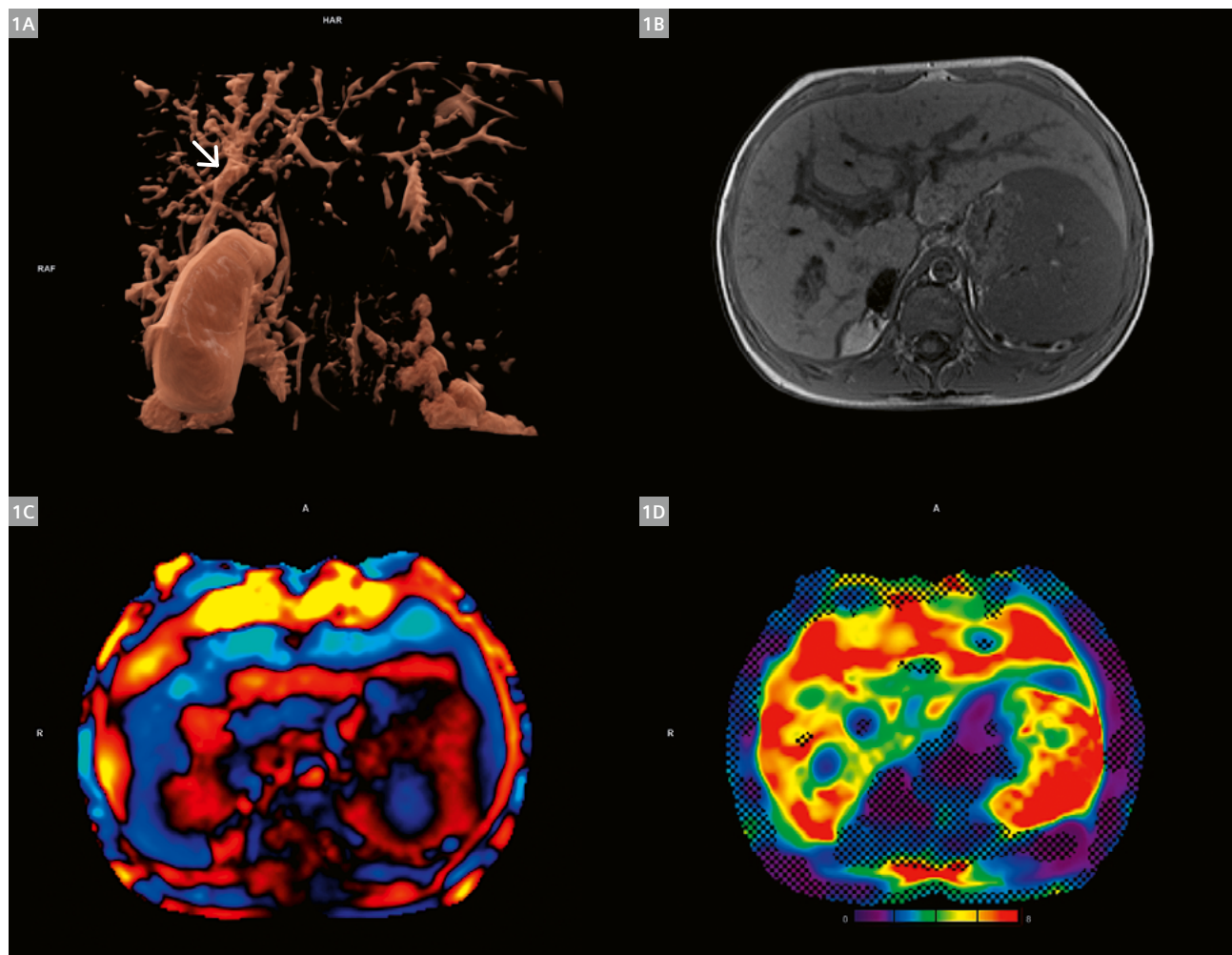
A 17-year-old boy with ulcerative colitis, AIH, and PSC diagnosed five years prior was referred for a check-up by MRCP. At the time of the imaging study, the patient had no clinical signs or symptoms. However, laboratory tests revealed elevated transaminases, GGTP, bilirubin, bile acids, and IgG4, and thrombocytopenia.

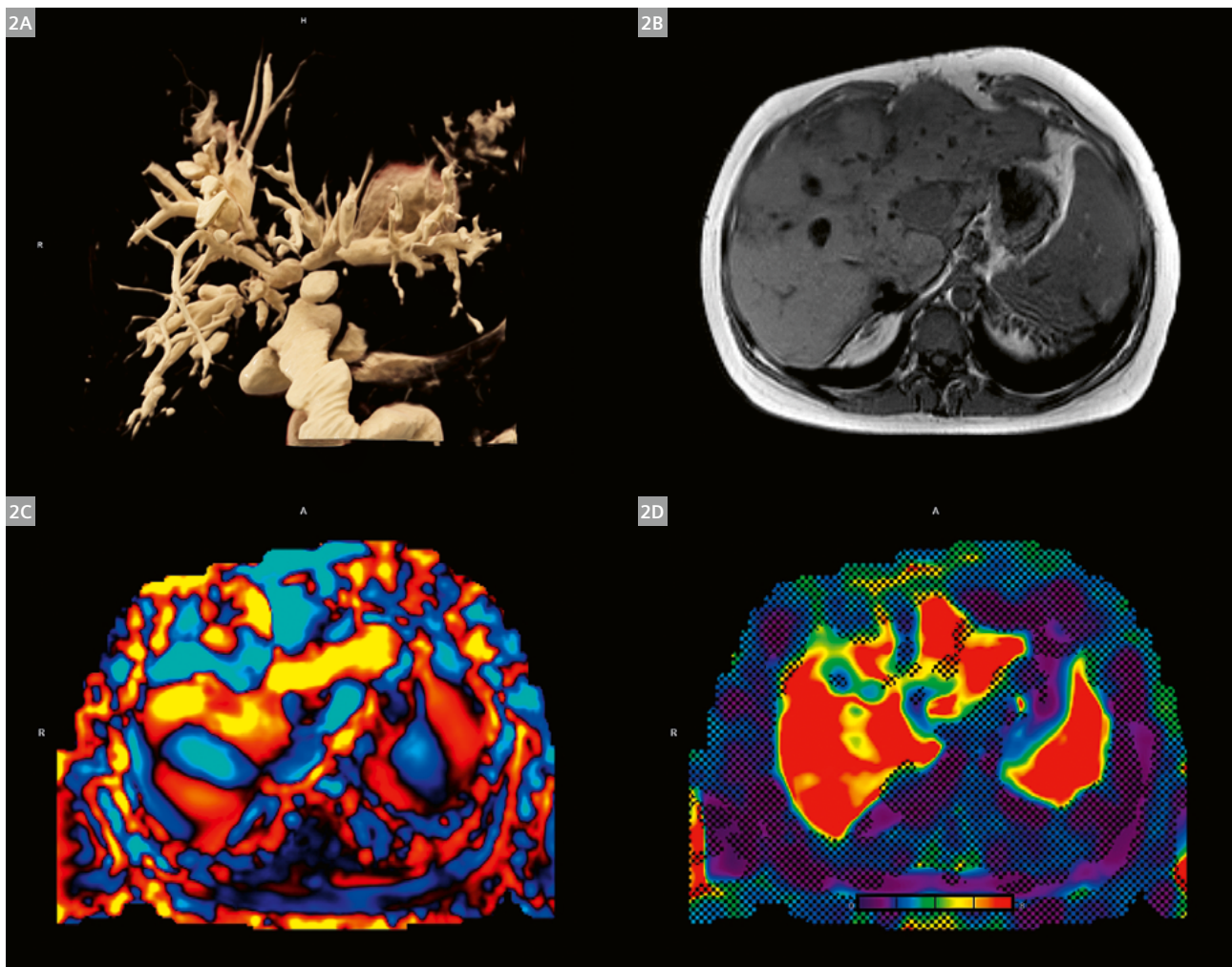
Figure 1A shows a volume-rendered reconstruction of the biliary ducts. Peripheral biliary ducts were significantly dilated, with a diameter of up to 6 mm, and had irregular contours. MRE revealed significantly increased liver stiffness, with a mean value of 5.5 kPa. The spleen was significantly enlarged at 27 cm and had stiffness of 7.0 kPa. Figures 1B, 1C, and 1D show magnitude, wave, and color elastogram with 95% confidence masks. Biopsy performed the day after MRI confirmed significant liver fibrosis, corresponding to an Ishak score of 6. Gastroscopy performed during the same hospitalization period revealed esophageal varices, which were endoscopically ligated.

Case 2

A 14-year-old girl with biliary atresia, five years after liver transplantation (LTx), was admitted due to fever and elevated inflammatory markers. She received antibiotic therapy, which relieved her clinical signs and normalized her laboratory markers. Afterwards, she was referred for MRCP to assess the biliary ducts. In addition, MRE was performed to assess the stiffness of the transplanted liver.

The study revealed a heterogeneous, polycystic liver. In segment III of the liver, a fluid collection measuring $3.5 \times 3 \times 3.5$ cm was observed, without diffusion restriction. Bile ducts were significantly and irregularly dilated by up to 10 mm. The stiffness of the transplanted liver was markedly elevated, with a global mean value of 7.5 kPa. Spleen stiffness was 7.8 kPa. Figures 2A–D show magnitude, wave, and color elastogram with 95% confidence masks and a volume rendering of the liver bile ducts.





During the same hospitalization period, the patient underwent liver biopsy, which confirmed significant liver fibrosis with an Ishak score of 6. Grade I esophageal varices and a single gastric varix were diagnosed. The patient was discharged in a good state with cyclic antibiotic therapy.

References

- Muthupillai R, Lomas DJ, Rossman PJ, Greenleaf JF, Manduca A, Ehman RL. Magnetic resonance elastography by direct visualization of propagating acoustic strain waves. *Science*. 1995;269(5232):1854–7.
- Guglielmo FF, Venkatesh SK, Mitchell DG. Liver MR Elastography Technique and Image Interpretation: Pearls and Pitfalls. *RadioGraphics*. 2019;39(7):1983–2002.
- Binkovitz LA, El-Youssef M, Glaser KJ, Yin M, Binkovitz AK, Ehman RL. Pediatric MR elastography of hepatic fibrosis: principles, technique and early clinical experience. *Pediatr Radiol*. 2012;42(4):402–9.
- Talwalkar JA. Elastography for detecting hepatic fibrosis: options and considerations. *Gastroenterology*. 2008;135(1):299–302.
- Mehta SH, Lau B, Afdhal NH, Thomas DL. Exceeding the limits of liver histology markers. *J Hepatol*. 2009;50(1):36–41.
- Shire NJ, Yin M, Chen J, Railkar RA, Fox-Bosetti S, Johnson SM, et al. Test-retest repeatability of MR elastography for noninvasive liver fibrosis assessment in hepatitis C. *J Magn Reson Imaging*. 2011;34(4):947–55.
- Venkatesh SK, Yin M, Takahashi N, Glockner JF, Talwalkar JA, Ehman RL. Non-invasive detection of liver fibrosis: MR imaging features vs. MR elastography. *Abdom Imaging*. 2015;40(4):766–75.
- Singh S, Venkatesh SK, Wang Z, Miller FH, Motosugi U, Low RN, et al. Diagnostic performance of magnetic resonance elastography in staging liver fibrosis: a systematic review and meta-analysis of individual participant data. *Clin Gastroenterol Hepatol*. 2015;13(3):440–451.e6.
- Venkatesh SK, Yin M, Ehman RL. Magnetic resonance elastography of liver: technique, analysis, and clinical applications. *J Magn Reson Imaging*. 2013;37(3):544–55.
- Park HS, Kim YJ, Yu MH, Choe WH, Jung SI, Jeon HJ. Three-Tesla magnetic resonance elastography for hepatic fibrosis: comparison with diffusion-weighted imaging and gadoteric acid-enhanced magnetic resonance imaging. *World J Gastroenterol*. 2014;20(46):17558–67.
- Simonetto DA, Yang H, Yin M, de Assuncao TM, Kwon JH, Hilscher M, et al. Chronic passive venous congestion drives hepatic fibrogenesis via sinusoidal thrombosis and mechanical forces. *Hepatology*. 2015;61(2):648–59.



- 12 Chen J, Talwalkar JA, Yin M, Glaser KJ, Sanderson SO, Ehman RL. Early detection of nonalcoholic steatohepatitis in patients with nonalcoholic fatty liver disease by using MR elastography. *Radiology*. 2011;259(3):749–56.
- 13 Dyvorne HA, Jajamovich GH, Besa C, Cooper N, Taouli B. Simultaneous measurement of hepatic and splenic stiffness using MR elastography: preliminary experience. *Abdom Imaging*. 2015;40(4):803–9.
- 14 Escorsell A, Garcia-Pagán JC, Bosch J. Assessment of portal hypertension in humans. *Clin Liver Dis*. 2001;5(3):575–89.
- 15 Ripoll C, Groszmann R, Garcia-Tsao G, Grace N, Burroughs A, Planas R, et al. Hepatic venous pressure gradient predicts clinical decompensation in patients with compensated cirrhosis. *Gastroenterology*. 2007;133(2):481–8.
- 16 Yoon H, Shin HJ, Kim M-J, Han SJ, Koh H, Kim S, et al. Predicting gastroesophageal varices through spleen magnetic resonance elastography in pediatric liver fibrosis. *World J Gastroenterol*. 2019;25(3):367–377.
- 17 Wong RJ, Aguilar M, Cheung R, Perumpail RB, Harrison SA, Younossi ZM, et al. Nonalcoholic steatohepatitis is the second leading etiology of liver disease among adults awaiting liver transplantation in the United States. *Gastroenterology*. 2015;148(3):547–55.
- 18 Schwimmer JB, Behling C, Angeles JE, Paiz M, Durelle J, Africa J, et al. Magnetic resonance elastography measured shear stiffness as a biomarker of fibrosis in pediatric nonalcoholic fatty liver disease. *Hepatology*. 2017;66(5):1474–1485.
- 19 Joshi M, Dillman JR, Towbin AJ, Serai SD, Trout AT. MR elastography: high rate of technical success in pediatric and young adult patients. *Pediatr Radiol*. 2017;47(7):838–843.
- 20 Xanthakos SA, Podberesky DJ, Serai SD, Miles L, King EC, Balistreri WF, et al. Use of magnetic resonance elastography to assess hepatic fibrosis in children with chronic liver disease. *J Pediatr*. 2014;164(1):186–8.
- 21 Trout AT, Sheridan RM, Serai SD, Xanthakos SA, Su W, Zhang B, et al. Diagnostic Performance of MR Elastography for Liver Fibrosis in Children and Young Adults with a Spectrum of Liver Diseases. *Radiology*. 2018;287(3):824–832.
- 22 Mahalingam N, Trout AT, Gandhi DB, Sahay RD, Singh R, Miethke AG, et al. Associations between MRI T1 mapping, liver stiffness, quantitative MRCP, and laboratory biomarkers in children and young adults with autoimmune liver disease. *Abdom Radiol (NY)*. 2022;47(2):672–683.
- 23 McCrary J, Trout AT, Mahalingam N, Singh R, Rojas CC, Miethke AG, et al. Associations Between Quantitative MRI Metrics and Clinical Risk Scores in Children and Young Adults With Autoimmune Liver Disease. *AJR Am J Roentgenol*. 2022;1–9.
- 24 DiPaola FW, Schumacher KR, Goldberg CS, et al. Effect of Fontan operation on liver stiffness in children with single ventricle physiology. *Eur Radiol*. 2017;27(6):2434–2442.
- 25 Trout AT, Anupindi SA, Gee MS, Khanna G, Xanthakos SA, Serai SD, et al. Normal Liver Stiffness Measured with MR Elastography in Children. *Radiology*. 2020;297(3):663–669.
- 26 QIBA Profile, Magnetic resonance elastography of the liver. Stage 2: consensus profile. Radiological Society of North America https://qibawiki.rsna.org/images/a/a5/MRE-QIBAProfile-2018-05-02_CONSENSUS.pdf (2018).

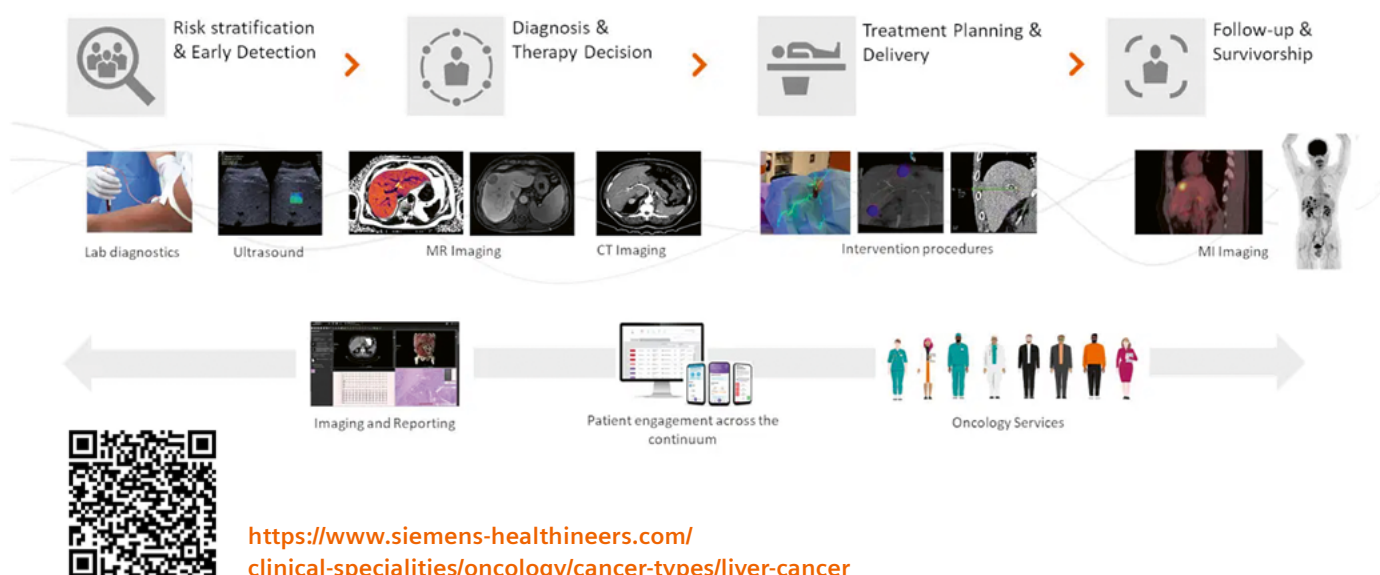
Contact

Professor Elżbieta Jurkiewicz, M.D., Ph.D.
Department of Diagnostic Imaging
The Children's Memorial Health Institute
aleja Dzieci Polskich 20
04-736 Warszawa
Poland
e.jurkiewicz@ipczd.pl

Advertisement

We are with you every step of the way.

Explore our comprehensive offering for liver cancer management.





Fast and Reliable Liver Imaging Using Deep Learning HASTE

Sébastien Mulé, M.D., Ph.D.^{1,2,3}; Aurélien Massire, Ph.D.⁴; Pierre Zerbib¹; Dominik Nickel, Ph.D.⁵; Alain Luciani, Ph.D., M.D.^{1,2,3}

¹Service d'Imagerie Médicale, AP-HP, Hôpitaux Universitaires Henri Mondor, Créteil, France

²Faculté de Santé, Université Paris-Est Créteil, Créteil, France

³INSERM IMRB, U 955, Equipe 18, Créteil, France

⁴Siemens Healthcare SAS, Saint-Denis, France

⁵Siemens Healthineers, Erlangen, Germany

Introduction

With its superb ability to detect, characterize, and differentiate focal lesions in the liver, magnetic resonance imaging (MRI) has become the gold standard and problem-solving modality in diagnostic abdominal imaging. Despite its indisputable clinical value, however, MRI is not as robust and reliable as other modalities, e.g., CT scans. This is mainly due to breathing-induced motion during the time-consuming data sampling process and the long scan time of 25–30 minutes.

Triggered and breath-hold acquisitions

Different strategies to minimize the susceptibility to artifacts have been developed over the last decades. The most routinely used ones are: (multiple-)breath-hold acquisitions; prospectively and retrospectively triggered acquisitions where only data in specific states of the respiratory cycle is acquired or used for reconstruction; and data sampling trajectories which are inherently less susceptible to motion, such as radial or BLADE sampling. Each approach has certain advantages and disadvantages: With triggered acquisitions, the data sampling rate over time is low and scan times can easily exceed five minutes per acquisition, particularly in patients with irregular or shallow breathing patterns. On the other hand, triggered acquisitions do not require major compromises in spatial resolution, as data sampling does not have to be “squeezed” into a single or a few breath-holds. Non-Cartesian sampling schemes such as radial trajectories are very robust because they simply average out motion effects, but they may show image blurring and streaking artifacts.

The advent and clinical adoption of MR acceleration techniques that use “intelligent” *k*-space subsampling and parallel data sampling – such as SENSE, GRAPPA, CAIPIRINHA, SMS, and Compressed Sensing – have drastically reduced breath-hold durations and data sampling times for most of the relevant imaging contrasts in abdominal MRI. However, they are only applicable to certain contrast weightings and sequence types.

One of the remaining weak points of a typical, routine liver MRI protocol (with T2-weighted imaging, diffusion-weighted imaging, T1-weighted in- and opposed-phase imaging, dynamic contrast-enhanced T1-weighted scanning, and post-contrast T1-weighted scans) is the acquisition of high-resolution, high-quality T2-weighted TSE images in a short scan time. To achieve appropriate T2-weighting, long TRs have to be chosen, which require several breath-holds or long respiratory-triggered protocols to cover multiple segments of the *k*-space and thereby achieve sufficient *k*-space sampling to reconstruct high-resolution images. Modified segmented Cartesian sampling schemes in which several rotated, overlapping bundles of parallel *k*-space lines are acquired and combined are available from all vendors (PROPELLER, MultiVane, BLADE) and have been shown to improve robustness and SNR compared to conventional TSE scanning. Scan times, however, remain a challenge for both triggered and multiple-breath-hold acquisitions.

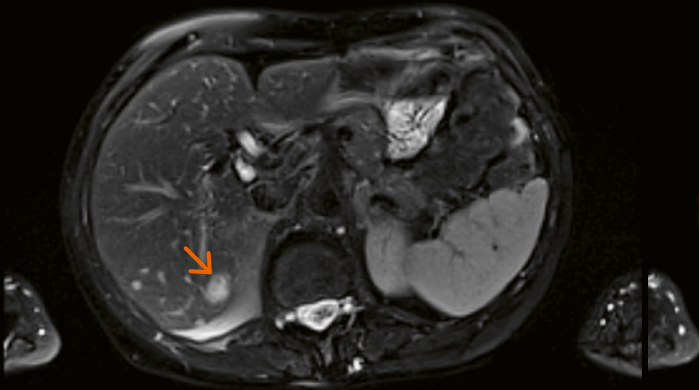
Single-shot acquisition

A more radical approach is to acquire data for a complete imaging slice in a single shot, as implemented in the half-Fourier acquisition single-shot turbo spin-echo (HASTE) sequence. Since data acquisition requires just fractions of a second, motion artifacts do not pose any problem. Breath-holds or synchronization with breathing are only required to achieve uniform slice coverage across the abdomen. On the downside, reading out the entire *k*-space in a single shot requires a compromise in spatial resolution as the echo train length (which scales with spatial resolution) makes HASTE prone to T2-decay-related blurring and SNR reduction. Accordingly, HASTE images are not typically considered adequate for high-resolution T2-weighted imaging of the abdomen. They are mostly used to provide a quick overview or to acquire “something” in challenging cases, e.g., pediatric patients¹.

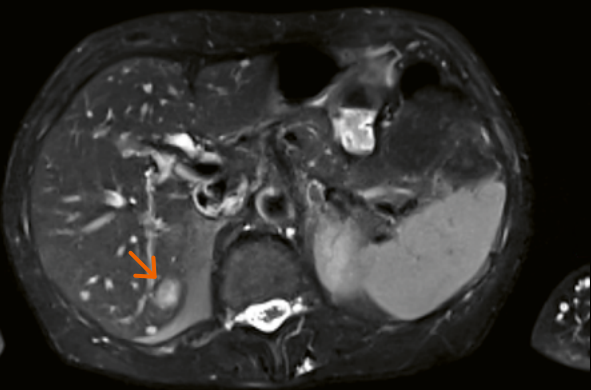
¹MR scanning has not been established as safe for imaging fetuses and infants younger than two years of age. The responsible physician must evaluate the benefits of the MR examination compared to those of other imaging procedures.



1A

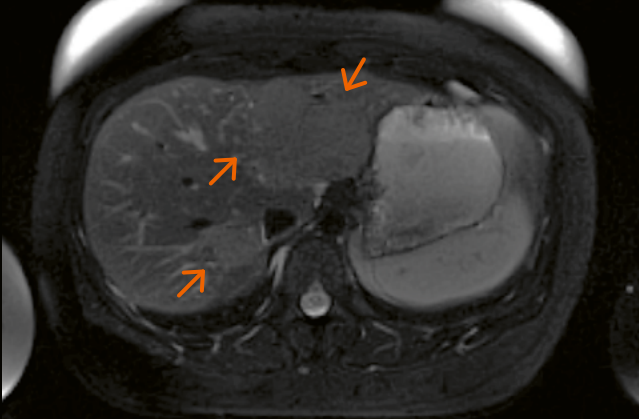


1B

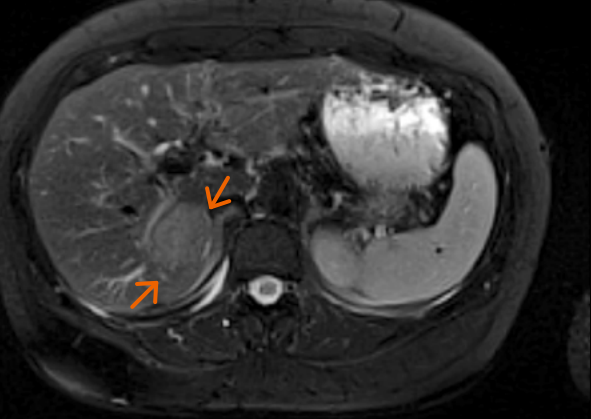


- 1** An 82-year-old female patient with hepatic angiomyolipoma. (1A) T2-weighted FS BLADE TSE and (1B) T2-weighted FS DL HASTE. Similar lesion conspicuity with significantly reduced acquisition time for DL HASTE, and higher SNR in the liver on DL HASTE images.

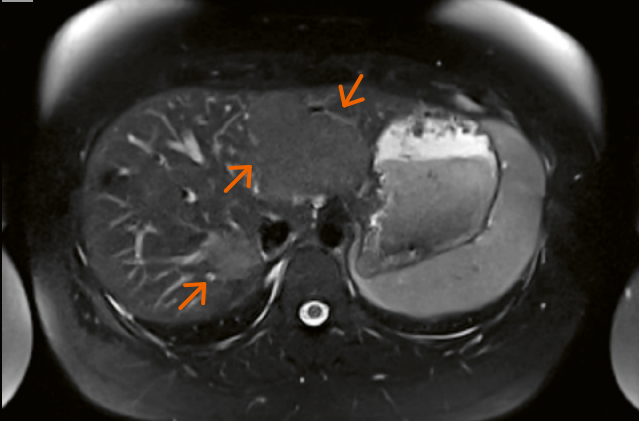
2A



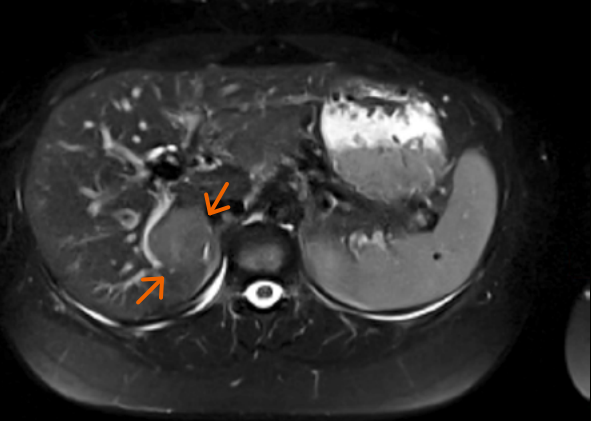
2B



2C



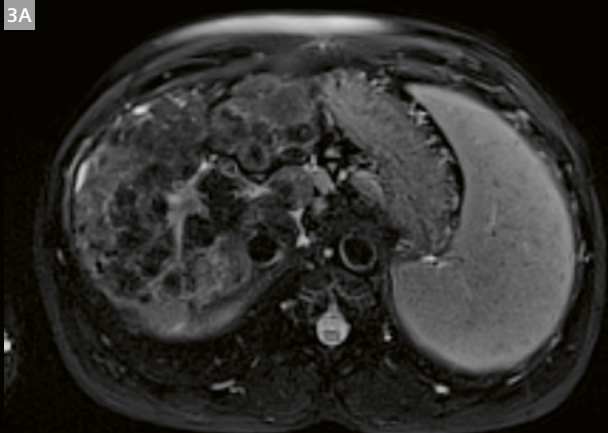
2D



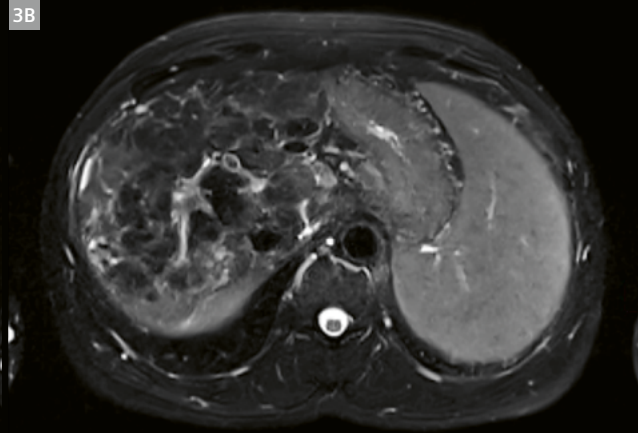
- 2** A 31-year-old female patient with focal nodular hyperplasia. (2A, B) T2-weighted FS BLADE TSE and (2C, D) T2-weighted FS DL HASTE. DL HASTE provides higher lesion-to-liver contrast and sharper lesion delineation.



3A



3B

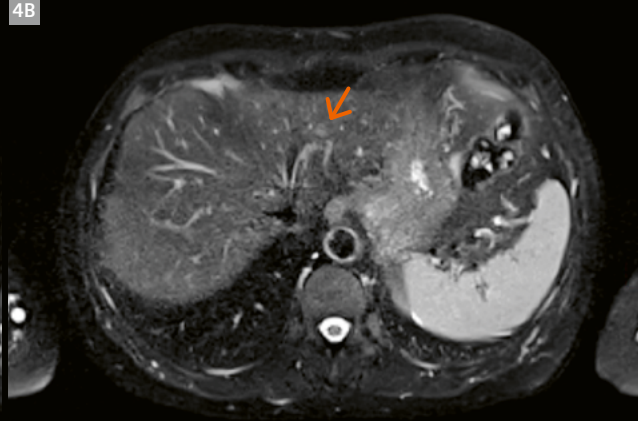


- 3** A 49-year-old male patient with sarcoidosis nodules. (3A) T2-weighted FS BLADE TSE and (3B) T2-weighted FS DL HASTE. There is higher lesion conspicuity and lesion-to-liver CNR of multiple hypointense liver nodules on the DL HASTE images.

4A

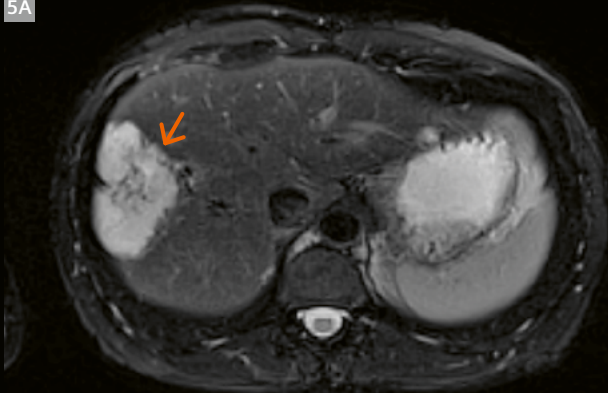


4B

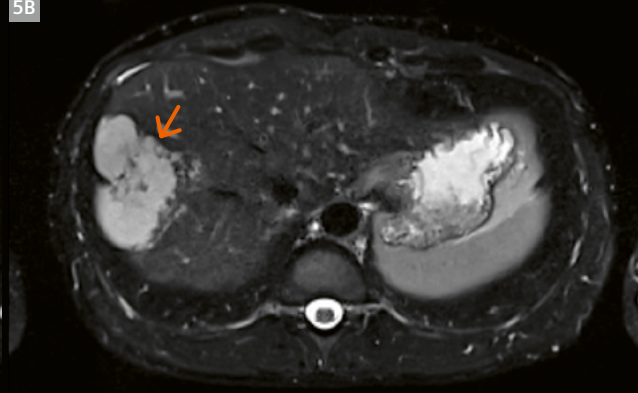


- 4** A 72-year-old female patient with focal nodular hyperplasia. (4A) T2-weighted FS BLADE TSE and (4B) T2-weighted FS DL HASTE. The lesion is not seen on the BLADE image (4A) but is individualized on the DL HASTE image (4B).

5A



5B



- 5** A 48-year-old male patient with atypical hemangioma. (5A) T2-weighted FS BLADE TSE and (5B) T2-weighted FS DL HASTE. The DL HASTE image shows sharper lesion conspicuity and higher liver SNR.



Deep learning HASTE

The introduction of a novel image reconstruction method usually referred to as deep learning reconstruction [2, 3] can potentially overcome the abovementioned challenge in HASTE imaging (and other MR imaging problems). Instead of a conventional Fourier transformation of the acquired k -space data, a deep neural network is used to translate frequency information into the image domain as described in detail elsewhere [4]. In short, high-quality HASTE raw data and respective images were acquired as ground truth information. A neural network was then trained to “associate” down-sampled raw data (achieved by retrospectively removing k -space data, thereby simulating higher parallel imaging factors) with high-quality output images. If the trained network is then presented with highly undersampled input data, high-quality images can be reconstructed while conventional reconstruction would result in artifacts and low SNR. The main advantages of Deep Learning HASTE are increased SNR, improved image contrast, and reduced T2 blurring by shortening the echo train with parallel imaging. Another advantage is the reduction in the specific absorption rate (SAR often presents a challenge in HASTE acquisitions, particularly at 3T), which allows substantial reductions in TR and therefore acquisition time.

Materials and methods

At our institution, we had access to a prototypical implementation of the DL HASTE sequence². All patients underwent a multiphase liver MRI examination in a clinical 1.5T MR system (MAGNETOM Avanto^{fit}, Siemens Healthcare, Erlangen, Germany) in supine position with an 18-channel body array and a 32-channel spine array. We used two sequences:

- Multiple-breath-hold, fat-suppressed Turbo Spin-Echo T2-weighted (TSE BLADE) with an average acquisition time of ~ 2.5 minutes
- Single-breath-hold, fat-suppressed Half-Fourier Acquisition Single-shot Turbo Spin-Echo T2-weighted sequence with deep learning reconstruction (DL HASTE), with an average acquisition time of ~ 18 seconds

We present a series of clinical cases which show that DL HASTE provides similar image quality and diagnostic information as the longer conventional, triggered BLADE acquisition, which is the clinical standard at our institution. These results are also in line with the published literature, which has reported remarkable time savings, as well as comparable image quality and diagnostic confidence for staging hepatic pathologies and characterizing hepatic lesions [4].

²Work in progress. The application is currently under development and is not for sale in the U.S. and in other countries. Its future availability cannot be ensured.

A usual and reasonable concern is that deep learning reconstruction may result in loss of fine structures, eradication of focal lesions, or hallucination of structures that do not exist. Therefore, it is worth mentioning that the reconstruction pipeline is set up in a similar way to clinically accepted and well-established methods, such as compressed sensing reconstruction: several iterations for image improvement are performed within clear and strict boundaries so as not to conflict with physical reality and data integrity.

Both our cohort and the literature gave us confidence that the DL HASTE method is not affected by the abovementioned issues and provides reliable, robust, and high-quality image information in a single breath-hold. We believe the method holds great potential for saving valuable scan time in abdominal MRI studies and beyond.

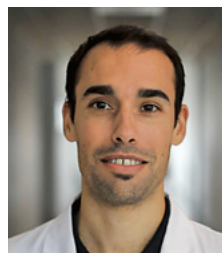
References

- 1 Rosenkrantz AB, Mannelli L, Mossa D, Babb JS. Breath-hold T2-weighted MRI of the liver at 3T using the BLADE technique: impact upon image quality and lesion detection. *Clin Radiol*. 2011;66(5):426–33.
- 2 Schlemper J, Caballero J, Hajnal JV, Price AN, Rueckert D, et al. A Deep Cascade of Convolutional Neural Networks for Dynamic MR Image Reconstruction. *IEEE Trans Med Imaging*. 2018;37(2):491–503.
- 3 Hammernik K, Klatzer T, Kobler E, Recht MP, Sodickson DK, Pock T, et al. Learning a variational network for reconstruction of accelerated MRI data. *Magn Reson Med*. 2018;79(6):3055–3071.
- 4 Herrmann J, Gassenmaier S, Nickel D, Arberet S, Afat S, Lingg A, et al. Diagnostic Confidence and Feasibility of a Deep Learning Accelerated HASTE Sequence of the Abdomen in a Single Breath-Hold. *Invest Radiol*. 2021;56(5):313–319.



Contact

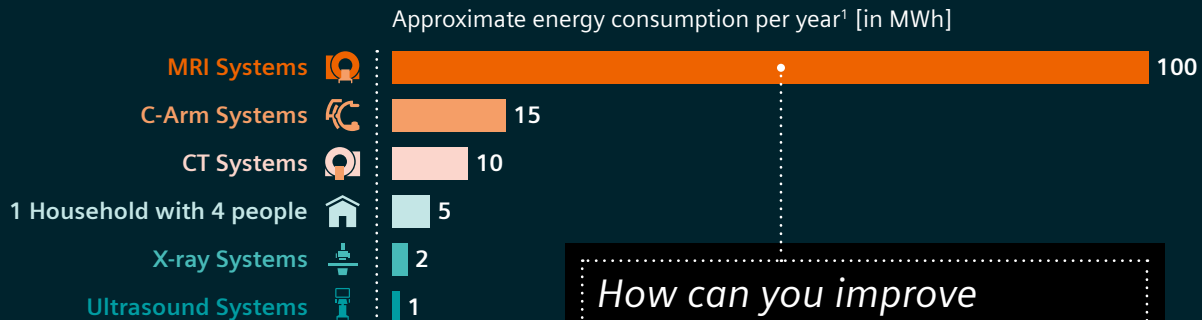
Professor Alain Luciani, Ph.D., M.D.
Hôpital Henri-Mondor
HU Henri Mondor,
Medical Imaging Department,
APHP, UPEC University
51 Avenue Mal De Lattre De Tassigny
94000 Créteil
France
alain.luciani@aphp.fr



Sébastien Mulé, M.D., Ph.D.
HU Henri Mondor
Medical Imaging Department,
APHP, UPEC University
51 Avenue Mal De Lattre De Tassigny
94000 Créteil
France
sebastien.mule@aphp.fr

Environmental Sustainability in Magnetic Resonance

MRI is the major contributor in radiology to energy consumption



How can you improve your energy management and save electricity in MRI?



Did you know? We're also working on saving helium!

Zero Helium Boil-off Technology

It was first introduced in 2004 and prevents helium boil-off throughout your scanner's lifetime. It is available for all our MAGNETOM systems.



Up to 37% reduction in helium inventory

A significant reduction in helium inventory is possible with our latest scanner generation.

- Improved magnet & gradient architecture
- Strong reduction of conductive materials
- More efficient cooling

DryCool Technology

Our new class of MRI systems offers you the most compact whole-body MRI with virtually helium-free infrastructure and radically simplified infrastructure requirements:

- Only 0.7 liters liquid helium
- Sealed-for-life magnet design
- No quench pipe
- New benchmark in ramp-up times

Values are computed for a 1.5T MAGNETOM Sola system for illustration purposes.

¹ Data Siemens Healthineers own measurements and assumptions; Actual consumption can vary depending on use pattern, system type, and configuration.

² Assuming the system is turned on during the weekends and overnight.

³ Results are quantified assuming scanning operations as per COCIR standards.

How to save energy with your MRI system:

Energy consumption for an MRI system in one year, if the scanner is always on²: **100 MWh**



Save ~20% energy by turning off your scanner when not in use³ **~80 MWh**



Did you know?

The start-up time for our scanners is only approx. 5.5 minutes and with our System Start-Up Timer you can enable automatic start-up of your scanner. So your system is ready when the workday starts!

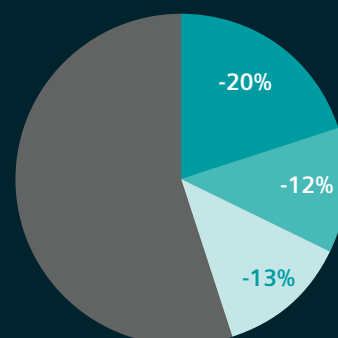


Save ~12% energy by using Eco Power mode³ **~70 MWh**



Save ~13% energy by using Deep Resolve **~60 MWh**

Make the most of our innovations and save **~40%** energy!



Learn more about Abdominal and Oncological Imaging

Lectures and presentations given at the MAGNETOM World Summit are available on demand

Free-breathing Abdominal MRI and Liver Fat Quantification

Holden H. Wu (David Geffen School of Medicine, University of California, Los Angeles, CA, USA)

The Role of MRI in the Management of Diffuse Liver Disease

Kartik S. Jhaveri (University Health Network, Toronto, Canada)

Quantitative MR Imaging: Application in Pancreatic Diseases

Liang Zhu (Peking Union Medical College (PUMC), Beijing, China)

Rectal Cancer Staging and Evaluation of Response

Bachir Taouli (Icahn School of Medicine at Mount Sinai, New York, NY, USA)

Minimal Invasive Image-Guided Therapy of Primary and Secondary Liver Disease

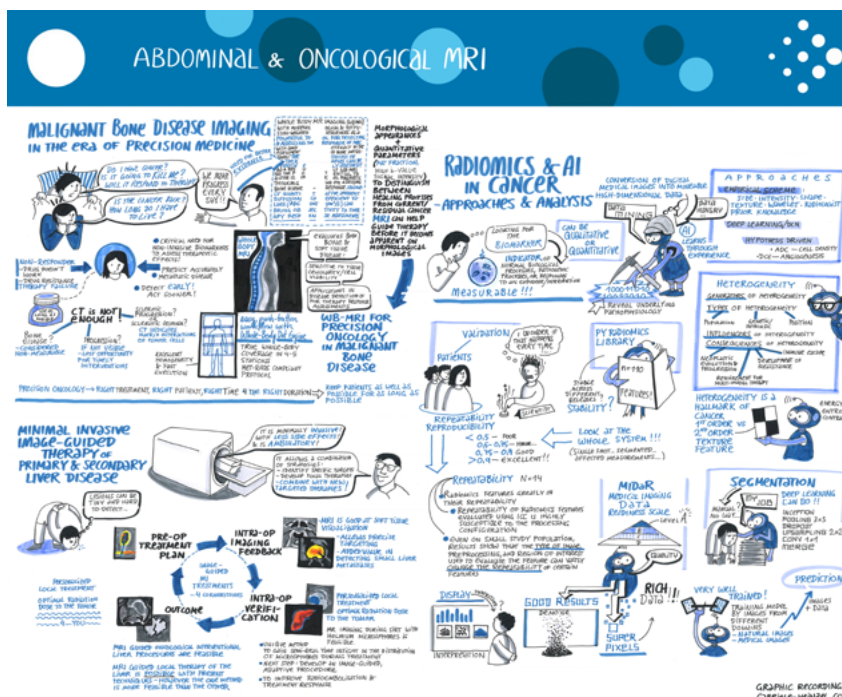
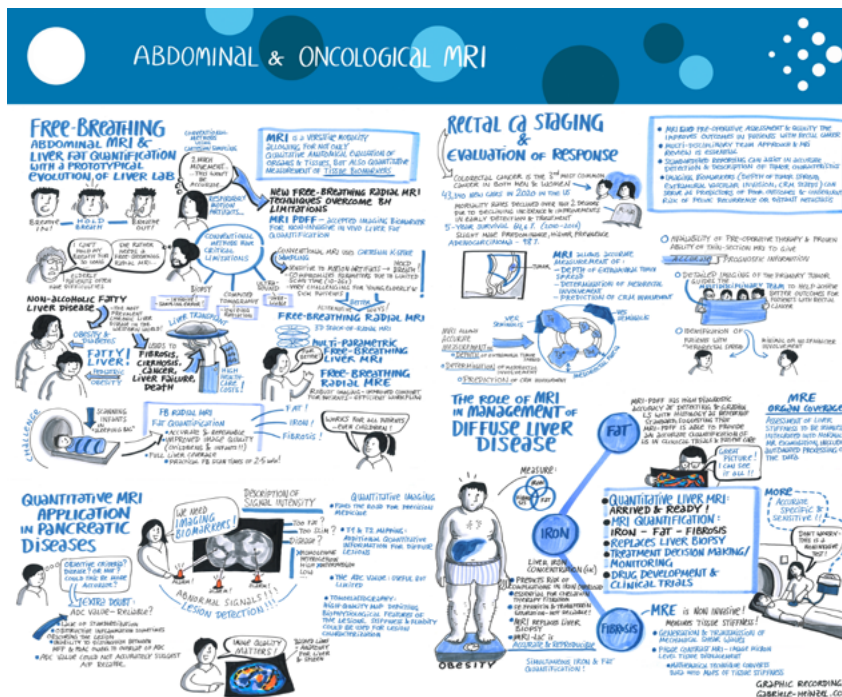
Jurgen Fütterer (Radboud University Medical Center, UMC, Nijmegen, The Netherlands)

Malignant Bone Disease Imaging in the Era of Precision Medicine

Anwar R. Padhani (Strickland Scanner Centre, Mount Vernon Cancer Centre, London, UK)

Radiomics and AI in Cancer – Approaches and Analysis

Masoom Haider (Sinai Health System & University Health Network, Toronto, Canada)



Don't miss this valuable source of information

<https://www.magnetomworld.siemens-healthineers.com/magnetom-world-summit/recordings/abdominal-oncological>

Graphic recording:
www.gabriele-heinzel.com



Fast, Standardized, and Robust Imaging with BioMatrix and Compressed Sensing GRASP-VIBE

Johan Dehem, M.D.

VZW Jan Yperman, Ypres, Belgium

When high-tech applications leave the shelter of the lab and come to the hospital to face real clinical challenges, the question arises: Does it work? Spoiler alert: The answer can be found in the images.

Upon arrival of the 1.5T MAGNETOM Sola, the first thing you notice is the small bump in the back. Since the magnet is such a short bore system, which I can literally hold in my arms, this rear extension is a quite logical way to support table movement beyond the bore.

Indeed, patient friendly magnets should be as short as possible. Speaking of patient comfort, listen when you move the table; you can't hear it. It's smooth and slides silently in place, in sharp contrast to the high-pitched shrieking on older systems. The acoustic isolation from gradient power has also improved. Many patients in follow-up studies spontaneously mention a more quiet noise level throughout the exam.

Another innocuous, innocent looking, but much appreciated change is the head coil. For the first time ever, it's tiltable! Slight tilting of the head is preferred by many patients and helps them to relax. It's also very

much appreciated by sick and older patients or those with kyphosis or other malformations, since we no longer need to tilt the patient until the head fits but simply tilt the head coil. Together with the standard leg support, every patient fits. It's a small tilt for the coil, but a giant leap for patient comfort.

Patient comfort is one thing, how about operator comfort? Well, MAGNETOM Sola has some appealing tricks up its sleeve to charm the technologists. Patient positioning, for example, is done automatically; you just acknowledge by pressing the Go button and you're done. Using the laser beam to position suddenly seems so last century. Moreover, this automatic positioning avoids suboptimal positioning or even errors by eliminating interoperator variability, regardless of your patient's body type. As a result, scanning is always in local mode, which is less shim-dependent and hence faster (except for large FOV exams). Together with AutoAlign and AutoCoverage in the Dot engines, a highly standardized and robust examination quality results. DotGO and Dot engines are a match made in heaven! (Actually, a match made in Germany).

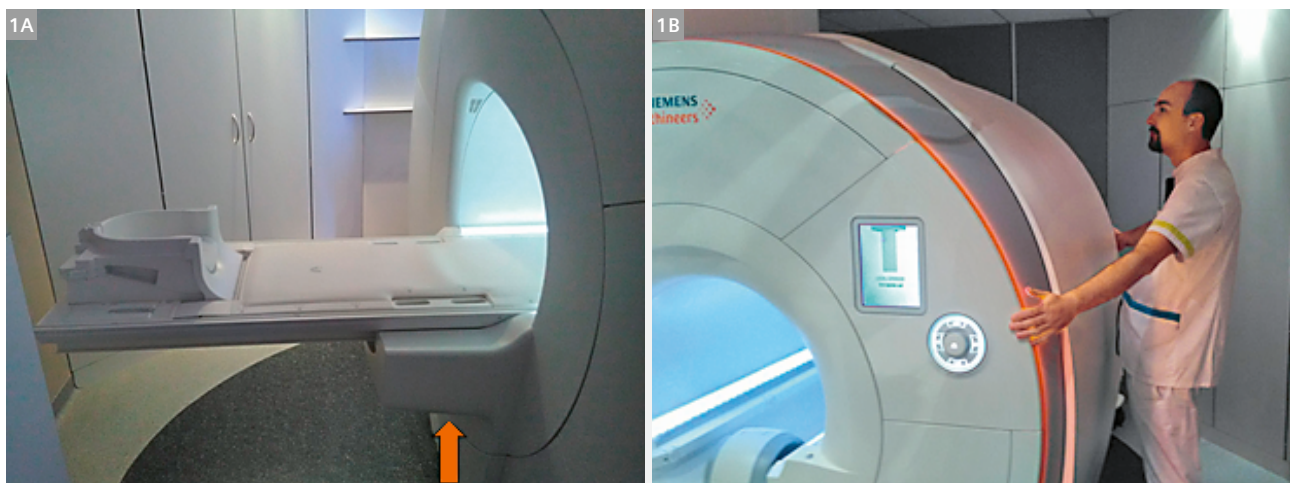
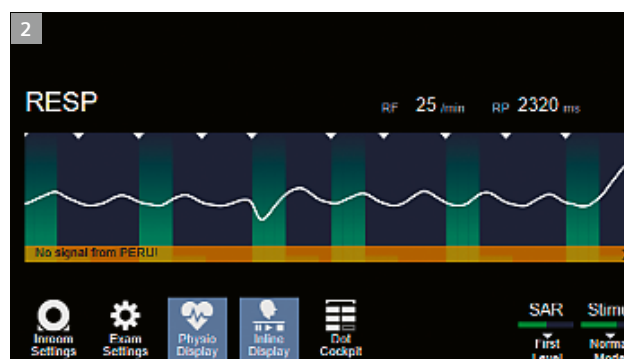


Figure 1:

The support in the back is needed since the magnet is so short that a person can easily hold the magnet in their arms. It may be quite an unusual feature; however it is a reliable parameter to determine if your magnet is patient friendly.

The user interface has changed quite a bit – dramatically in fact; however, we didn't complain about the transformation at all because it has changed for the better! For example, you can actually scroll through the images in the graphic segments, speeding up and improving the accuracy of planning. Or double click and have your planning stack in full screen. The dual screen setup at the console is efficient at separating scanning workflow from viewing, postprocessing, and archiving. Another benefit is the distribution of images where complex multiphase, multiseries studies are neatly presented in a graphic overview, guiding you to send only the relevant series to the PACS system instead of blindly dumping images.

The built-in respiratory sensor is helping us in different ways. First, if you ask your patient to hold their breath, you get a direct view if the breath-hold is properly done. If your patient is sick, you keep an eye on the respiration frequency together with the ECG. Second, the BioMatrix Sensor is robust and reliable for triggering T2 TSE, HASTE, or DWI acquisitions of the liver. There is no need to put on a respiratory belt and no scanning time is lost with the navigator. A kinetic sensor and beat sensor are in the development pipeline and I am eager to see if they perform just as well.



Now that we have touched on the subject of breath-holding, it seems a good time to mention that not every patient is very good at holding their breath, especially on command. On the Aera, we used StarVIBE to minimize respiratory movement artifacts (at the cost of dynamic contrast enhancement information), the Sola with GRASP-VIBE excels at getting rid of these artifacts while maintaining all the dynamic information over time. It turns out image quality that is surprisingly good, giving pristine images in not-so-compliant patients.

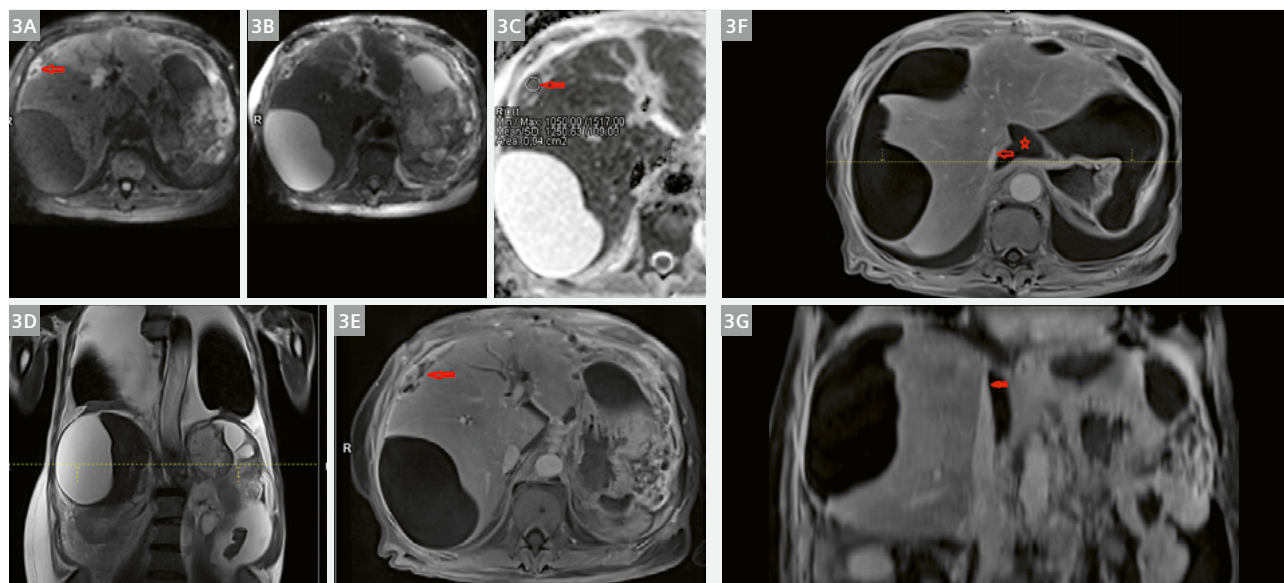


Figure 3: This 73-year-old male presented with shortness of breath and leg swelling. History of pancreatectomy and duodenectomy for pancreas cancer

DWI with high b-value (3A), low b-value (3B), and ADC map (3C). Coronal HASTE (3D, E). Note the coverage was head to feet with GRASP-VIBE for artifact-free free-breathing T1 imaging, demonstrating peritoneal implant (red arrow). Ascites (dielectrical effect) and massive pleural fluid are challenging image quality. Shortness of breath is immediately explained by the massive pleural effusion and compression atelectasis.

GRASP-VIBE free-breathing acquisition in the venous phase (3F) depicts the severe extrinsic compression of the inferior vena cava (red arrow) in diaphragmatic hiatus explaining edema and swelling of the lower limbs. Since slice thickness is 2.5 mm, you can reconstruct coronal images to better delineate anatomical landmarks.



To be honest, the gold standard breath-holding acquisition itself is quite limited in temporal resolution (it takes time for the patient to breathe in and out between different phases) and you need to time your acquisition very well to have a crisp arterial phase; whereas in GRASP-VIBE, the acquisition simply keeps going while the patient is quietly breathing; hence, GRASP-VIBE does not simply maintain dynamic information, but actually enhances time resolution giving you, for example, three arterial phases in liver imaging. Here, the time resolution was just 7 seconds.

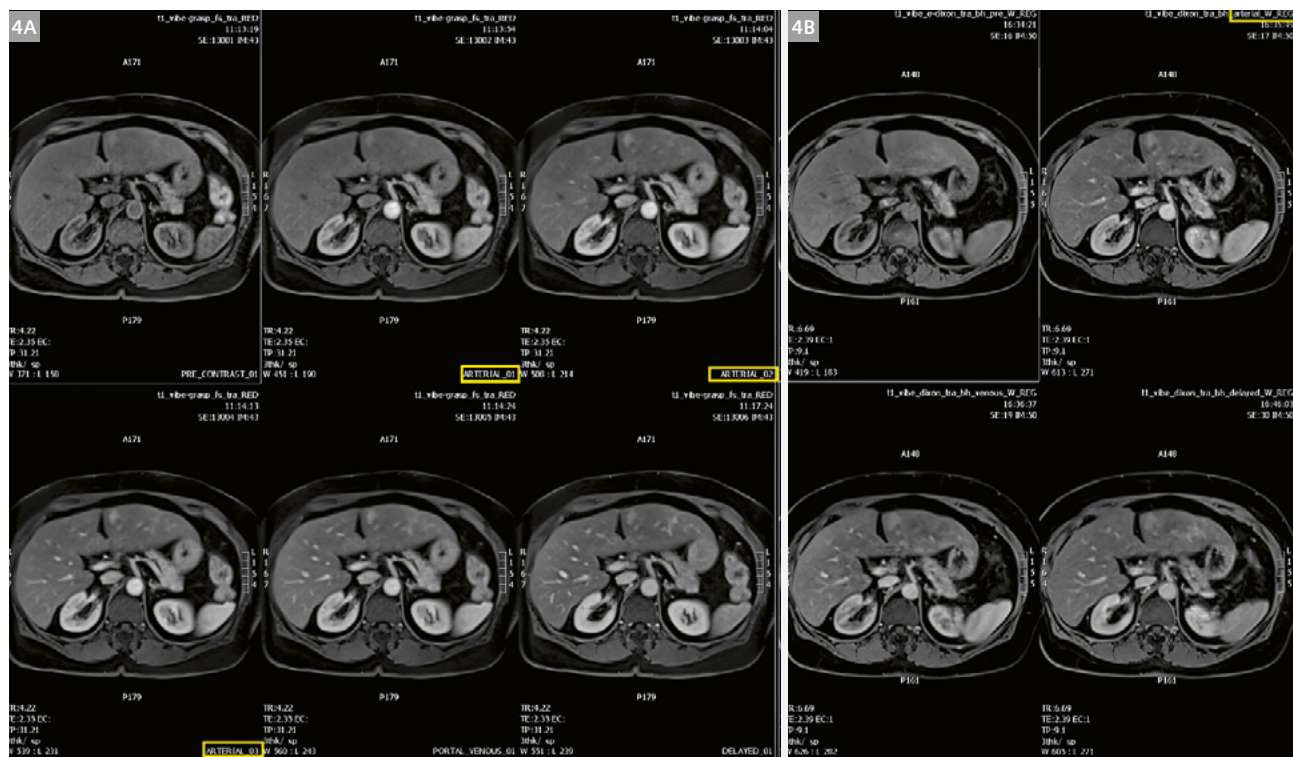


Figure 4:

(4A) Three columns showing reduced reconstruction sets of GRASP-VIBE with three arterial phases (yellow box); (4B) two columns showing previous exam using CAIPIRINHA 4 VIBE on the Aera with standard single arterial phase (yellow box).

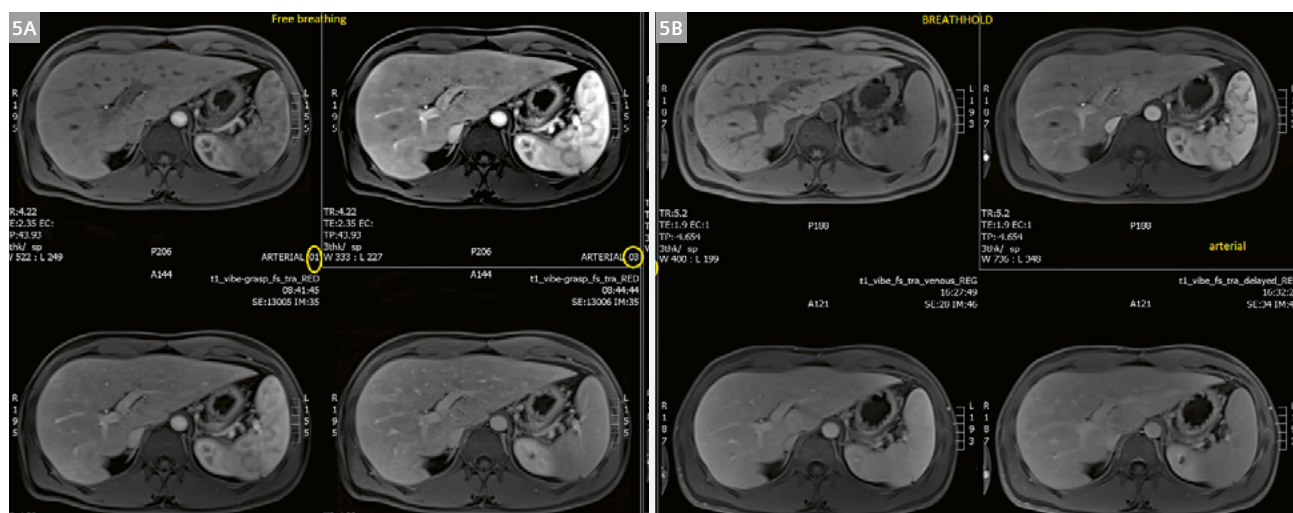


Figure 5:

(5A) When comparing this free-breathing GRASP acquisition in this young and cooperative patient, the quality of the free-breathing series equals that of the best CAIPIRINHA 4 VIBE technique (5B) we had available last year; however, you have much higher temporal resolution with more phases, e.g., three consecutive arterial phases (arterial 01 and 03 are depicted, phase 02 is left out for sake of comparison).

For older and sick patients, free breathing makes an even bigger difference with better image quality in addition to higher temporal resolution.

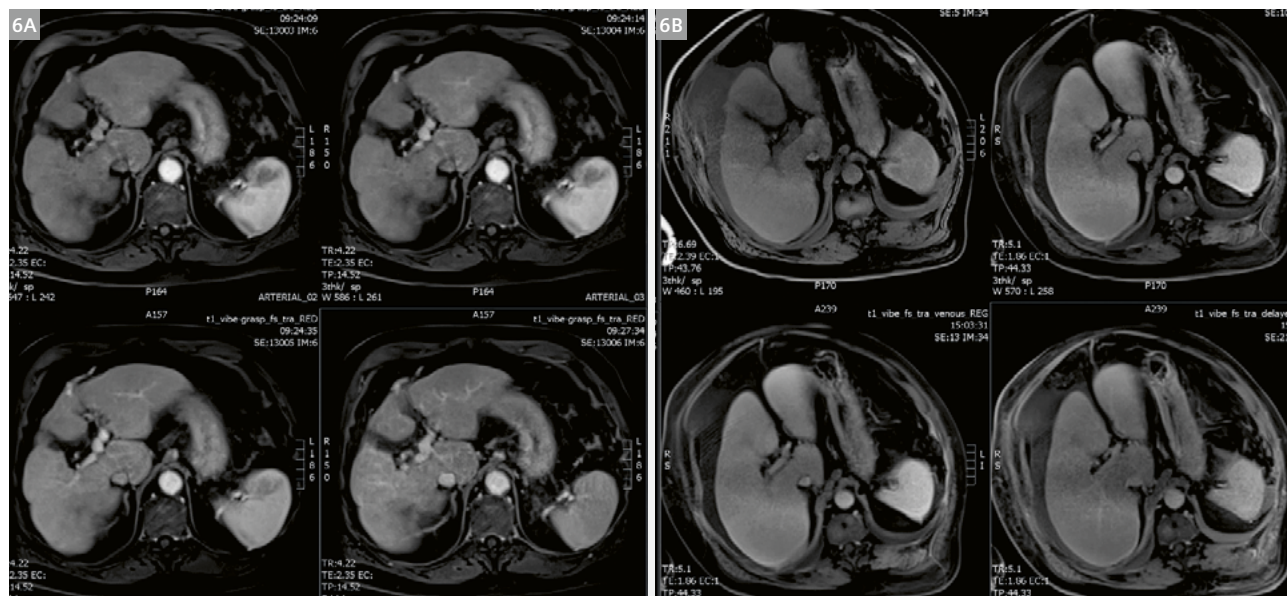


Figure 6:

In this 76-year-old patient with advanced liver cirrhosis, the GRASP-VIBE exam (6A) compared side-by-side with previous exam (6B; at 70 years) shows the portal vessels and the recanalized umbilical vein to a far better extent. This improved image quality is achieved despite the fact that patient is 6 years older and, worse, at an more advanced stage of cirrhosis. In addition to the image quality improvement, instead of one weak arterial phase, we have three confident arterial phases!

GRASping dynamic inflow information is actually new and makes GRASP a new tool to help differentiate liver lesions.

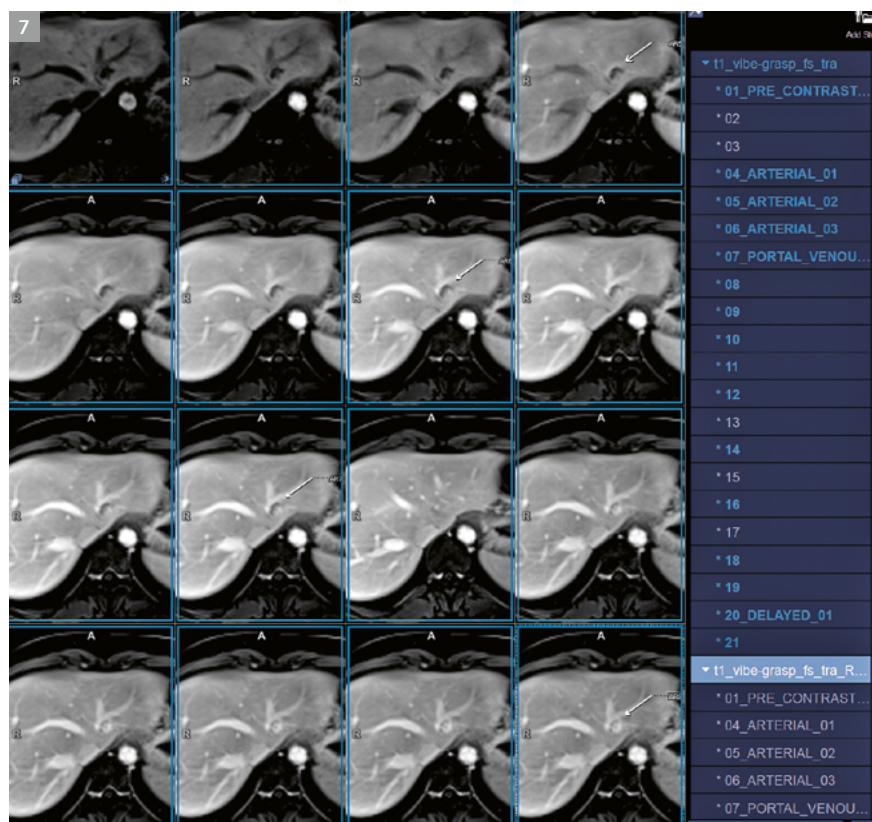


Figure 7:

Classic filling of liver hemangioma (arrow); however, with no breath-holding, time resolution 7 seconds, 3 mm slice thickness. The system automatically detects contrast bolus arrival and labels the phases accordingly. For convenience, a reduced dataset containing only the relevant, labelled phases (scroll down menu on the right side of the image series) is prepared, which can be sent separately to the PACS.

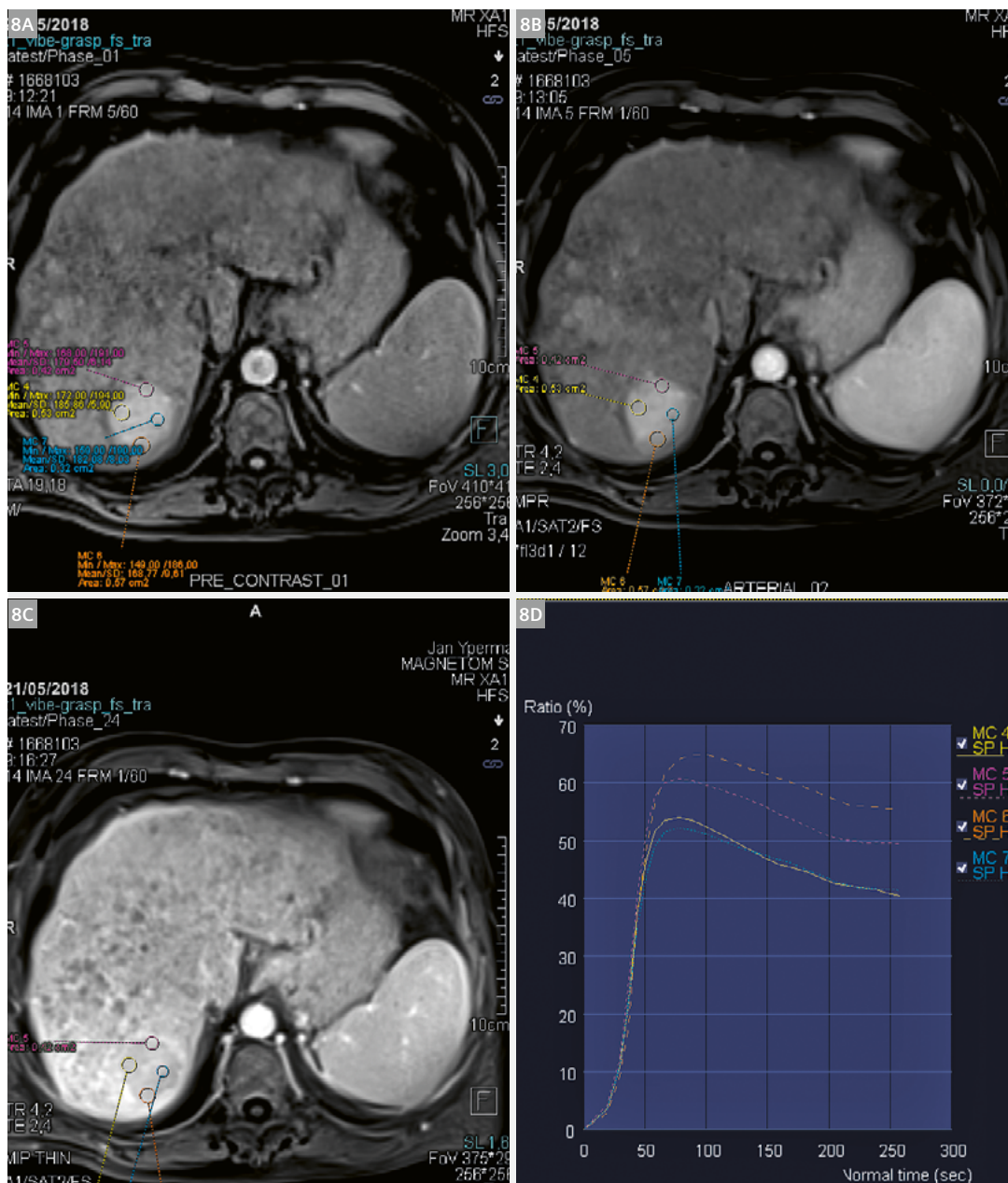


Figure 8: Large HCC with selected images T1 fatsat precontrast (8A), arterial enhancing (8B), and washout on delayed phase (8C) with the corresponding high quality contrast enhancement curve over time resulting from the high temporal resolution sampling in 4D GRASP. One can actually see the washin in the upper row and the washout in 8D.

4D GRASP can also showcase dynamic filling, for example, of the mesenteric vessels, or even give an impression as to how organs are moving or are restricted in movement. In GRASP liver imaging, the reconstructor receives a respiration-dependent fluctuating signal. This respiratory information in the dataset is actually used to gate the reconstructions in expiratory phases only when wanted (our standard approach in liver imaging). This is convenient when reading/reporting the GRASP-VIBE dynamic series side-by-side with T2 and diffusion-weighted imaging, where having the same position in slices facilitates lesion recognition and characterization. GRASP-VIBE is also outperforming breath-hold imaging in this practical reading aspect.

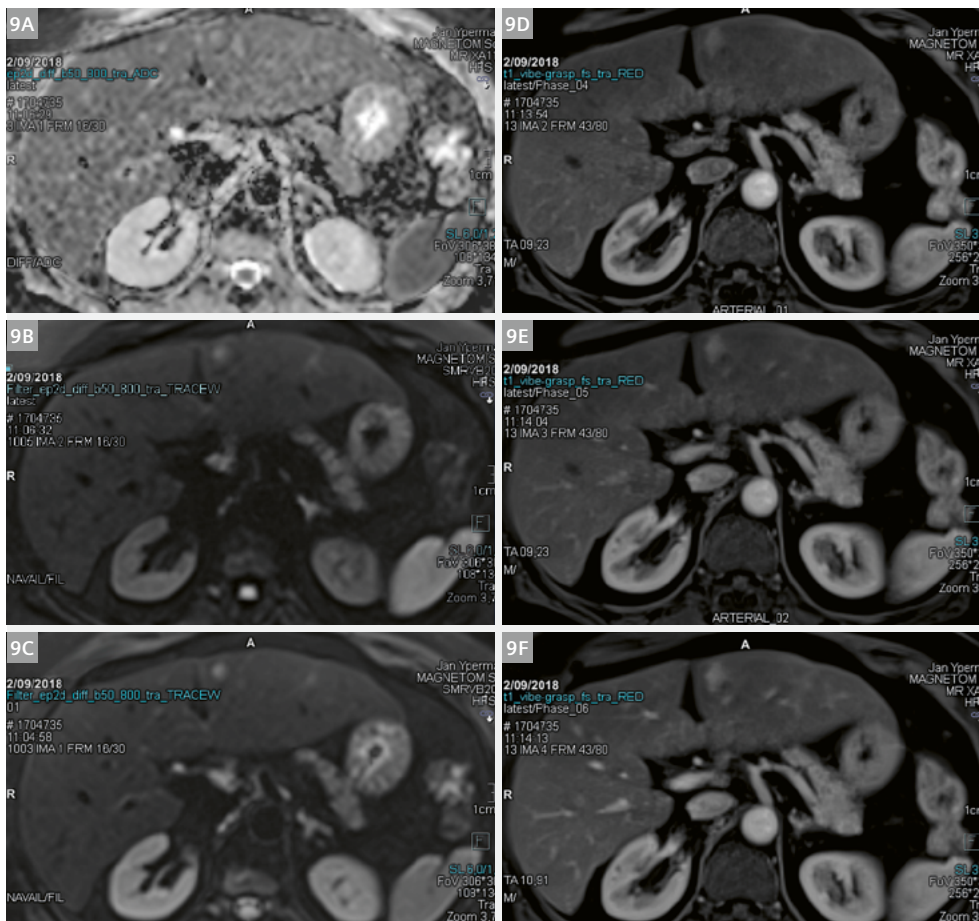


Figure 9:
The DWI (9A–C)
nicely match the three
arterial phases in a row
(9D–F) making
lesion detection and
characterization easier
and more reliable.

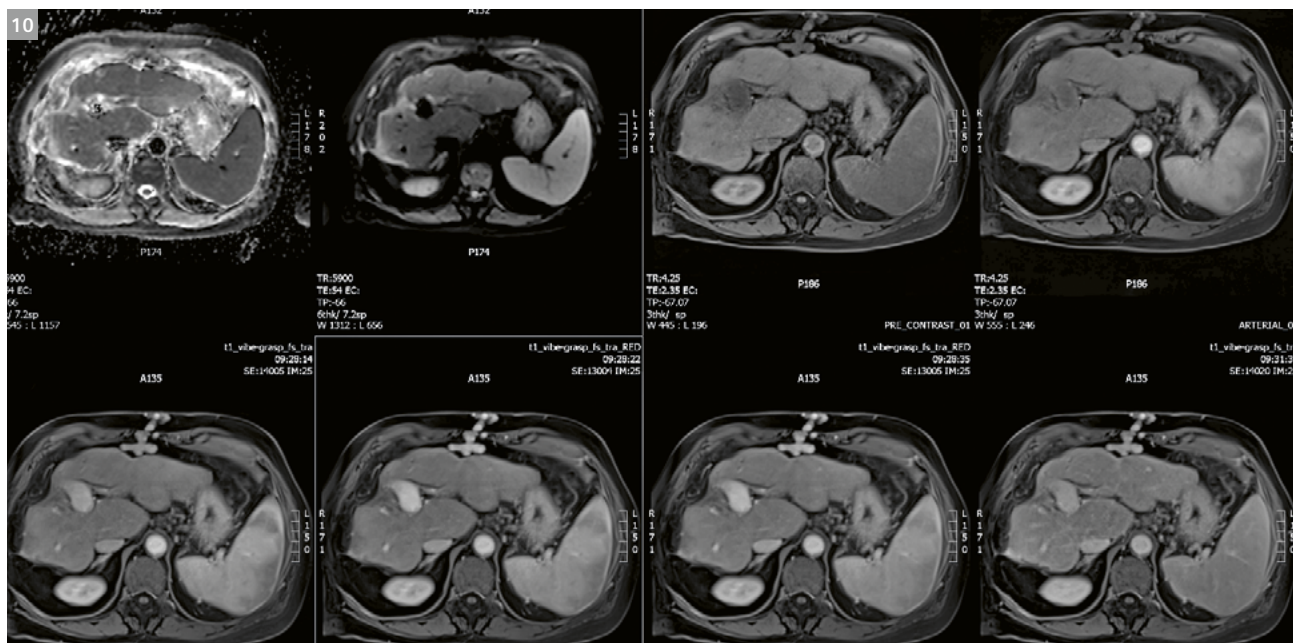


Figure 10:
Macronodular liver cirrhosis with recanalized umbilical vein; effortless dynamic imaging is perfectly aligned with the DWI thanks to the reconstruction in the expiratory phase.



Without respiratory gating in reconstruction, we can take temporal and spatial resolution even higher – as high as 28 slices x 1 mm in-plane, 3 mm thick every 3 seconds as in this case of fibromuscular stroma carcinoma of the prostate extending in the transition zone. Just as in liver imaging, side-by-side comparison with DWI is able to “resolve” prostate issues with amazing simplicity and accuracy.

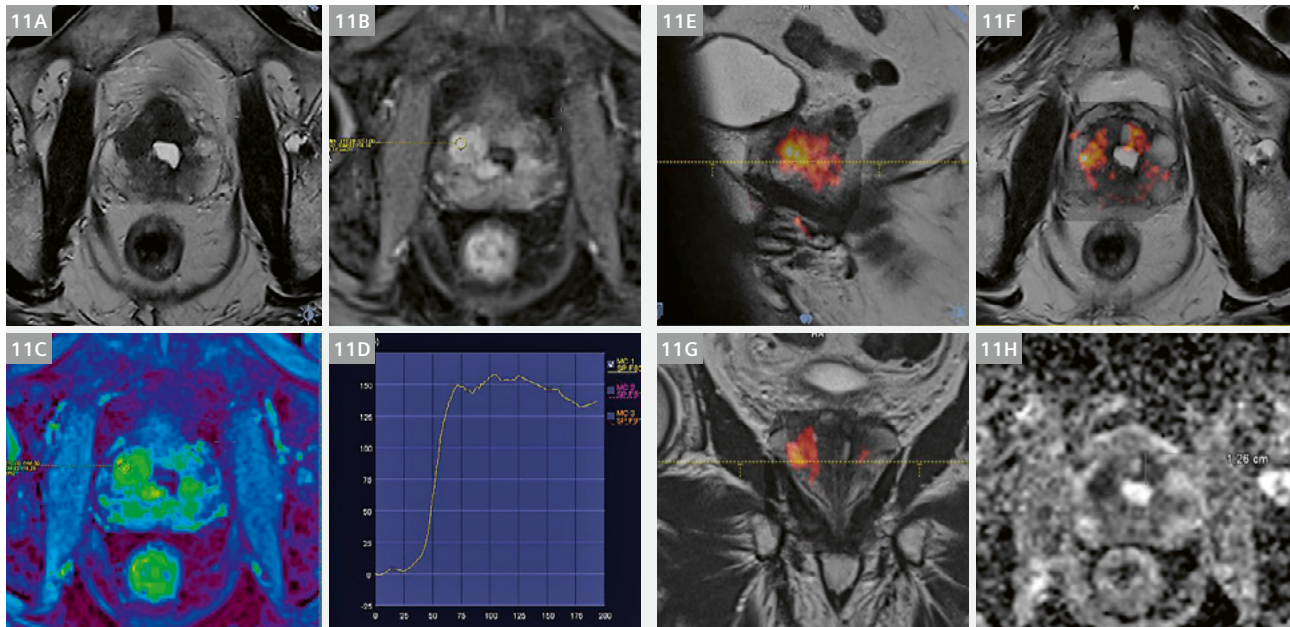


Figure 11:

Axial T2 (11A) demonstrating charcoal-like dark mass, capsule retraction. Fusion images of high b-value and T2 demonstrating diffusion restriction in the T2 dark zones Ax 4D GRASP (11F); wash in-wash out pattern depicted on the graph. ADC map (11H) with restricted diffusion.

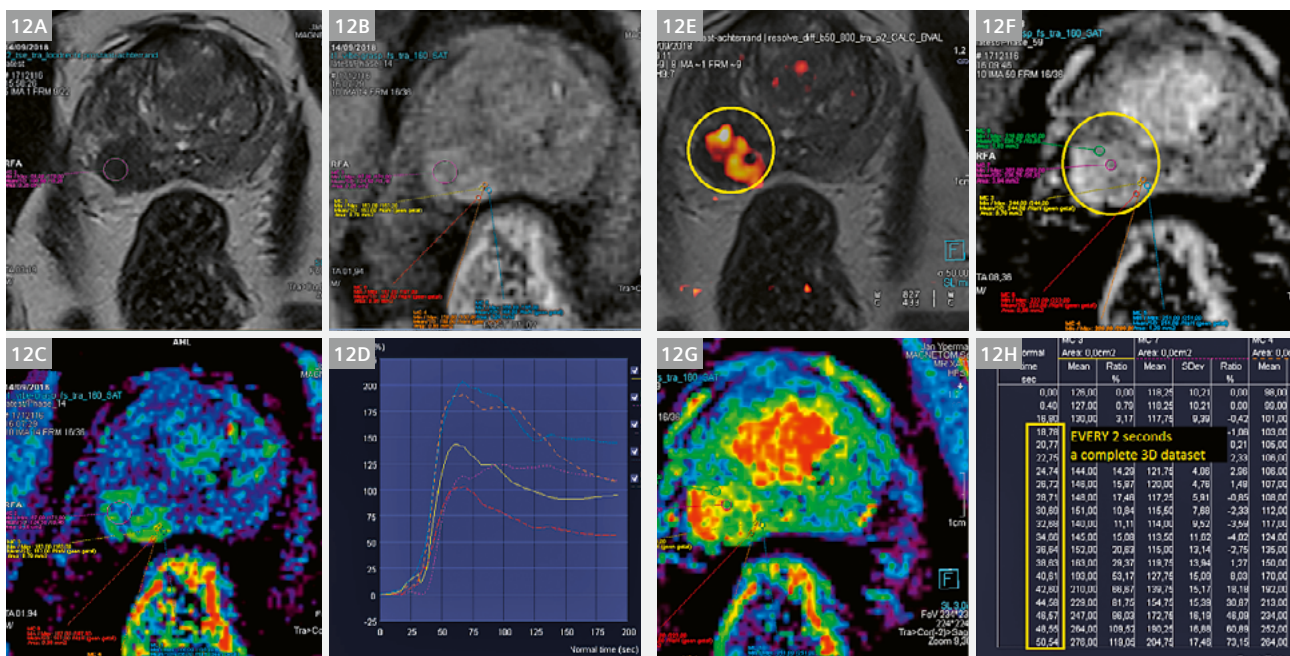


Figure 12:

Besides the contrast enhancement curve, one can see the wash in (12B) in addition to seeing the wash out in (12F) (yellow circle).

Also note the T2 hypointense nodule (12A) and corresponding DWI fusion image with high b-value hyperintensity (12E) (yellow circle). Note time resolution in the mean curve table: 2 seconds for 36 x 3 mm slices; 1 mm in-plane resolution.

GRASP-VIBE is an excellent solution to counter motion artifacts, on the one hand, and for resolving contrast enhancement dynamics, on the other hand, making it ideal for neck imaging¹. In radiology, the neck is also known as the “Great Swallowing Region”.

1 mm in-plane resolution and slice thickness of 1.1 mm, 144 slices covered every 6 seconds artifact-free. This means not only no swallowing artifacts, but also robust fatsat thanks to the CoilShim. This same CoilShim allows perfect DWI in the neck, which was previously difficult to achieve.

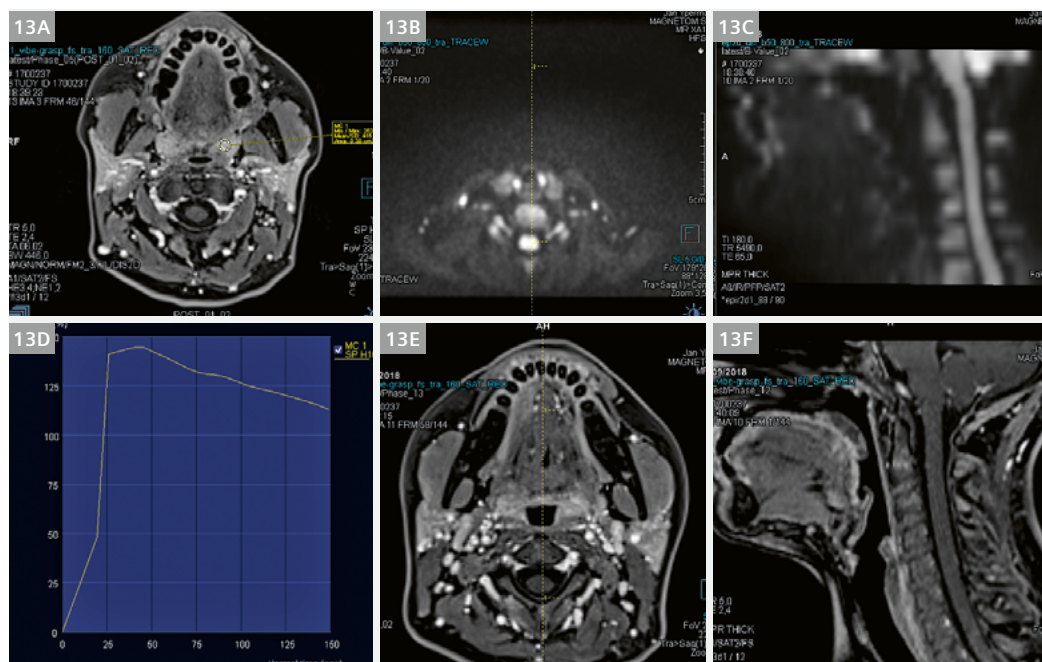


Figure 13:
144 slices in 1.1 isotropic resolution every 6 seconds. (13B, C) Axial DWI high b-value and sagittal MPR of high b-value with no distortion.

Contrast enhancement curve in left tonsil, timepoint every 6 seconds. (13E, F) Axial GRASP-VIBE and sagittal reconstruction: time-resolved and high resolution for high quality MPR reconstructions.

We can push the speed of GRASP acquisition even further; fast enough to grasp the filling of an aneurysm. 1.1 isotropic acquisition matrix and 2.5 seconds temporal resolution.

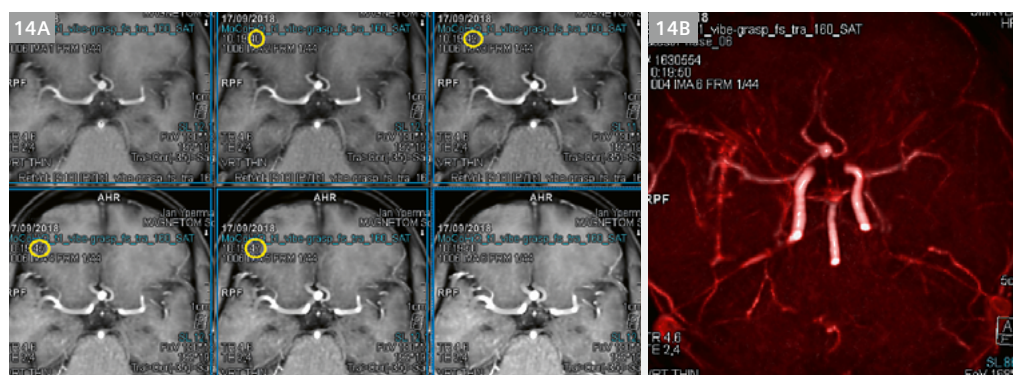


Figure 14:
Thin VRT reconstruction of 4D GRASP, time resolution 2.5 seconds (yellow circle) at 1.1 isotropic spatial resolution. VRT reconstruction single arterial phase from GRASP series; 2.5-second acquisition.

Contact

Johan Dehem, M.D.
Jan Yperman Ziekenhuis
Briekstraat 12
8900 Ypres
Belgium
Phone: +32 57 35 74 00
johan.dehem@yperman.net



¹Compressed Sensing GRASP-VIBE for other regions than liver is not for sale in the U.S.
Intended Use: Compressed Sensing GRASP-VIBE (GRASP = Golden-angle Radial Sparse Parallel MRI) is intended to be used in dynamic and/or non-contrast liver examinations to support patients who cannot reliably hold their breath for a conventional breath-hold measurement.



Fast and efficient liver imaging with Primovist®/Eovist®

Thomas Lamprecht^{1,2}; Martin Rohrer, Ph.D.²; Gregor Thörmer, Ph.D.¹

¹ Siemens Healthineers, Erlangen, Germany

² Bayer AG, Radiology, Berlin, Germany

Introduction

Primovist¹ is a dedicated contrast agent for MR imaging of the liver. It combines the dynamic characteristics of an extracellular contrast agent with characteristics for liver-specific imaging during the hepatobiliary phase [1, 2]. Primovist contains an ionic, highly water-soluble Gd³⁺

chelate complex and therefore has magnetic properties comparable to other gadolinium-containing contrast media that are used to enhance dynamic T1-weighted imaging [3]. The addition of a lipophilic EOB group increases protein binding in plasma and maximizes

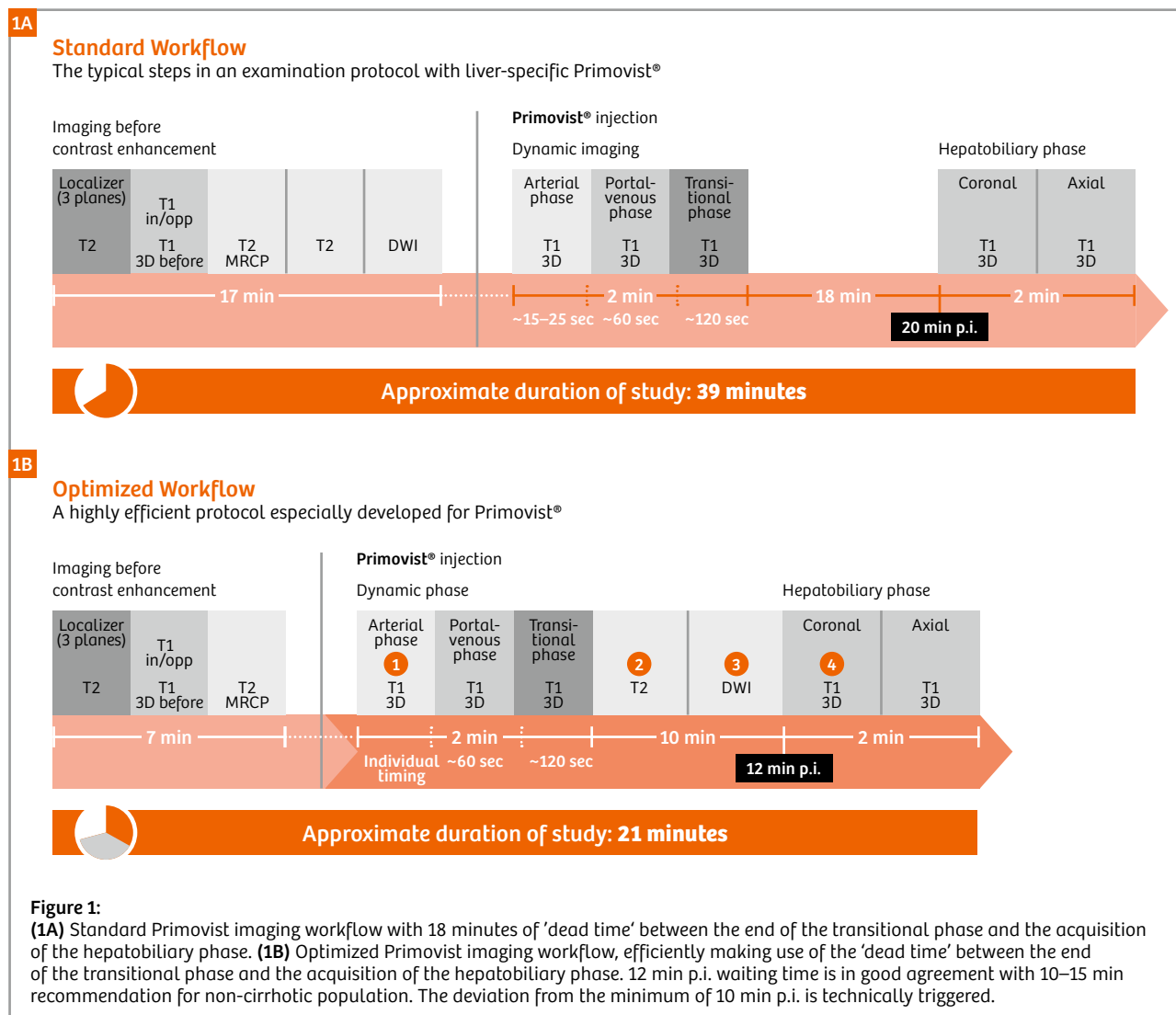


Figure 1 is courtesy of: Elmar M. Merkle, Department of Radiology, Basel University Medical Center, Basel, Switzerland.



contrast medium uptake by the hepatocytes. Once injected, Primovist is taken up by functional hepatocytes, which means that the contrast medium accumulates in the cells. After administration, the signal enhancement in healthy liver tissue is present for at least two hours. Since malignant tumors and non-hepatic tissues (e.g., metastases) possess very few functional hepatocytes, or none at all, they exhibit almost no Primovist uptake. This results in a pronounced contrast between malignancy (dark = hypointense) and adjacent healthy liver tissue (bright = hyperintense). Compared with healthy tissue, benign liver lesions may display an even more pronounced signal enhancement [4].

Since the recommended minimal waiting time of approximately 10 to 15 minutes (for non-cirrhotic population) between contrast media administration and the acquisition of hepatobiliary phase images is relatively short, examinations using Primovist make it possible to avoid taking the patient off the MR table, waiting until contrast accumulates in the hepatocytes, and rescheduling the patient for an additional late-phase scan. Nonetheless, the unused waiting time is still perceived as 'dead time', inevitably resulting in long exam slots (see Figure 1A).

A time-optimized workflow for Primovist liver MRI

In order to make better, effective use of the time between the dynamic and liver-specific phases, it is highly desirable to

- A. shift the time-intensive acquisition of high-resolution T2-weighted images and diffusion-weighted images to after the contrast injection, and
- B. shorten the delay between contrast dynamics and the acquisition of hepatobiliary phase images.

With this in mind, respective studies have been undertaken which show that Primovist does not have any significant impact on the signal of the liver parenchyma in T2-weighted [5] or diffusion-weighted sequences [6]. Furthermore, a fairly marked liver-specific contrast enhancement will already be present after 10 minutes in patients without liver cirrhosis. This will only increase slightly up to 20 minutes after contrast injection [7]. Accordingly, Bayer has suggested a shortened Primovist imaging protocol which allows performing a complete Primovist examination in a 30-minute exam slot (Fig. 1B).

In this article, we present three optimized workflows for efficient imaging with Primovist:

- Two standard strategies without additional license requirements
- One strategy using advanced Abdomen Dot Engine features such as automated slice positioning, auto coverage, and ABLE² for personalized timing of the arterial phase thanks to automated bolus detection, and automated adjustment of breath-hold times to individual patient capabilities.

Respective protocols for the 1.5T and 3T platforms are available to download on the MAGNETOM World website at www.siemens.com/magnetom-world > **Clinical Corner** > **Protocols**.

Primovist standard protocols

The standard protocol set for liver imaging with Primovist provides two different strategies: The default imaging strategy uses automated breath-hold commands during exhalation, while the alternative strategy uses breath-hold commands during inhalation. Before starting the actual examination, users can decide on the exam strategy (see Figure 2). Depending on this decision, respective protocols are automatically pulled into the exam queue. Figure 3 illustrates the flow of the two different strategies. The default strategy deliberately uses exhalation. Even though patients perceive breath-holding during exhalation to be more demanding, the literature shows that the stability and reproducibility is higher [8]. In addition, planning images can be used throughout the entire exam for both breath-hold and free-breathing acquisitions. The alternative strategy using inhalation includes additional planning images, since the free-breathing and triggered exams (T2-weighted and diffusion-weighted) should not be planned on images acquired during inhalation (see Figure 4).

The actual exam starts with the acquisition of localizer images. These are followed by fast overview scans with a single-shot T2 HASTE technique in coronal and axial orientation. If preferred, T2 BLADE scans may be used instead of a breath-hold T2 HASTE approach. Depending

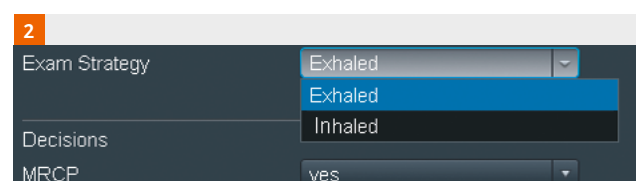


Figure 2: Prior to the exam, users can choose the strategy from the dialog box. In this step, they can also decide whether the individual clinical question requires a fast T2-weighted MRCP.

¹ The information shown herein refers to products of 3rd party manufacturers and thus are in their regulatory responsibility. Please contact the 3rd party manufacturer for further information.

² Automated Breath-hold Liver Exam



	Expiration	Inspiration
3A	✓ localizer_haste_multislice 00:18 t2_haste_cor_p2_mbh 00:48 t2_haste_tra_p2_mbh_320 01:08 t1_t2d_opp-in_tra_p2_mbh 00:45	localizer_haste_multislice 00:18 t2_haste_cor_p2_mbh 00:48 t2_haste_tra_p2_mbh_320 01:08 t1_t2d_opp-in_tra_p2_mbh 00:45
3B	MRCP yes t2_haste_fs_multislab_p2_384_mbh 00:47 t1_vibc_dixon_tra_p4_bh_prc 00:15 prepare injection t1_vibe_dixon_tra_p4_bh_arterial 00:15 t1_vibe_dixon_tra_p4_bh_portal-venous 00:15 t1_vibe_dixon_tra_p4_bh_delayed 00:15	MRCP yes t2_haste_fs_multislab_p2_384_mbh 00:47 t1_vibc_dixon_tra_p4_bh_prc 00:15 prepare injection t1_vibe_dixon_tra_p4_bh_arterial 00:15 t1_vibe_dixon_tra_p4_bh_portal-venous 00:15 t1_vibe_dixon_tra_p4_bh_delayed 00:15
3C		
3D	ep2d diff b50 400 800 tra p3 03:35 T2 options 2d_T2_TSE t2_tse_tra_p2_trig_512 02:59 3d_T2_SPACE_dark vessel t2_space_fs_tra_p2_trig_512 05:11 t1_vibe_dixon_tra_p4_bh_12min_p.i_higher FA 00:17 t1_vibe_dixon_cor_p6_bh_320_iso 00:21	loc_cor_Expiration_for_positioning ✱ 00:11 ep2d diff b50 400 800 tra p3 03:35 T2 options 2d_T2_TSE t2_tse_tra_p2_trig_512 04:02 3d_T2_SPACE_dark vessel t2_space_fs_tra_p2_trig_512 05:11 t1_vibe_dixon_tra_p4_bh_12min_p.i_higher FA 00:17 t1_vibe_dixon_cor_p6_bh_320_iso 00:21
3E		

Figure 3:

Two standard strategies using exhalation and inhalation are provided. **(3A)** Fast planning images acquired with coronal HASTE and transversal HASTE FS scans provide an overview. **(3B)** Optional fast thick-slab HASTE FS scans for T2-weighted MRCP follow. **(3C)** Contrast dynamics; **(3D)** DWI and T2 (2D or 3D) post-contrast; **(3E)** delayed imaging in different planes.

(*) In the inhalation strategy, additional planning images are required to position the free-breathing scans correctly.

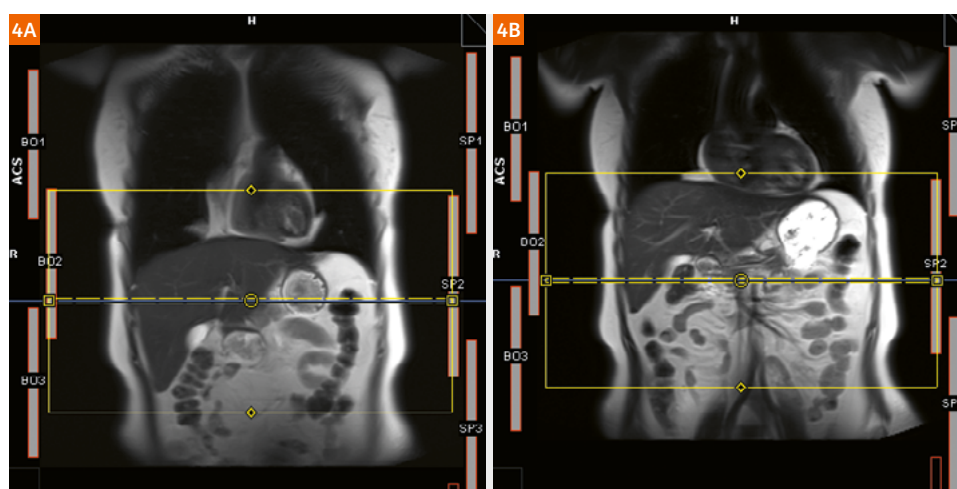


Figure 4:

Inhaled **(4A)** and exhaled **(4B)** coronal planning images illustrate how significantly the organ coverage is affected: While the liver is perfectly centered in the FOV in the inhaled exam, the liver dome risks being cut off in images acquired with triggering, which is typically performed in the exhaled phase. Therefore, an additional localizer is provided to ensure consistent planning of the free-breathing and triggered scans.

on individual preferences, *strongly* T1-weighted in-phase and opposed-phase scans can be acquired with a 2D FLASH technique. This information, however, is also included in the T1-weighted 3D VIBE scans prior to contrast administration and can therefore be skipped if acceptable in the specific clinical setting. Throughout the entire exam, users receive guidance on how to plan

and execute the subsequent scans, such as the optional multiple T2-weighted MRCP scans with a thick-slab 2D HASTE in rotating acquisition (see Figure 5).

For the contrast-enhanced scans, the protocols are prepared so that the system automatically issues breath-hold commands and adheres to typical delays between the different phases. The delay between the phases can

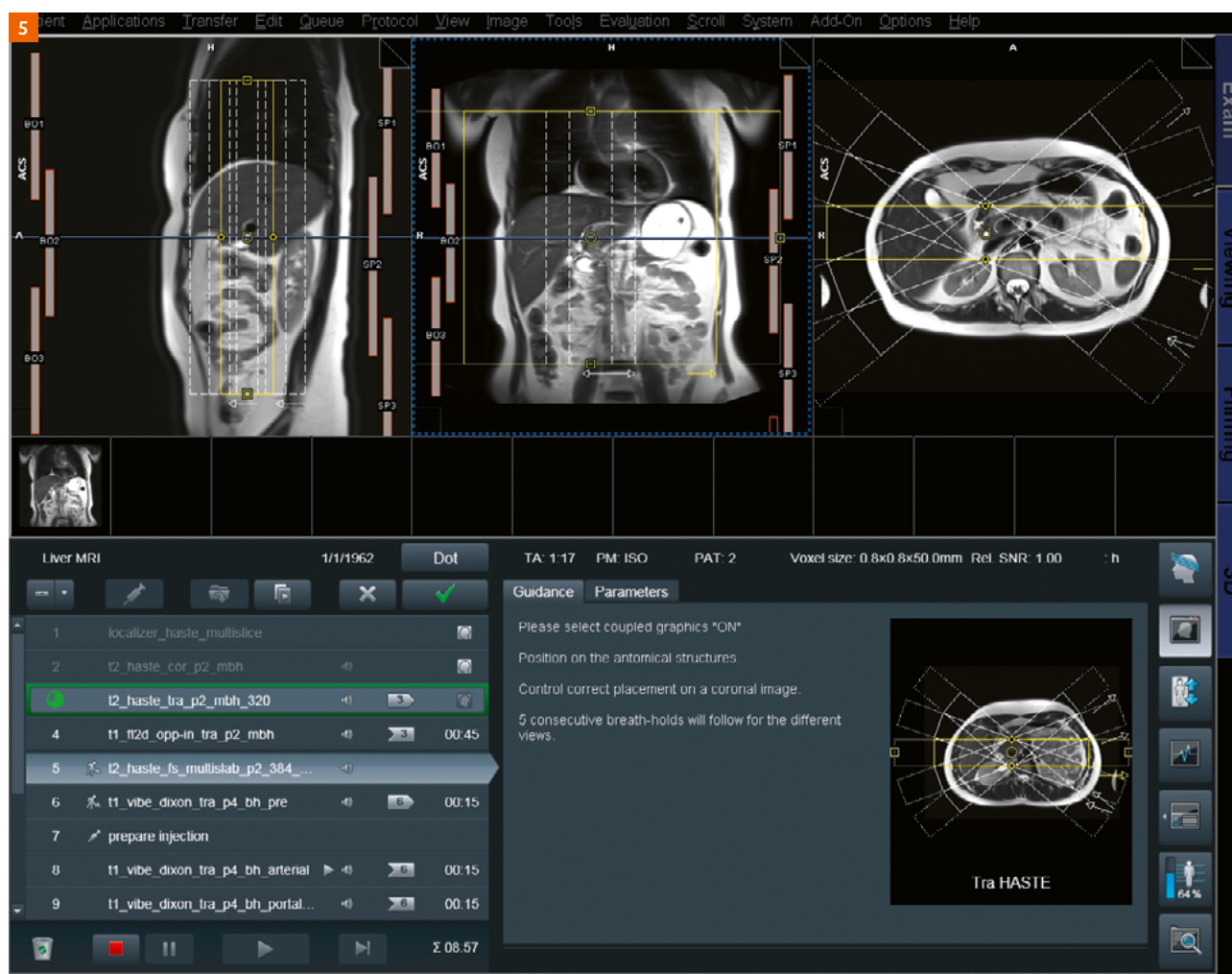


Figure 5:

Overview of the scanner's user interface. Planning images are displayed at the top of the screen, the scan queue is displayed in the lower left, and guidance on how to perform subsequent scans is provided in the "Guidance" window in the lower right of the screen. If "Coupled Graphics = On" is selected, users can intuitively plan five thick-slab MRCP scans with T2 HASTE by positioning the center of the slice stack in an image showing the common bile duct.

be adapted to the institution's individual needs. Important information regarding timing of the contrast-enhanced scans can be found in Figure 6. Depending on local availability and institutional preference, contrast can be delivered via an automated injector.

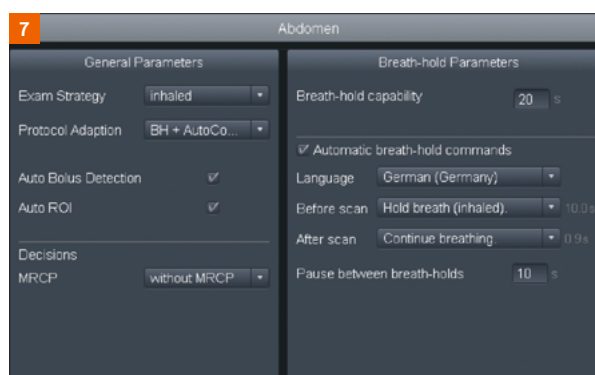
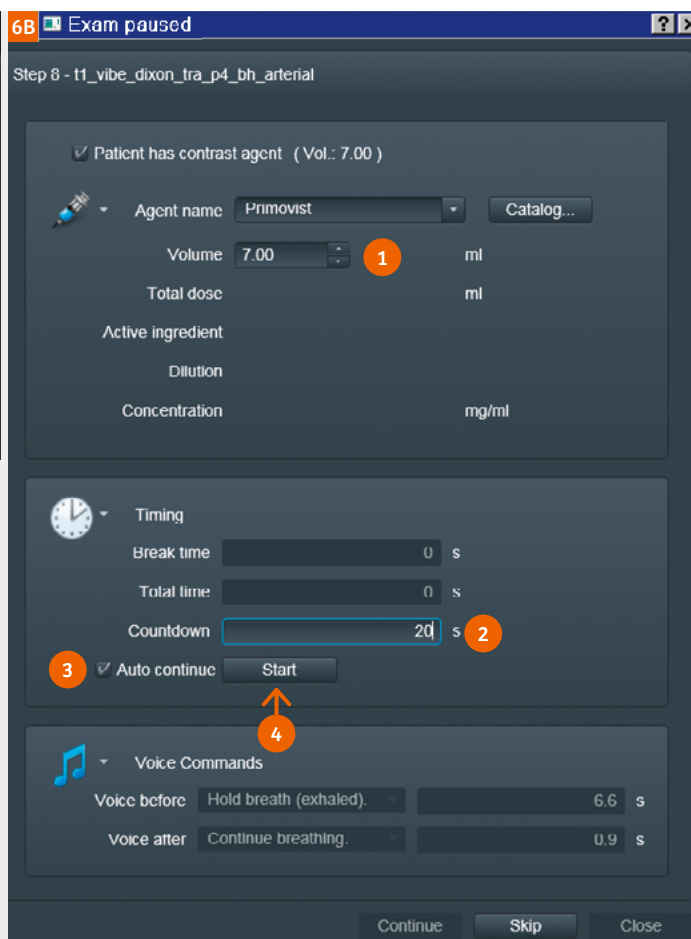
After starting the contrast injection and imaging countdown simultaneously, arterial, portal-venous and delayed phase imaging will be performed automatically with predefined pauses which can be adapted to the institution's own standards. If desired, subtraction images of the different phases can be automatically generated. As proposed by Bayer, the time between the delayed phase and the hepatobiliary phase can be effectively used to acquire high-resolution T2-weighted and diffusion-weighted images in free-breathing. Users can choose

between 2D or 3D acquisition for the T2-weighted scans. The 3D T2-weighted scans also include weak "diffusion" gradients to generate a dark-vessel contrast in the liver, which makes it easier to identify T2-intense lesions.

Approximately 10 to 15 minutes post contrast injection, the hepatobiliary phase scans can be started in non-cirrhotic patients. According to the recommendations in the literature, the flip angle is increased for higher contrast between enhancing normal liver parenchyma and non-enhancing lesions. At the end of the exam, an optional T1-weighted MR cholangiography with a high-resolution FLASH 3D protocol in one breath-hold can be acquired. This scan provides a nice functional overview of the biliary system (post-resection, for example), as Primovist is excreted by 50% via the hepatobiliary system).

**Figure 6:**

(6A) After acquisition of the pre-contrast T1-weighted scans (#6 in the queue), the examination is stopped to prepare the injector and to check the coverage and quality of the pre-contrast scans (#7). If everything is fine, users can proceed to the next step (#8) since the arterial phase imaging will not start yet ("play" symbol in the queue). A dialog box (6B) will open automatically and allow users to define the contrast media and contrast volume (1). In the "Timing" section, users set the delay (2) between contrast administration and start of arterial phase imaging. A typical value is 20 seconds. If "Auto continue" (3) is selected, users can start the countdown by pressing "Start" (4) and administer contrast agent at exactly the same time. In this case, the MR system will automatically count down to zero and will also issue the breath-hold commands in a good time to ensure that the scan starts when it reaches zero. When "Auto Continue" is selected, users should not press "Continue" or "Skip".

**Figure 7:**

Prior to the actual examination, users can tailor the exam to the individual patient characteristics and clinical question, e.g., by setting the maximum breath-hold duration and using Auto Bolus Detection for individualized arterial phase imaging, as recommended by Bayer for imaging with Primovist.

Primovist protocol using Abdomen Dot Engine features³

The Primovist Abdomen Dot Engine strategy follows exactly the same structure and logic as the standard protocols: Coronal and axial HASTE scans, 2D in-phase and opposed-phase FLASH, and optional fast T2-weighted MRCP scans prior to contrast are followed by dynamic contrast-enhanced scans and high-resolution T2-weighted, diffusion-weighted, and hepatobiliary phase imaging. The original, general Abdomen Dot Engine settings with breath-holds during inhalation remained unchanged. If desired, users can change this general approach. Additional features and related advantages of the Abdomen Dot Engine are as follows:

- The exam can be tailored to the patient's individual breath-hold capabilities by simply defining the maximum breath-hold duration at the beginning of the exam or by changing it during the exam. The software automatically adapts related imaging parameters in a consistent way.
- Automated landmark detection in the abdomen (organ box) allows automated adaptation of the field-of-view and number of slices, and correct positioning of the imaging volume in the individual anatomy (see Figure 7).

³ A prerequisite for using this strategy is the local availability of the Abdomen Dot Engine license. TWIST-VIBE and GRASP-VIBE are licensed options and not available for all systems.



- Auto Bolus Detection with ABLE (see Figure 8) precisely adapts the start (respecting also TTC) of the arterial phase scans to the patient's physiology by releasing the scan when contrast agent arrives in the ROI in the descending aorta. The location of the ROI can either be defined by the user or automatically by the software (Auto ROI).
- Encapsulated acquisition is possible for double-echo T2-weighted scans with "normal" (TE = 70 ms) and "very strong" (TE = 430 ms) T2-weighting between venous and delayed scans.
- Automated subtraction of dynamic liver phases with a liver motion correction algorithm (DynaVIBE) ensures

that slices from different breath-holds represent the same anatomical position.

- The system can seamlessly integrate multiple arterial phase images with TWIST-VIBE or free-breathing liver dynamics with GRASP-VIBE from the Abdomen Dot Library.

References

- 1 Bluemke DA, Sahani D, Amendola M, et al. Efficacy and safety of MR imaging with liver-specific contrast agent: U.S. multicenter phase III study. *Radiology*. 2005; 237(1):89–98.
- 2 Huppertz A, Balzer T, Blakeborough A, et al. Improved detection of focal liver lesions at MR imaging: multicenter comparison of gadoxetic acid-enhanced MR images with intraoperative findings. *Radiology*. 2004; 230(1):266–275.
- 3 Rohrer M, Bauer H, Mintonovitch J, Requardt M, Weinmann H-J. Comparison of magnetic properties of MRI contrast media solutions at different magnetic field strengths. *Invest Radiol*. 2005;40:715–724.
- 4 Zech CJ, Grazioli L, Breuer J, et al. Diagnostic performance and description of morphological features of focal nodular hyperplasia in Gd-EOB-DTPA-enhanced liver magnetic resonance imaging: results of a multicenter trial. *Invest Radiol*. 2008;43(7):504–511.
- 5 Kim YK, Kwak HS, Kim CS, Han YM. Detection and characterization of focal hepatic tumors: a comparison of T2-weighted MR images before and after the administration of gadoxetic acid. *J Magn Reson Imaging*. 2009;30(2):437–443.
- 6 Kinner S, Umutlu L, Blex S, et al. Diffusion weighted MR imaging in patients with HCC and liver cirrhosis after administration of different gadolinium contrast agents: is it still reliable? *Eur J Radiol*. 2012;81(4):e625–628.
- 7 van Kessel CS, Veldhuis WB, van den Bosch MA, van Leeuwen MS. MR liver imaging with Gd-EOB-DTPA: a delay time of 10 minutes is sufficient for lesion characterisation. *Eur Radiol*. 2012;22(10):2153–2160.
- 8 Lens E, Gurney-Champion OJ, Tekelenburg DR, et al. Abdominal organ motion during inhalation and exhalation breath-holds: pancreatic motion at different lung volumes compared. *Radiother Oncol*. 2016;121(2):268–275.

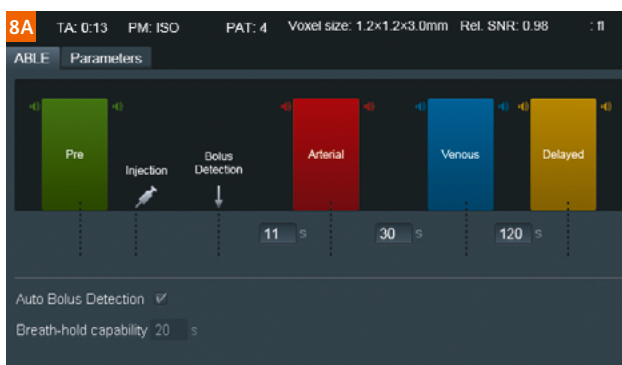


Figure 8:
(8A) The progress of dynamic imaging is intuitively displayed, and it is easy to modify pauses between the different phases. (8B) To perfectly catch the early arterial enhancement in the liver, a ROI is automatically (or manually) placed above the descending aorta. As soon as a signal threshold in this region is exceeded, the subsequent T1-weighted VIBE is released and dynamic phase imaging starts without further user interaction. Automatic breath-hold commands are included. If preferred, the CareBolus scans can also be acquired in axial orientation.

Contact

Gregor Thörmer, Ph.D.
Global Segment Manager MRI in Oncology
Siemens Healthineers
Phone: +49 (0)9131 84-7726
gregor.thoermer@siemens-healthineers.com



Now available:

Optimized Primovist protocols

Download optimized Primovist protocols for 1.5 and 3T systems at:

<https://www.magnetomworld.siemens-healthineers.com/clinical-corner/protocols/body-pelvis/world-primovist-liver-mri-protocol>



Protocol Name	Protocol ID	Protocol Name	Protocol ID
1.5T_1.5T_Primovist_Liver_MRI_Protocol	1.5T_1.5T_Primovist_Liver_MRI_Protocol	3T_3T_Primovist_Liver_MRI_Protocol	3T_3T_Primovist_Liver_MRI_Protocol
1.5T_1.5T_Primovist_Liver_MRI_Protocol	1.5T_1.5T_Primovist_Liver_MRI_Protocol	3T_3T_Primovist_Liver_MRI_Protocol	3T_3T_Primovist_Liver_MRI_Protocol
1.5T_1.5T_Primovist_Liver_MRI_Protocol	1.5T_1.5T_Primovist_Liver_MRI_Protocol	3T_3T_Primovist_Liver_MRI_Protocol	3T_3T_Primovist_Liver_MRI_Protocol
1.5T_1.5T_Primovist_Liver_MRI_Protocol	1.5T_1.5T_Primovist_Liver_MRI_Protocol	3T_3T_Primovist_Liver_MRI_Protocol	3T_3T_Primovist_Liver_MRI_Protocol
1.5T_1.5T_Primovist_Liver_MRI_Protocol	1.5T_1.5T_Primovist_Liver_MRI_Protocol	3T_3T_Primovist_Liver_MRI_Protocol	3T_3T_Primovist_Liver_MRI_Protocol
1.5T_1.5T_Primovist_Liver_MRI_Protocol	1.5T_1.5T_Primovist_Liver_MRI_Protocol	3T_3T_Primovist_Liver_MRI_Protocol	3T_3T_Primovist_Liver_MRI_Protocol
1.5T_1.5T_Primovist_Liver_MRI_Protocol	1.5T_1.5T_Primovist_Liver_MRI_Protocol	3T_3T_Primovist_Liver_MRI_Protocol	3T_3T_Primovist_Liver_MRI_Protocol
1.5T_1.5T_Primovist_Liver_MRI_Protocol	1.5T_1.5T_Primovist_Liver_MRI_Protocol	3T_3T_Primovist_Liver_MRI_Protocol	3T_3T_Primovist_Liver_MRI_Protocol
1.5T_1.5T_Primovist_Liver_MRI_Protocol	1.5T_1.5T_Primovist_Liver_MRI_Protocol	3T_3T_Primovist_Liver_MRI_Protocol	3T_3T_Primovist_Liver_MRI_Protocol



Reduced Stress and Consistent Contrast-enhanced MRI Scans with Precisely Timed, Automated Injection Enabled by MR-Injector Coupling

A Joint Development by Bayer and Siemens Healthineers

Gregor Thoermer¹; Manuela Rick¹; Petra Bildhauer¹; Jens Gühring¹; Dieter Faust¹; Barbara De Napoli²; Ron Barbat³; Sri Shriram³

¹Siemens Healthineers, Magnetic Resonance Imaging, Erlangen, Germany

²Bayer Medical Care B.V., Pharmaceuticals, Maastricht, The Netherlands

³Bayer Healthcare, Pharmaceuticals, Indianola, USA

Introduction

Contrast-enhanced MR imaging procedures, such as MR angiography (MRA) or dynamic contrast-enhanced (DCE) imaging in oncology, require precise timing of contrast injection and MR data acquisition to hit the first pass of contrast agent in the body region or tissue of interest.

If all the required steps are performed carefully and in the right order, MRA and DCE can be performed with high

consistency and reproducibility. However, conducting a test bolus scan alone typically involves user interactions with three different monitors and devices (see Table 1). In daily clinical practice, typically, MRA is a one-per-day examination and consequently many technologists do not routinely perform such exams. Also, calculating the delay time between injection and scanning, considering

	Conventional workflow	Enhanced ISI workflow
Preparation	1. Localizer imaging to gain anatomical overview 2. Vessel scout to gain overview where big vessels are located	
Test Bolus	3. Plan and prepare test bolus examination 4. Set-up test bolus protocol & Arm the injector 5. Prepare patient for the injection 6. Arm the scan on the MR console (prescans are performed)	
	7. Start contrast agent injection on the injector console 8. Start MR acquisition at the same time with second hand	7. precisely synchronized start of injection and scan with one click
Time Delay (TD) Calculation	9. Open mean-curve application and load test bolus data 10. Derive time-to-arrival 11. calculate TD based on time-to-center and formula	8. Select supplying vessel in pre-loaded test bolus images with one click for automated calculation of TD
MRA	12. (9.) Plan and scan pre-contrast T1w 3D protocol 13. (10.) Set up injection protocol & arm injector 14. (11.) Wait-for-user-to-start dialogue (@scanner) to enter contrast agent and volume applied 15. (12.) Arm the post-contrast scan (prescans are performed) 16. (13.) Prepare patient for second injection and breath-hold exam	
	17. Start contrast agent injection on the injector console 18. Monitor time elapsed 19. Apply breath-hold command 3–4 seconds before intended start of scanning (TD) 20. Start the scan at TD 21. "Continue breathing"	14. One click to: – Inject contrast – Apply timed Auto-voice command before TD – Auto-start scan at TD – "Continue breathing" command

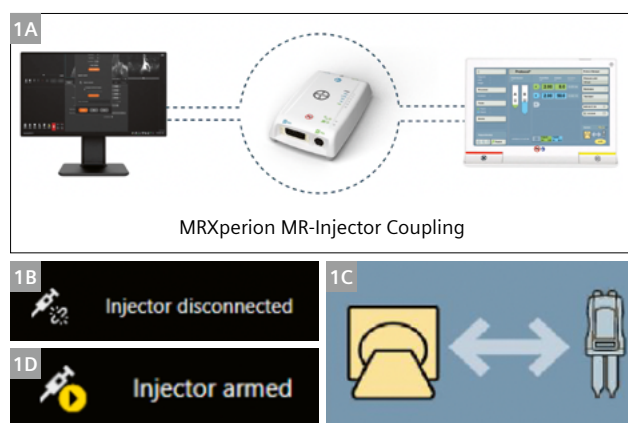
Table 1: Comparison between conventional workflow and enhanced ISI workflow.

when the center of k -space is acquired, is often regarded as a challenge. Along with the lack of routine practice, this can cause uncertainty and errors in the workflow that may result in imperfect timing. If the bolus is missed, the MRA may show venous enhancement or improper arterial filling, and in DCE the lesion-to-background contrast will not be optimal. If an examination is of reduced quality or non-diagnostic, this may lead to repeated administration of contrast, delayed diagnosis, additional costs, and tensions between radiologist and technologist.

Imaging System Interface (ISI) for MR-Injector Coupling

Bayer Healthcare and Siemens Healthineers have jointly developed a hardware and software interface (ISI – Imaging System Interface) enabling active coupling between the Medrad® MRXperion MR Injection System (in short, “injector”) and the MR scanner (Fig. 1)¹. It establishes a direct reliable connection between the MR scanner and the injector control system, allowing a technologist at the MR operator console to release injections remotely, which helps to overcome the aforementioned challenges. Combined with intuitive guidance provided by the Angio Dot Engine or the Abdomen Dot Engine, this provides a self-contained, intuitive workflow for high-quality and consistent contrast-enhanced procedures.

¹Work in progress: the application is currently under development and is not for sale in the U.S. and in other countries. Its future availability cannot be ensured. Note: This feature may not be available in all regions/countries at the time of publication.



1 (1A) Schematic view of scanner-injector coupling via the ISI box. On the MR console, the status of the scanner-injector coupling is displayed as: not connected (1B), connected or armed. After confirming the injection protocol (“Lock”) and ensuring that tubes and syringes are cleared of air (“Arm”) on the injector console (1C) the status on the MR console changes to “Injector armed” (1D). From this point on, it is possible to initiate the contrast application directly from the MR console, seamlessly embedded in different workflows.

Conventional versus enhanced ISI Workflow

An MRA of the carotids is used in Table 1 to illustrate the enhanced ISI workflow in comparison with a conventional examination. The related advantages can be generalized to various other CE examinations.

As shown in Table 1, the ISI workflow is predominantly similar to the conventional workflow, but decisive and critical steps are assisted and the user interaction is reduced to the essentials. If the coupling between the injector and the MR scanner is established as described in Figure 1, both the scan and the injection can be initiated with one single mouse click in the MR scanner user interface (Fig. 2). Among other things, this enables precise synchronization between contrast injection and start of the test bolus MR sequence for the accurate calculation of contrast arrival in the target region.

Exam Paused ? x

☐ Patient has Contrast Agent (Vol. 0.00)

Agent Name Catalog...

Volume ml

Total Dose ml

Active Ingredient

Dilution

Concentration mg/ml

Timing

Injector Control

Injector armed

☒ Use Injector with Auto Continue

☐ and Countdown (see Timing)

Start Injection

Voice Commands

Continue **Skip** **Close**

2 Pause dialogue before first contrast injection. Injector and MR are coupled via ISI, the injector is armed. Selecting the tick box “Use Injector with Auto Continue” will facilitate a synchronized release of contrast injection and scan whenever the user presses “Start Injection”.



- 3** Interaction dialogue of the Angio Dot Engine after the test bolus measurement. After selecting a feeding artery in test bolus images, the contrast enhancement curve in the respective ROI is displayed as a red curve. Optionally it is also possible to display the contrast dynamics in a vein to make sure that the k -space center is acquired before the venous enhancement is pronounced. The dialogue box intuitively visualizes when and how the post-contrast scan will be performed, when the breath-hold commands will be applied and when the center of k -space will be acquired. The experienced user may always change the settings.

Within the Angio Dot Engine workflow (Fig. 3), the user is also guided and assisted in deriving the patient-specific delay time for MRA. The acquired test bolus datasets are automatically pre-loaded and the user is only required to select a feeding artery in the images. The software will then automatically derive when the peak of enhancement is reached, and by accounting for specific parameters, such as time-to-center of k -space, the optimal delay time between injection and start of the post-contrast scan will be calculated.

With the ISI workflow application of contrast and start of measurement are synchronized, so the user has to press just one button, "Start Injection", instead of manually

injecting contrast on the injector console while giving breath-hold commands to the patient in a timely fashion via the Patient Intercom, and finally starting the actual MR data acquisition manually after the derived delay time on a third device – the MR scanner console. As shown in Figure 4, the automatically derived delay time is prepopulated. By choosing "Use Injector with Auto Continue" and "Countdown" in the acquisition step of the post-contrast images, the scanner software will not only automatically initiate the contrast but start image acquisition at the right time. The required breath-hold commands will also be played exactly when needed.



Summary

In a conventional setting, the technologist is required to constantly plan, monitor, and time the various steps on the injector and scanner workstations for contrast-enhanced procedures – resulting in reduced efficiency, high stress, and potentially suboptimal image quality.

The MR-Injector coupling via ISI is a software and hardware solution that simplifies synchronized contrast injection and scanning by guiding the user through an intuitive workflow, with clicks and interactions reduced to the essentials. With consistent and reproducible studies, this helps to save time, improve operational efficiency, and reduce stress.

Furthermore, the solution is designed to support scenarios such as remotely assisted scans with the *syngo* Virtual Cockpit, where an expert controls the scanner virtually from a remote location. This can help to transform care delivery by providing advanced contrast-enhanced imaging services in remote areas, instead of requiring patients to travel to distant, centralized expert medical centers.

Acknowledgments

The authors would like to thank Sharon Standish, Sean Berecek and William Hohn, and the extended Bayer team (Bayer U.S. LLC, Pharmaceuticals, Indianola, PA, USA) for their valuable support.

- 4 Wait-for-user-to-start dialogue before main contrast injection. Volume and type of contrast agent can be specified. In the "Timing" section, the delay time between injection and start of image acquisition (see Figure 3) is already pre-populated. The section "Injector Control" shows that the injector is armed and that the protocol will be performed with automated countdown and automated start. As soon as "Start injection" is pressed, the contrast injection is initiated, the countdown starts, and 8.9 seconds before "zero" (= start of the imaging sequence) the voice command is played.

Contact

Gregor Thörmer, Ph.D.
Global Segment Manager
MRI in Oncology
Siemens Healthineers
Tel.: +49 (0)9131 84-7726
gregor.thoermer@siemens-healthineers.com



Exam Paused

☒ Patient has Contrast Agent (Vol. 0.00)

Agent Name

Volume

0.00 ml

Total Dose

Active Ingredient

Dilution

Concentration

mg/ml

Timing

Break time

0 s

Total Time

0 s

Countdown

27 s

☒ Auto Continue

Start Countdown

Injector Control

Injector armed

☒ Use Injector with Auto Continue

☒ and Countdown (see Timing)

Start Injection

Voice Commands

Before Scan	Hold breath (inhaled).	8.9 s
After Scan	Continue breathing.	2.7 s

Continue

Skip

Close



New Advances in Radiomics of Liver Imaging

Roberto Cannella¹, Tommaso Vincenzo Bartolotta^{1,2}

¹Section of Radiology – BiND, University Hospital “Paolo Giaccone”, Palermo, Italy

²Department of Radiology, Fondazione Istituto Giuseppe Giglio, Ct.da Pietrapollastra, Cefalù (Palermo), Italy

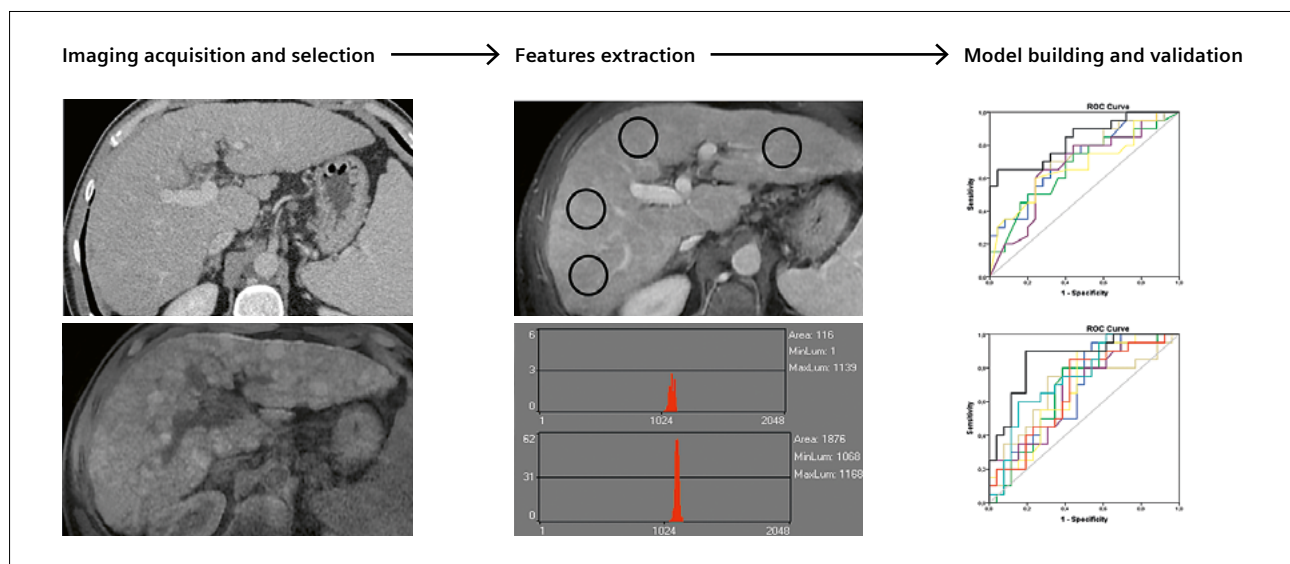
Introduction

Interpretation of liver imaging studies remains challenging in clinical practice due to the complex presentation of chronic liver disease and the presence of multiple focal liver lesions arising in normal and cirrhotic liver with overlap in imaging appearance. Radiomics is currently emerging as a new promising tool for quantitative analysis of liver imaging studies that could potentially increase diagnostic accuracy in the assessment of focal liver lesions, predict treatment response and prognosis after loco-regional or systemic therapies, and stratify the risk of advanced fibrosis and cirrhosis in patients with chronic liver disease [1].

Radiomics allows to extract a large amount of mathematical data through the analysis of the distribution and relationships of pixel densities/intensities within a defined region of interest, providing additional quantitative information from medical images that cannot be evaluated by human eyes [2]. These large amounts of quantitative data can be combined with patients' clinical characteristics, laboratory markers, histopathological parameters, or

genetic data in order to provide predictive models that will help guide physicians to the most appropriate form of management [3]. Radiomics can be applied to any type of imaging study, including ultrasound, CT, MRI, and PET/CT, but most liver studies are currently based on CT or MRI examinations [4]. Although multiple experimental studies have shown promising results from radiomics, with excellent performance for diagnostic, prognostic, and predictive applications in liver imaging, there are several challenges for the adoption of radiomics in clinical practice. Differences in image acquisition, features extraction, and radiomics software pose challenges for the repeatability or application of radiomics models in large populations [3].

In this paper, we aim to discuss the basis of the radiomics workflow and review the new advances and current applications of radiomics in liver imaging, with an emphasis on the current knowledge about radiomics applications in the field of chronic liver disease and focal liver lesions.



1 Schematic of radiomics workflow.



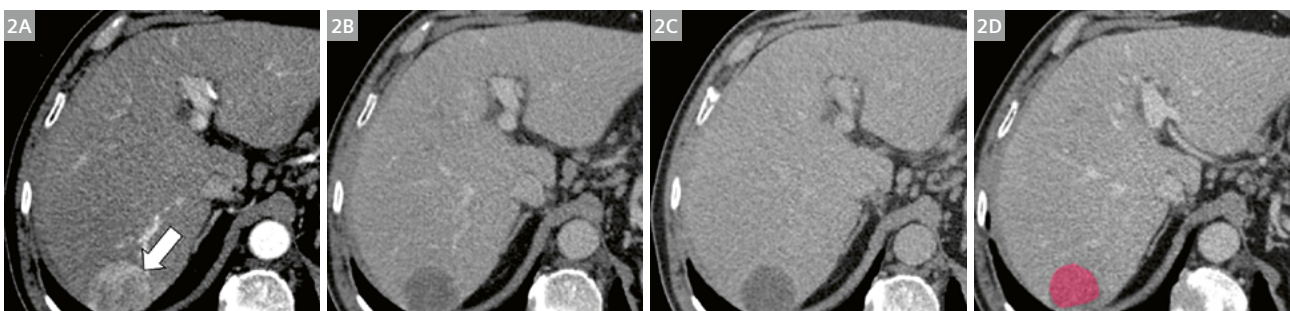
The radiomics workflow

Radiomics analysis is based on a multistep process that includes image acquisition, lesion segmentation, features extraction, features selection and reduction, predictive model building, final validation, and clinical interpretation of the results (Fig. 1) [4–7]. Acquisition of radiological imaging studies is one of the most important steps for radiomics, since scanning and technical parameters are known to influence the reproducibility of radiomics features. In particular, the reconstruction algorithm and slice thickness have an impact on the reproducibility of radiomics features on contrast-enhanced CT images [8–10]. Differences in acquisition protocols complicate the retrospective evaluation of CT or MRI studies acquired with different scanners [11]. It is also important to select the optimal phase/sequence for image analysis. Pre-contrast images are not affected by the contrast administration, but the segmentation may be not feasible if the lesion cannot be distinguished from the background hepatic parenchyma. However, pre-contrast images may provide more reliable assessment of the liver parenchyma in patients with chronic liver disease. Contrast-enhanced images may provide better lesion visualization, but the type, timing, and amount of contrast agent can be additional confounding factors, especially for images acquired in the arterial phase.

Segmentation can be performed manually by experienced radiologists using semi-automatic, or automatic software [11]. Manual segmentation is currently the gold standard in most radiomics studies, but it is often time consuming and is prone to intra- and inter-reader variability [4, 6, 12]. Semi-automatic or automatic software can provide more rapid and reproducible results, but they are prone to errors in cases of imaging artifacts, or unexpected liver anatomy or lesions. When analyzing focal liver lesions, the segmentation is usually performed by drawing an ROI within the tumor margins (Fig. 2). The ROI can be positioned on a single slice (2D ROI) on the largest tumor cross section, or it can include the whole lesion (3D ROI) [7]. When assessing diffuse liver disease, the

segmentation can be performed using a single ROI with fixed diameters positioned on a specific hepatic segment (usually in the right lobe) in a single slice and not including large hepatic vessels or focal live lesions; using multiple ROIs with fixed diameters on different hepatic segments or different levels; or using ROIs that include the whole liver parenchyma or specific segments, usually at the level of the porta hepatis. Although 3D and whole-liver segmentations can capture more tissue heterogeneity, the clinical advantage remains debatable, since studies have demonstrated that single-slice analysis is often sufficient for the evaluation of chronic liver disease and focal lesions, and more practical for the radiological workflow.

Several in-house or commercially available radiomics research software programs allow users to extract a large number of radiomics features. Radiomics features are usually classified as first-, second-, or third-order features [4]. First-order features are obtained from the analysis of the gray-level histogram within a defined ROI, without considering spatial relationships between pixels. The most common histogram-based features include mean (average of the pixels within the ROI), standard deviation (dispersion from the mean), skewness (asymmetry of the histogram), kurtosis (peakedness/flatness of the histogram), and entropy (image irregularity or complexity) [5]. Second-order texture features consider the spatial relationship between pixels and most commonly include the gray-level co-occurrence matrix (GLCM), which quantifies the arrangements of pairs of pixels with the same values in a specific direction, and the gray-level run length matrix (GLRLM), which quantifies consecutive pixels with the same intensity in a specific direction. Third-order or higher order features evaluate spatial relationships between three or more pixels using statistical methods after applying filters or mathematical transforms. These features include fractal analysis, wavelet transforms, and Laplacian transforms of Gaussian-filtered images. Due to the large number of extracted parameters, a features reduction should be performed in order to exclude features that are not reproducible or redundant, and to avoid overfitting problems [8].



2 A 76-year-old man with hepatitis C-related cirrhosis and hepatocellular carcinoma: Contrast-enhanced CT imaging shows a 4 cm liver lesion with arterial phase hyperenhancement (2A, arrow), and washout in portal venous (2B) and delayed (2C) phases. Example of lesion segmentation was performed on portal venous phase (2D).



Final radiomics models should be tailored to validate the accuracy of uncorrelated features according to the specific outcome. The choice of statistical methods depends on multiple factors, such as evaluation of primary outcome, number of features, and number of analyzed lesions. Validation in an independent or external patient cohort is necessary in order to test the real performance of radiomics [12].

Radiomics in chronic liver disease

Chronic liver disease covers a wide spectrum of liver pathologies, the incidence of which has been increasing in recent years. The most common etiologies of chronic liver disease include chronic viral hepatitis (primarily hepatitis B and C), alcoholic hepatitis, and nonalcoholic fatty liver disease (NAFLD). These may evolve into advanced fibrosis and cirrhosis, with possible complications such as portal hypertension, decompensated hepatic failure, and development of hepatocellular carcinoma. In particular, the presence of significant and advanced fibrosis has been reported as an independent predictor of mortality caused by chronic liver disease [13].

Although liver biopsy is considered the reference standard for the diagnosis and staging of fibrosis in patients with chronic liver disease, it has known complications such as pain, hemorrhage, and infections. It is also prone to sampling errors due to the heterogeneous distribution of fibrosis in the hepatic parenchyma, and to inter- and intra-reader variability. Several imaging-based noninvasive methods have been developed for assessing hepatic fibrosis in patients with chronic liver disease. They include shear wave elastography, MR elastography, diffusion-weighted imaging, and liver surface nodularity [14]. Recently, radiomics has been applied to liver imaging for the noninvasive assessment of hepatic fibrosis, with several studies reporting a fair-to-good diagnostic performance for the detection of advanced fibrosis or cirrhosis [15–23]. Most of these studies applied radiomics on CT or MR imaging, using pre-contrast or portal venous phase images. Overall, similar diagnostic performance was observed regardless of the etiology of the chronic liver disease. However, it should be noted that most current radiomics studies have evaluated patients with chronic viral hepatitis B or C. Nonalcoholic fatty liver disease, which is becoming the major cause of chronic liver disease and cirrhosis in Western countries, was investigated by only a minority of studies [15, 16, 18].

In the initial experience of Lubner et al. [18] quantitative texture analysis was performed on contrast-enhanced CT images from 289 patients with different etiologies of chronic liver disease, with a fair-to-good performance in discriminating between different stages of fibrosis. In a subsequent study, Lubner et al. [19] enrolled a cohort of

556 patients that included both healthy subjects and patients with hepatitis C and various degrees of hepatic fibrosis. Texture features were extracted by drawing an ROI that covered the entire liver. A good diagnostic performance was achieved for detecting significant and advanced fibrosis of models incorporating multiple features. A multiparametric approach that combines radiomics features and other CT-based methods for staging hepatic fibrosis has demonstrated excellent results in the stratification of fibrosis degree, improving the performance of individual parameters [21]. A recent study of MRI [15] investigated the performance of texture analysis in NAFLD patients, reporting a fair accuracy of entropy and standard deviation for the diagnosis of significant and advanced fibrosis, based on pre-contrast sequences.

Compared to other noninvasive imaging-based methods for assessment of hepatic fibrosis, the major advantage of radiomics and texture analysis is that they can also be applied retrospectively to extract additional data from images that have already been acquired, and can potentially be performed with any type of imaging study. However, a lack of standardization, variability in radiomics features and available software, and vulnerability to image acquisition parameters still pose significant challenges for applying radiomics in routine clinical practice. Further studies should focus on validation in multicenter cohorts, and on comparison with other non-invasive techniques for fibrosis evaluation.

Radiomics in focal liver lesions

Focal liver lesions include a wide spectrum of benign and malignant lesions that can occur in both normal liver and in cirrhosis. The differential diagnosis of focal liver lesions should consider the background liver parenchyma, presence of risk factors, clinical parameters, and imaging appearance on multiphasic contrast-enhanced studies. Although some lesions may demonstrate typical enhancement patterns on CT or MR images, the differential diagnosis in clinical practice remains challenging, and a histopathological confirmation is often required to reach the final diagnosis.

In patients without history of chronic liver disease or extrahepatic malignancies, focal liver lesions are most commonly benign, and the differential diagnosis includes hemangioma, focal nodular hyperplasia (FNH), and hepatocellular adenoma (HCA). Differentiating between FNH and HCA is challenging due to the overlap in the imaging appearance and the presence of multiple subtypes of HCA [24]. While FNHs are indolent lesions, HCAs carry a risk of complications such as hemorrhage and malignant transformation. Lesion biopsy is therefore often required to reach the definitive diagnosis [24]. Recent studies have demonstrated that the application of radiomics could help



increase the diagnostic performance for the differential diagnosis between FNH and HCA, with significant improvements compared to conventional qualitative evaluations [25, 26]. In particular, a retrospective study [26] reported that texture-based parameters obtained from gadoxetate disodium-enhanced MRI on T2-weighted and hepatobiliary phase imaging can distinguish FNH from HCA in up to 96% of cases.

In patients with underlying cirrhosis or chronic liver disease, hepatocellular carcinoma (HCC) represents the most common primary malignancy, accounting for up to 90% of all liver cancers [27, 28]. Several studies have adopted a radiomics approach to quantify lesion heterogeneity in HCC. In particular, recent studies have explored the potential of radiomics for preoperative assessments of HCC with prediction of recurrence-free survival and overall survival after curative resection, recurrence following liver transplantation, correlation with histopathological markers of HCC aggressiveness (i.e., microvascular invasion), and evaluation of treatment response in patients undergoing locoregional therapies or systemic therapies in cases with advanced tumors [29–40]. Anh et al. [31] found that imaging findings and texture-based features on preoperative gadoxetate disodium-enhanced MRI were helpful for predicting early recurrence after curative resections in patients with single HCC. Feng et al. [35] developed a preoperative radiomics model for prediction of microvascular invasion based on gadoxetate disodium-enhanced MRI. Park et al. [38] investigated the role of CT-based texture analysis in the prediction of therapeutic response in HCC after transcatheter arterial chemoembolization.

Conclusions

Radiomics is emerging as a promising tool with large potential for the assessment of chronic liver disease and focal liver lesions, providing excellent diagnostic performance for multiple applications in research studies. Future implementation of radiomics models should focus on addressing current limitations that pose challenges for its application in everyday clinical practice.

References

- Lubner MG, Smith AD, Sandrasegaran K, Sahani DV, Pickhardt PJ. CT Texture Analysis: Definitions, Applications, Biologic Correlates, and Challenges. *Radiographics*. 2017;37(5):1483-1503.
- Vernuccio F, Cannella R, Comelli A, Salvaggio G, Lagalla R, Midiri M. [Radiomics and artificial intelligence: new frontiers in medicine.]. *Recenti Prog Med*. 2020;111(3):130-135.
- Gillies RJ, Kinahan PE, Hricak H. Radiomics: Images Are More than Pictures, They Are Data. *Radiology*. 2016;278(2):563-577.
- Lewis S, Hectors S, Taouli B. Radiomics of hepatocellular carcinoma. *Abdom Radiol (NY)*. 2020;doi:10.1007/s00261-019-02378-5.
- Miranda Magalhaes Santos JM, Clemente Oliveira B, Araujo-Filho JAB, Assuncao-Jr AN, de M Machado FA, Carlos Tavares Rocha C, et al. State-of-the-art in radiomics of hepatocellular carcinoma: a review of basic principles, applications, and limitations. *Abdom Radiol (NY)*. 2020;45(2):342-353.
- Varghese BA, Cen SY, Hwang DH, Duddalwar VA. Texture Analysis of Imaging: What Radiologists Need to Know. *AJR Am J Roentgenol*. 2019;212(3):520-528.
- Cannella R, La Grutta L, Midiri M, Bartolotta TV. New advances in radiomics of gastrointestinal stromal tumors. *World J Gastroenterol* 2020;26(32):4729-4738
- Berenguer R, Pastor-Juan MDR, Canales-Vázquez J, Castro-García M, Villas MV, Mansilla Legorburo F, et al. Radiomics of CT Features May Be Nonreproducible and Redundant: Influence of CT Acquisition Parameters. *Radiology*. 2018;288(2):407-415.
- Ahn SJ, Kim JH, Lee SM, Park SJ, Han JK. CT reconstruction algorithms affect histogram and texture analysis: evidence for liver parenchyma, focal solid liver lesions, and renal cysts. *Eur Radiol*. 2019;29(8):4008-4015.
- Meyer M, Ronald J, Vernuccio F, Nelson RC, Ramirez-Giraldo JC, Solomon J, et al. Reproducibility of CT Radiomic Features within the Same Patient: Influence of Radiation Dose and CT Reconstruction Settings. *Radiology*. 2019;293(3):583-591.
- Koçak B, Durmaz EŞ, Ateş E, Kılıçkesmez Ö. Radiomics with artificial intelligence: a practical guide for beginners. *Diagn Interv Radiol*. 2019;25(6):485-495.
- Wakabayashi T, Ouhmich F, Gonzalez-Cabrera C, Felli E, Saviano A, Agnus V, et al. Radiomics in hepatocellular carcinoma: a quantitative review. *Hepatol Int*. 2019;13(5):546-559.
- Chalasani N, Younossi Z, Lavine JE, Charlton M, Cusi K, Rinella M, et al. The diagnosis and management of nonalcoholic fatty liver disease: Practice guidance from the American Association for the Study of Liver Diseases. *Hepatology*. 2018;67(1):328-357.
- Petitclerc L, Gilbert G, Nguyen BN, Tang A. Liver Fibrosis Quantification by Magnetic Resonance Imaging. *Top Magn Reson Imaging*. 2017;26(6):229-241.
- Cannella R, Borhani AA, Tublin M, Behari J, Furlan A. Diagnostic value of MR-based texture analysis for the assessment of hepatic fibrosis in patients with nonalcoholic fatty liver disease (NAFLD). *Abdom Radiol (NY)*. 2019;44(5):1816-1824.
- Daginawala N, Li B, Buch K, Yu H, Tischler B, Qureshi MM, et al. Using texture analyses of contrast enhanced CT to assess hepatic fibrosis. *Eur J Radiol*. 2016;85(3):511-517.
- House MJ, Bangma SJ, Thomas M, Gan EK, Ayonrinde OT, Adams LA, et al. Texture-based classification of liver fibrosis using MRI. *J Magn Reson Imaging*. 2015;41(2):322-328.
- Lubner MG, Malecki K, Kloke J, Ganeshan B, Pickhardt PJ. Texture analysis of the liver at MDCT for assessing hepatic fibrosis. *Abdom Radiol (NY)*. 2017;42(8):2069-2078.
- Lubner MG, Jones D, Kloke J, Said A, Pickhardt PJ. CT texture analysis of the liver for assessing hepatic fibrosis in patients with hepatitis C virus. *Br J Radiol*. 2019;92(1093):20180153. Epub 2018 Oct 11.
- Park HJ, Lee SS, Park B, Yun J, Sung YS, Shim WH, et al. Radiomics Analysis of Gadoxetic Acid-enhanced MRI for Staging Liver Fibrosis. *Radiology*. 2019;290(2):380-387.
- Pickhardt PJ, Graffy PM, Said A, Jones D, Welsh B, Zea R, et al. Multiparametric CT for Noninvasive Staging of Hepatitis C Virus-Related Liver Fibrosis: Correlation With the Histopathologic Fibrosis Score. *AJR Am J Roentgenol*. 2019;212(3):547-553.



- 22 Wu Z, Matsui O, Kitao A, Kozaka K, Koda W, Kobayashi S, et al. Hepatitis C related chronic liver cirrhosis: feasibility of texture analysis of MR images for classification of fibrosis stage and necroinflammatory activity grade. *PLoS One*. 2015;10(3):e0118297.
- 23 Zhang X, Gao X, Liu BJ, Ma K, Yan W, Liling L, et al. Effective staging of fibrosis by the selected texture features of liver: Which one is better, CT or MR imaging? *Comput Med Imaging Graph*. 2015;2:227-236.
- 24 Nault JC, Couchy G, Balabaud C, Morcrette G, Caruso S, Blanc JF, et al. Molecular Classification of Hepatocellular Adenoma Associates With Risk Factors, Bleeding, and Malignant Transformation. *Gastroenterology*. 2017;152(4):880-894.e6.
- 25 Cannella R, Borhani AA, Minervini MI, Tsung A, Furlan A. Evaluation of texture analysis for the differential diagnosis of focal nodular hyperplasia from hepatocellular adenoma on contrast-enhanced CT images. *Abdom Radiol (NY)*. 2019;44(4):1323-1330.
- 26 Cannella R, Rangaswamy B, Minervini MI, Borhani AA, Tsung A, Furlan A. Value of Texture Analysis on Gadoteric Acid-enhanced MRI for Differentiating Hepatocellular Adenoma from Focal Nodular Hyperplasia. *AJR Am J Roentgenol*. 2019;212(3):538-546.
- 27 European Association for the Study of the Liver. EASL Clinical Practice Guidelines: Management of hepatocellular carcinoma. *J Hepatol*. 2018;69(1):182-236.
- 28 Marrero JA, Kulik LM, Sirlin CB, Zhu AX, Finn RS, Abecassis MM, et al. Diagnosis, Staging, and Management of Hepatocellular Carcinoma: 2018 Practice Guidance by the American Association for the Study of Liver Diseases. *Hepatology*. 2018;68(2):723-750.
- 29 Chen S, Zhu Y, Liu Z, Liang C. Texture analysis of baseline multiphasic hepatic computed tomography images for the prognosis of single hepatocellular carcinoma after hepatectomy: A retrospective pilot study. *Eur J Radiol*. 2017;90:198-204.
- 30 Zhou Y, He L, Huang Y, Chen S, Wu P, Ye W, et al. CT-based radiomics signature: a potential biomarker for preoperative prediction of early recurrence in hepatocellular carcinoma. *Abdom Radiol (NY)*. 2017;42(6):1695-1704.
- 31 Ahn SJ, Kim JH, Park SJ, Kim ST, Han JK. Hepatocellular carcinoma: preoperative gadoxetic acid-enhanced MR imaging can predict early recurrence after curative resection using image features and texture analysis. *Abdom Radiol (NY)*. 2019;44(2):539-548.
- 32 Brenet Defour L, Mulé S, Tenenhaus A, Piardi T, Sommacale D, Hoeffel C, et al. Hepatocellular carcinoma: CT texture analysis as a predictor of survival after surgical resection. *Eur Radiol*. 2019;29(3):1231-1239.
- 33 Oh J, Lee JM, Park J, Joo I, Yoon JH, Lee DH, et al. Hepatocellular Carcinoma: Texture Analysis of Preoperative Computed Tomography Images Can Provide Markers of Tumor Grade and Disease-Free Survival. *Korean J Radiol*. 2019;20(4):569-579.
- 34 Ning P, Gao F, Hai J, Wu M, Chen J, Zhu S, et al. Application of CT radiomics in prediction of early recurrence in hepatocellular carcinoma. *Abdom Radiol (NY)*. 2020;45(1):64-72.
- 35 Feng ST, Jia Y, Liao B, Huang B, Zhou Q, Li X, et al. Preoperative prediction of microvascular invasion in hepatocellular cancer: a radiomics model using Gd-EOB-DTPA-enhanced MRI. *Eur Radiol*. 2019;29(9):4648-4659.
- 36 Xu X, Zhang HL, Liu QP, Sun SW, Zhang J, Zhu FP, et al. Radiomic analysis of contrast-enhanced CT predicts microvascular invasion and outcome in hepatocellular carcinoma. *J Hepatol*. 2019;70(6):1133-1144.
- 37 Wilson GC, Cannella R, Fiorentini G, Shen C, Borhani A, Furlan A, et al. Texture analysis on preoperative contrast-enhanced magnetic resonance imaging identifies microvascular invasion in hepatocellular carcinoma. *HPB (Oxford)*. 2020;S1365-182X(20)30079-4.
- 38 Park HJ, Kim JH, Choi SY, Lee ES, Park SJ, Byun JY, et al. Prediction of Therapeutic Response of Hepatocellular Carcinoma to Transcatheter Arterial Chemoembolization Based on Pretherapeutic Dynamic CT and Textural Findings. *AJR Am J Roentgenol*. 2017;209(4):W211-W220.
- 39 Yu JY, Zhang HP, Tang ZY, Zhou J, He XJ, Liu YY, et al. Value of texture analysis based on enhanced MRI for predicting an early therapeutic response to transcatheter arterial chemoembolisation combined with high-intensity focused ultrasound treatment in hepatocellular carcinoma. *Clin Radiol*. 2018;73(8):758.e9-758.e18.
- 40 Mulé S, Thieffin G, Costentin C, Durot C, Rahmouni A, Luciani A, et al. Advanced Hepatocellular Carcinoma: Pretreatment Contrast-enhanced CT Texture Parameters as Predictive Biomarkers of Survival in Patients Treated with Sorafenib. *Radiology*. 2018;288(2):445-455.

Contact

Professor Tommaso Vincenzo Bartolotta, M.D., Ph.D.
Department of Radiology
Fondazione Istituto Giuseppe Giglio
Ct.da Pietrapollastra
Via Pisciotto,
90015 Cefalù (Palermo)
Italy
tommasovincenzo.bartolotta@unipa.it



Roberto Cannella, M.D.
Section of Radiology – BiND
University Hospital “Paolo Giaccone”
Via del Vespro 129
90127 Palermo
Italy
rob.cannella89@gmail.com





4D-MRI for Treatment Planning of Liver Tumors

Jessica Scholey¹; Horatio Thomas¹; Xin Miao²; Dianne Ferguson³; Mary Feng¹

¹Department of Radiation Oncology, University of California, San Francisco, CA, USA

²Siemens Medical Solutions USA Inc., Boston, MA, USA

³Department of Radiation Oncology, Brigham and Women's Hospital, Dana Farber Cancer Institute and Harvard Medical School, Boston, MA, USA

Introduction

Stereotactic body radiation therapy (SBRT) is increasingly being used to manage primary and metastatic liver tumors [1–3]. Accurately accounting for respiratory motion is imperative when targeting liver tumors with radiation. Strategies such as abdominal compression and breath-hold have been used to reduce tumor motion, though many patients cannot tolerate these strategies due to coexisting comorbidities and poor performance status. For these patients, four-dimensional computed tomography (4D-CT) is used to estimate tumor motion throughout the respiratory cycle and generate internal target volumes (ITVs) for radiotherapy treatment planning. However, delineating liver tumors on 4D-CT is very challenging because of its inherent poor soft tissue contrast. These tumors can only be visualized using intravenous contrast, which is eliminated from the liver quickly, creating practical challenges in correctly timing contrast administration with image acquisition. Contrast-enhanced 4D magnetic resonance imaging (4D-MRI)¹ offers a promising strategy for directly visualizing liver tumor motion. The superior soft tissue contrast of MRI and long usable duration of hepatobiliary MRI contrast allows the visualization of tumors throughout the respiratory cycle [4,5].

Prior studies have demonstrated 4D-MRI acquisition using multi-slice 2D or 3D sequences with Cartesian or non-Cartesian sampling trajectories [6–10]. Despite

increased interest, clinical implementation of 4D-MRI technology has been limited because it requires specialized acquisition protocols, reconstruction techniques, and hardware. In this study, we adopted a novel 4D-MRI technique¹ that performs continuous volumetric scanning with self-gating and retrospective respiratory binning that can capture irregular respiratory motion. We assessed the feasibility of using 4D-MRI in target volume generation for liver tumors and compared 4D-MRI with 4D-CT in terms of liver tumor clarity and the dosimetry of radiation treatment plans [11].

Materials and methods

Image acquisition and reconstruction

Twelve patients undergoing SBRT to the liver were prospectively recruited into this IRB-approved study. All patients received same-day 4D-CT and 4D-MRI simulation using identical positioning and immobilization. 4D-CT scans were acquired over a single respiratory cycle (120 kVp, 0.98 × 0.98 mm voxels, 3 mm slice thickness, scan time ~1 minute) and retrospectively binned using 8-phase reconstruction (SOMATOM Definition AS, Siemens Healthcare, Forchheim, Germany).

MRIs were acquired on a 3 Tesla MRI simulator (MAGNETOM Vida, Siemens Healthcare, Erlangen,

¹Work in progress. The application is currently under development and is not for sale in the U.S. and in other countries. Its future availability cannot be ensured.



Germany) using a large 18-channel UltraFlex coil suspended from a coil bridge and a 32-channel spine coil. 4D-MRIs were acquired after injection with hepatobiliary contrast (gadoxetic acid) [12] using a T1-weighted 3D fast gradient echo sequence acquired in the axial plane with a golden-angle stack-of-stars sampling trajectory (TE/TR = 1.4/2.8 ms, 1.3×1.3 mm voxels, 3 mm slice thickness, FOV = 380×380 mm², 64–72 slices) [13]. 4D-MRI *k*-space was filled continuously over multiple respiratory cycles (scan time ~8–10 minutes). A self-gating signal (SGS) was extracted from the *k*-space center and used as a respiratory motion surrogate. The Advanced 4D MRI¹ research sequence was used to provide a binning option that separates inhalation and exhalation in the SGS-based motion trace. For consistency with CT, the total number of respiratory bins was chosen as 8. The SGS waveform was first segmented into 4 amplitude bins, and then data in the same bin were separated into inspiration and expiration groups according to the direction of the motion. After respiratory binning, images were reconstructed using a standard radial re-gridding algorithm.

To identify regular and irregular breathers, breathing regularity was quantified using the SGS waveform. The peak-to-trough range and mid-level amplitude (i.e. (peak-amplitude + trough-amplitude) / 2) were calculated for each respiratory cycle. The average mid-level amplitude across all cycles normalized by the average peak-to-trough range was used as the regularity score. Subjects with the score greater than 20% were defined as irregular breathers.

Image analysis

Image quality was assessed using a 4-point Likert scale ('clarity score'). Images were scored as follows:

- 1 diagnostic quality,
- 2 non-diagnostic, but clearly demarcated lesion,
- 3 less clear borders but definable for treatment planning, and
- 4 lesion undefinable for treatment planning.

Images for each patient were reviewed concurrently by two radiation oncologists and a consensus score was assigned for the end-inspiration and end-expiration phase of each binning technique. Paired *t*-tests were used to compare images and differences were considered statistically significant if *p*-value < 0.05.

Radiotherapy target delineation and treatment planning

Targets were independently contoured on the 4D-CT and 4D-MRI scans by two radiation oncologists. Gross target

volumes (GTV) were contoured on each image phase and internal target volumes (ITV) were generated by summing the GTVs. Planning target volumes (PTVs) were generated by expanding ITVs 8 mm vertically and 5 mm in all other directions. Volumetric information for MR- and CT-derived PTVs were extracted and compared using paired *t*-tests.

4D-CT and 4D-MRI datasets were co-registered by fusing ITVs in the corresponding end-expiration phases. For patients with multiple lesions, separate registrations were performed for each target to account for liver compressibility and rotation. For each patient, a planning CT was generated from the mean intensity projection of the 4D-CT images. All PTVs were transferred to, and OARs were contoured on, this average 4D-CT dataset. To assess dosimetric impacts of MR-derived (PTV_{MRI}) and CT-derived (PTV_{CT}) targets, radiation plans were optimized separately on each dataset according to the target prescription and OAR objectives used clinically for each patient.

Treatment planning was performed in RayStation (v.7.0 RayStation Laboratories, Stockholm, Sweden) using 10 MV or 10 FFF photon coplanar volumetric modulated arc therapy. Targets were treated to a median dose of 50 Gy in 5 fractions. To maintain consistency and ensure plan quality, all plans were created by a single planner who followed the same workflow that is implemented for clinical patients. To minimize the introduction of biases towards MR- versus CT-optimized plans, each patient's plan was initialized using the same beam orientation and optimization objectives. Thereafter, objectives were adjusted independently during plan optimizations to produce clinically acceptable plans. The proportion of the PTVs receiving 90% of the prescription dose for MR- and CT-derived targets was extracted from the plans optimized for the respective targets. To assess the MR target coverage using CT-optimized plans used in current practice, the PTV coverage for the MR-derived targets was also extracted from the CT-optimized plan. The PTV coverage for MR-derived targets on the MR- and CT-optimized plans were compared to the coverage of CT-derived targets using paired *t*-tests.

Results

Image acquisition

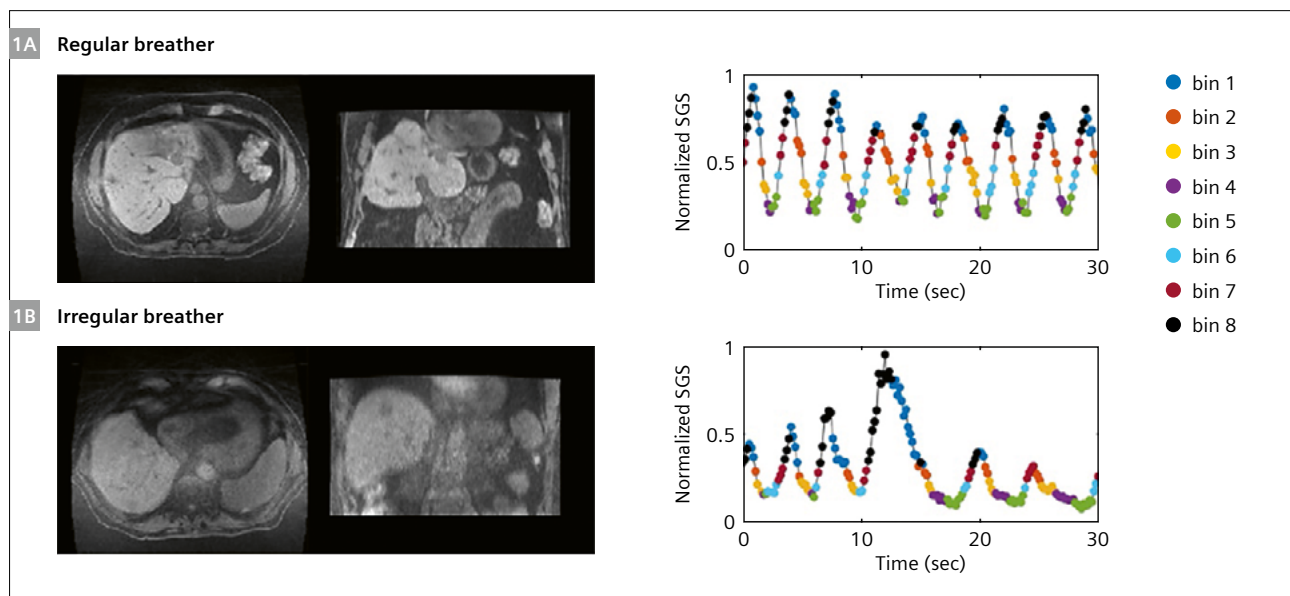
4D-MRIs were obtained for twelve patients with a total of 17 liver tumors. Of the twelve patients, six were classified as regular breathers and six as irregular breathers. Example axial and coronal views of regular and irregular breathers is shown in Figure 1, along with their corresponding respiratory traces and binning results. The binning algorithm was

found to be robust to both regular (Fig. 1A) and irregular (Fig. 1B) breathing patterns.

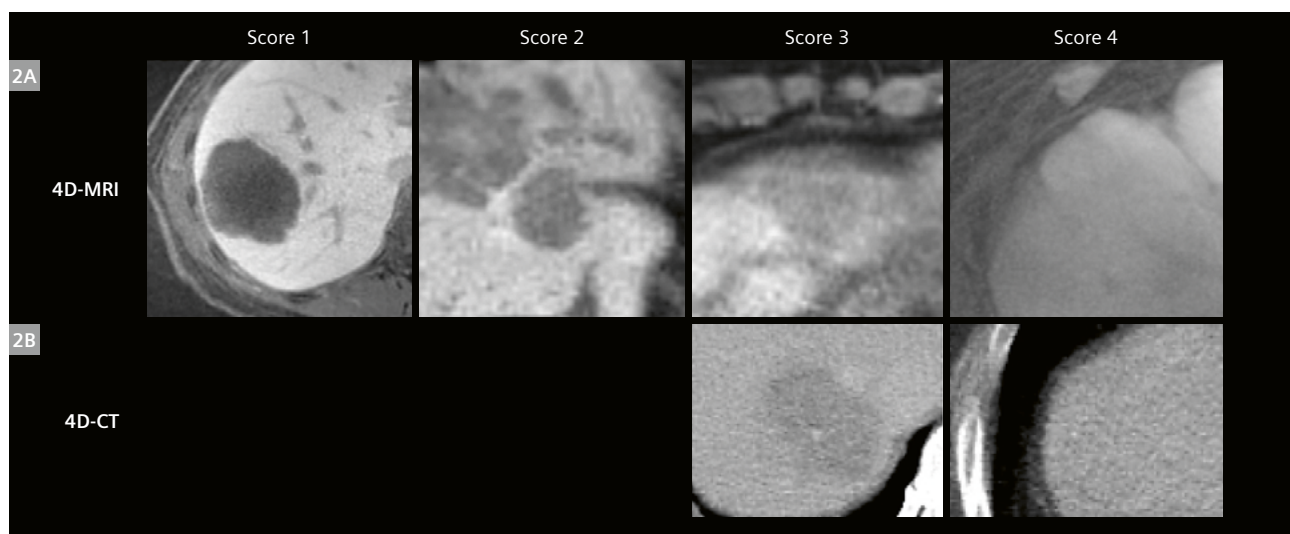
Image quality was assessed using a 4-point clarity score, with lower clarity scores corresponding to superior image quality, as shown in Figure 2. Clarity scores were significantly better for 4D-MRI versus 4D-CT (1.2 ± 0.4 and 3.5 ± 0.7 , respectively, $p < 10^{-9}$). No liver tumors were rated 4 on any 4D-MRI because all lesions were definable on all phases regardless of the binning algorithm. No liver tumors were rated 1 or 2 on any 4D-CT.

Radiotherapy target delineation and treatment planning

On average, there was no significant difference between volumes of MRI-derived and CT-derived targets (39 cc vs. 44 cc, respectively, $p = 0.44$). Analysis of the radiation plans revealed no significant difference between the dosimetric coverage of 17 CT-derived and MR-derived PTVs on the plans optimized for their respective volumes (PTV receiving 90% of prescription: 89.38% vs. 90.61%, respec-



1 Comparison of images and respiratory binning for patients who breathed **(1A)** regularly and **(1B)** irregularly. A 30-second segment of the respiratory self-gating signal (SGS) is also displayed for each binning option. Each point in the waveform has a timing correspondence to a segment of k -space data acquisition, and the color represents the bin index assigned to the data.



2 Atlas depicting the Likert-4 scale qualitative assessment of image quality of tumors on 4D-MRI **(2A)** and 4D-CT **(2B)** reconstructions. Score legend: (1) diagnostic quality, (2) non-diagnostic, but clearly demarcated lesion, (3) less clear borders but definable for treatment planning, and (4) lesion undefinable for treatment planning. There were no 4D-CT images scored at values of 1 or 2.



tively, $p = 0.68$) demonstrating similar plan quality for the targets. However, a comparison of the PTV coverage on the CT-optimized plan revealed significantly lower coverage of MR-derived compared to CT-derived targets (PTV receiving 90% of prescription: 75.56% vs. 89.38%, $p = 0.002$), indicating that planning to the 4D-CT-derived target would result in underdosing of the tumor (Fig. 3). There was no significant difference in the mean liver dose including the PTVs (16.34 Gy vs. 15.2 Gy, respectively, $p = 0.29$) or the doses to additional organs at risk for CT- and MR-optimized plans ($p > 0.05$), as OAR sparing had priority over target coverage.

Discussion

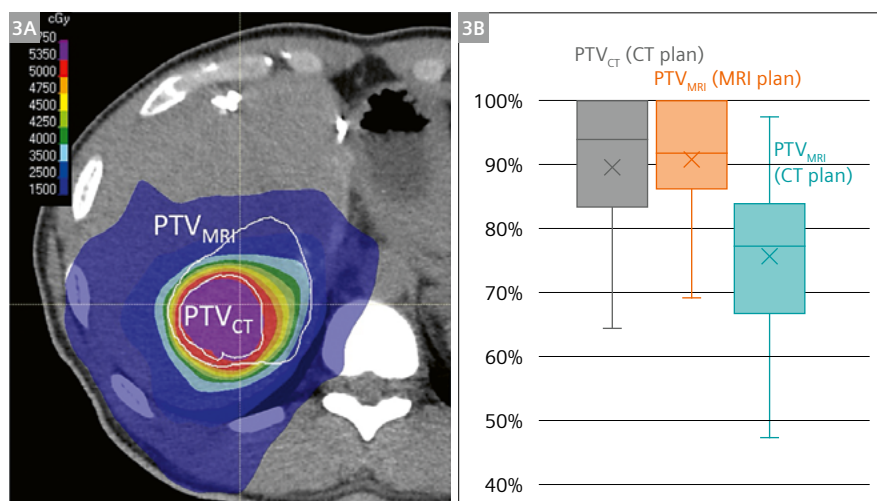
Accurately delineating liver tumors is essential for delivering radiation dose to the desired targets while minimizing radiation to normal tissues. In this study, we demonstrate the feasibility of using contrast-enhanced 4D-MRI for the direct visualization of liver tumors throughout the respiratory cycle for ITV generation. Estimating the motion of liver tumors on 4D-CT is fraught with uncertainty because detailed internal anatomy cannot be seen. In contrast, the reliable direct visualization of liver tumors during the respiratory cycle using 4D-MRI facilitates the production of ITVs that accounts for respiratory hysteresis and tissue compressibility.

We adopted a 4D-MRI technique that performs continuous volumetric scanning with self-gating and respiratory binning using a 3D T1-weighted fast gradient echo sequence and a golden-angle radial acquisition scheme. This acquisition scheme is inherently more robust to motion artifacts compared to Cartesian acquisition and allows high-frequency sampling of the center of k -space, from which a respiratory motion trace can be derived. As the motion trace is extracted from the acquired data itself, there is no need for external respiratory devices or

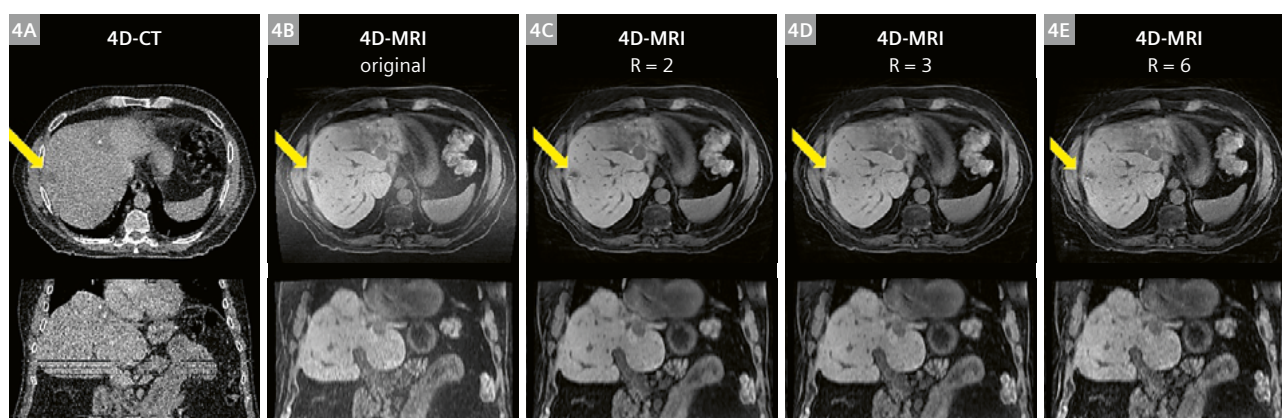
surrogates. In contrast to 4D-CT acquisition, which acquires data through a single respiratory cycle, this 4D-MRI approach continuously samples breathing over several minutes, with the final average over multiple respiratory cycles potentially being more representative of patients' normal breathing versus helical 4D-CT.

The dosimetric data demonstrated that the use of 4D-MRI may improve radiation targeting of liver tumors. In our study, MRI-generated ITVs tended to be smaller than CT-derived ITVs, although the difference was not statistically significant. Dosimetric data for radiation plans showed similar coverage when optimized for CT-derived and MR-derived targets and dose to adjacent organs at risk, though the significantly lower MR-derived target coverage on CT-optimized plans suggests that the current methods of treatment planning may lead to tumor underdosing and increase the risk of marginal misses. It is unclear how much the difference in ITV generation contributes to the local recurrence of tumors after SBRT, as tumor control is generally high ($> 90\%$) but recurrences could be due to marginal misses resulting from the under-contouring of tumor positions during respiration. Additional research is needed on the clinical impact using MR-based targets on tumor control and tissue toxicity.

Reducing MRI acquisition time is advantageous for many reasons including increased patient comfort and hospital throughput. One method for MRI acceleration is through compressed sensing (CS), however, the effects of CS acceleration on 4D-MRI in the context of radiotherapy treatment planning has not yet been investigated. Our group is investigating the compressed sensing capabilities currently available in the Advanced 4D MRI research sequence. Figure 4 shows example axial and coronal views of a (4A) 4D-CT, (4B) original 4D-MRI (~10-minute acquisition), and simulated 4D-MRI acceleration rate (R) of (4C) $R = 2$ (~5-minute acquisition), (4D) $R = 3$ (~3.3-minute acquisition), and (4E) $R = 6$ (~1.7-minute acquisition).



3 (3A) Example axial slice of a radiation treatment plan optimized using CT-derived target volume ('CT plan'). The inner white line shows the CT-derived target (PTV_{CT}), the outer white line shows the MR-derived target (PTV_{MRI}), and the colored regions correspond to isodose lines. **(3B)** A boxplot distribution for all 17 PTVs covered by 90% of the prescription dose shows a similar distribution of PTV coverage between CT-derived (gray) and MR-derived (orange) targets on plans optimized for their respective volumes and lower coverage of MRI-derived (petrol) targets for CT-optimized plans.



4 Example axial and coronal slices of exhale phase **(4A)** 4D-CT and 4D-MRIs reconstructed using **(4B)** original 3000 spoke sampling and acceleration factors (R) **(4C)** R = 2, **(4D)** R = 3, and **(4E)** R = 6. The liver tumor is annotated using the yellow arrow in all axial planes. Note that the 4D-MRI improves tumor contrast and resolves respiratory-induced motion artifacts relative to the 4D-CT.

Overall, there are many factors that can impact 4D-MRI image quality, including the breathing pattern of the subject, choices of sparsity constraints and regularization weighting in the CS algorithm, and SGS signal processing. The impacts of these factors are currently being investigated using a 4D MRI motion phantom.

Conclusion

This study demonstrates the feasibility of using hepatobiliary contrast-enhanced 4D-MRI to delineate gross liver tumors directly throughout the respiratory cycle. The lower coverage of directly visualized MRI targets in plans generated using standard of care 4D-CT-derived targets suggests that the adoption of 4D-MRI for motion management may improve radiation treatment of liver lesions and reduce the risk of marginal misses. Future investigations will focus on impacts of compressed sensing acceleration and ground-truth measurements in a 4D-MRI phantom.

References

- 1 Mahadevan A, Blanck O, Lanciano R, et al. Stereotactic Body Radiotherapy (SBRT) for liver metastasis – clinical outcomes from the international multi-institutional RSSearch® Patient Registry. *Radiation Oncology*. 2018;13(1):1-11.
- 2 Ohri N, Tomé WA, Romero AM, et al. Local control after stereotactic body radiation therapy for liver tumors. *International Journal of Radiation Oncology* Biology* Physics*. 2021;110(1):188-195.
- 3 Doi H, Beppu N, Kitajima K, Kuribayashi K. Stereotactic body radiation therapy for liver tumors: current status and perspectives. *Anticancer Research*. 2018;38(2):591-599.
- 4 Wojcieszynski AP, Rosenberg SA, Brower JV, et al. Gadoxetate for direct tumor therapy and tracking with real-time MRI-guided stereotactic body radiation therapy of the liver. *Radiother Oncol*. Feb 2016;118(2):416-8. doi:10.1016/j.radonc.2015.10.024
- 5 Leyendecker JR. Gadoxetate disodium for contrast magnetic resonance imaging of the liver. *Gastroenterology & Hepatology*. 2009;5(10):698.
- 6 von Siebenthal M, Szekely G, Gamper U, Boesiger P, Lomax A, Cattin P. 4D MR imaging of respiratory organ motion and its variability. *Physics in Medicine & Biology*. 2007;52(6):1547.
- 7 Hu Y, Caruthers SD, Low DA, Parikh PJ, Mutic S. Respiratory amplitude guided 4-dimensional magnetic resonance imaging. *International Journal of Radiation Oncology* Biology* Physics*. 2013;86(1):198-204.
- 8 Tryggstad E, Flammang A, Han-Oh S, et al. Respiration-based sorting of dynamic MRI to derive representative 4D-MRI for radiotherapy planning. *Medical physics*. 2013;40(5):051909.
- 9 Deng Z, Pang J, Yang W, et al. Four-dimensional MRI using three-dimensional radial sampling with respiratory self-gating to characterize temporal phase-resolved respiratory motion in the abdomen. *Magnetic resonance in medicine*. 2016;75(4):1574-1585.
- 10 Van de Lindt TN, Fast MF, van der Heide UA, Sonke J-J. Retrospective self-sorted 4D-MRI for the liver. *Radiotherapy and Oncology*. 2018;127(3):474-480.
- 11 Thomas HR, Miao X, Ferguson D, et al. Contrast-enhanced 4D-MRI for internal target volume generation in treatment planning for liver tumors. *Radiotherapy and Oncology*. 2022;
- 12 Van Beers BE, Pastor CM, Hussain HK. Primovist, Eovist: what to expect? *Journal of hepatology*. 2012;57(2):421-429.
- 13 Grimm R, Block K, Hutter J, et al. Self-gating reconstructions of motion and perfusion for free-breathing T1-weighted DCEMRI of the thorax using 3D stack-of-stars GRE imaging. 2012:3814.

Contact

Jessica Scholey, Ph.D., DABR
Assistant Professor
Director of MRI Simulation
Department of Radiation Oncology
University of California San Francisco
505 Parnassus Ave., Room L-75
San Francisco, CA 94143-0226
USA
Tel.: +1 (415) 353-7191
jessica.scholey@ucsf.edu



The entire editorial staff at Siemens Healthineers extends their appreciation to all the radiation oncologists, radiologists, technologists, physicists, experts, and scholars who donate their time and energy – without payment – in order to share their expertise with the readers of MAGNETOM Flash and the MReadings.

MAGNETOM Flash – Imprint

© 2023 by Siemens Healthcare GmbH,
All Rights Reserved

Publisher:

Siemens Healthcare GmbH
Magnetic Resonance,
Karl-Schall-Str. 6, D-91052 Erlangen, Germany

Editor-in-chief:

Antje Hellwich
(antje.hellwich@siemens-healthineers.com)

Copy Editing:

Sheila Regan, Jen Metcalf, UNIWORKS,
www.uni-works.org
(with special thanks to Kylie Martin)

Layout:

Agentur Baumgärtner,
Friedrichstr. 4, D-90762 Fürth, Germany

PrePress and Image Editing, Production:

Clemens Ulrich, Paul Linssen,
Siemens Healthcare GmbH

Printer:

Schmidl & Rotaplan Druck GmbH,
Hofer Str. 1, D-93057 Regensburg, Germany

Note in accordance with § 33 Para.1 of the German Federal Data Protection Law: Despatch is made using an address file which is maintained with the aid of an automated data processing system.

MAGNETOM Flash is sent free of charge to Siemens Healthineers MR customers, qualified physicians, technologists, physicists and radiology departments throughout the world. It includes reports in the English language on magnetic resonance: diagnostic and therapeutic methods and their application as well as results and experience gained with corresponding systems and solutions. It introduces from case to case new principles and procedures and discusses their clinical potential. The statements and views of the authors in the individual contributions do not necessarily reflect the opinion of the publisher.

The information presented in these articles and case reports is for illustration only and is not intended to be relied upon by the reader for instruction as to the practice of medicine. Any health care practitioner reading this information is reminded that they must use their own learning, training and expertise in dealing with their individual patients. This material does not substitute for that duty and is not intended by Siemens Healthcare to be used for any purpose in that regard. The drugs and doses mentioned herein are consistent with the approval labeling for uses and/or indications of the drug. The treating physician bears the sole responsibility for the diagnosis and treatment of patients, including drugs and doses prescribed in connection with such use. The Operating Instructions must always be strictly followed when operating the MR system. The sources for the technical data are the corresponding data sheets. Results may vary.

Partial reproduction in printed form of individual contributions is permitted, provided the customary bibliographical data such as author's name and title of the contribution as well as year, issue number and pages of MAGNETOM Flash are named, but the editors request that two copies be sent to them. The written consent of the authors and publisher is required for the complete reprinting of an article.

We welcome your questions and comments about the editorial content of MAGNETOM Flash. Please contact us at
magnetomworld.team@siemens-healthineers.com

Manuscripts as well as suggestions, proposals and information are always welcome; they are carefully examined and submitted to the editorial board for attention. MAGNETOM Flash is not responsible for loss, damage, or any other injury to unsolicited manuscripts or other materials. We reserve the right to edit for clarity, accuracy, and space. Include your name, address, and phone number and send to the editors, address above.

MReadings: Liver MRI is also available online:

www.magnetomworld.siemens-healthineers.com/publications/mreadings

Not for distribution in the US

On account of certain regional limitations of sales rights and service availability, we cannot guarantee that all products included in this brochure are available through the Siemens sales organization worldwide. Availability and packaging may vary by country and is subject to change without prior notice. Some/All of the features and products described herein may not be available in the United States.

The information in this document contains general technical descriptions of specifications and options as well as standard and optional features which do not always have to be present in individual cases, and which may not be commercially available in all countries.

Due to regulatory reasons their future availability cannot be guaranteed. Please contact your local Siemens organization for further details.

Siemens reserves the right to modify the design, packaging, specifications, and options described herein without prior notice. Please contact your local Siemens sales representative for the most current information.

Note: Any technical data contained in this document may vary within defined tolerances. Original images always lose a certain amount of detail when reproduced.

Siemens Healthineers Headquarters

Siemens Healthcare GmbH
Henkestr. 127
91052 Erlangen, Germany
Phone: +49 9131 84-0
siemens-healthineers.com